Forschungszentrum Karlsruhe

Technik und Umwelt

Wissenschaftliche Berichte

FZKA-6380

PREMIX Experiments PM12-PM18 to Investigate the Mixing of a Hot Melt with Water

A. Kaiser, W. Schütz, H. Will

Institut für Reaktorsicherheit

Programm Nukleare Sicherheitsforschung

Forschungszentrum Karlsruhe GmbH, Karlsruhe
2001

This document has been prepared
in the frame of the
4th EU Framework Programme
on Fission Reactor Safety 1996-99,

MFCI-Project
Contract FI4S-CT96-0037
Activity 2.1, PREMIX tests P2

EU number of present document:
INV-MFCI(00)-D091

Abstract

In the case of a hypothetical core melt-down accident in a pressurised light water reactor, hot melt may be relocated and mixed with water present in the lower coolant plenum. The amount of masses involved in the mixing process and the intensity of thermal interaction determine the extent of a possible steam explosion.

Such processes have been investigated, on a technical scale, at the Forschungszentrum Karlsruhe in so-called PREMIX experiments. Melt was released from above into a water pool using alumina instead of corium. Eighteen tests, PM01 to PM18, have been performed from 1994 to 1999. PM12 to PM18 were a task of the EU-MFCI-project within the Fourth Framework Programme. For that purpose, geometrical key data of the experimental facility as well as starting conditions of some of these tests were chosen to meet as close as possible those of the FARO/FAT tests performed at JRC Ispra with molten corium and water. This was in order to facilitate comparison of results.

Three tests (PM12, 13, 14) were started with almost identical parameters. The general course of events turned out to be very similar. Deviations nonetheless found in the results can generally be attributed to uncertainties in the procedure of preparing and controlling the melt supply. By this, reproducibility of the PREMIX experiments has been proven.

The conditions of two other tests (PM16, 17) were set to meet those of two FARO tests, L-28 and L-31. These were the melt mass, water temperature and depth, system pressure, nozzle diameter, and duration of melt release.

In most cases, under saturated water conditions, melt penetration, premixing, and steam production occurred in such a way that the bulk of water was prevented from close contact with the melt. Steam and water were in equal shares, around 50%, in the interaction zone. In case of large initial subcooling of the water, the share of the steam and, with it, the average distance between melt and water in the interaction zone were much smaller. Nonetheless, a steam explosion did not occur.

The influence of the various parameters on the results is discussed. Special interest is devoted to the evaluation of the jet break-up length. The report gives a documentation of all relevant data. The data should be used for the validation of multiphase computer programmes which are presently developed in reactor safety research.

Zusammenfassung

PREMIX, Abschlußbericht der zweiten Testserie (PM12 - PM18)

Beim Niederschmelzen des Reaktorkerns, denkbar als Folge eines hypothetischen Störfalls in einem Druckwasserreaktor, kann heiße Schmelze in das untere Kühlmittelplenum gelangen und sich mit dort vorhandenem Wasser mischen. Die Menge der an der Vermischung beteiligten Massen und die Intensität der thermischen Wechselwirkung bestimmen das Ausmaß einer eventuell auftretenden Dampfexplosion.

Derartige Vorgänge wurden im Forschungszentrum Karlsruhe in den sogenannten PREMIX Experimenten in technischem Maßstab untersucht. Die heiße Schmelze floss von oben in ein Wasserbad. Anstelle von Corium wurde Aluminiumoxid-Schmelze verwendet. Von 1994 bis 1999 wurden insgesamt 18 PREMIX-

Experimente (PM01 – PM18) durchgeführt. PM12 bis PM18 waren Teil eines Arbeitspakets des EU-MFCI-Projektes innerhalb des Vierten Rahmenprogramms. In diesem Zusammenhang wurden geometrische Eckdaten der Teststrecke wie auch Startbedingungen bei einigen dieser Versuche so gewählt, dass sie möglichst gut mit denen der FARO/FAT Versuche übereinstimmten, die im Forschungszentrum JRC in Ispra mit geschmolzenem Corium und Wasser durchgeführt wurden. Zweck war eine Erleichterung beim Vergleich der Ergebnisse.

Drei Experimente (PM12, 13, 14) wurden unter fast gleichen anfänglichen Bedingungen durchgeführt. Der generelle Ablauf der drei Versuche war sehr ähnlich. Dennoch festgestellte Unterschiede können Unsicherheiten im zeitlichen Ablauf der Schmelzeerzeugung zugewiesen werden. Das Ergebnis zeigt, dass die PREMIX-Experimente reproduzierbar sind

Die Bedingungen zweier weiterer Versuche (PM16, 17) wurden denen zweier FARO Tests, L-28 and L-31, angepasst. Es waren die Parameter Schmelzemasse, Wassertemperatur und -tiefe, Systemdruck, Durchmesser der Schmelzedüse und Dauer des Schmelzeausflusses.

Die Mehrzahl der Versuche wurde unter der Bedingung gesättigten Wassers durchgeführt. Hier verliefen das Eindringen der Schmelze in das Wasser, die Vorvermischung und die Dampfbildung in einer Weise, dass die Hauptmasse des Wassers von einem engen Kontakt mit der Schmelze abgehalten wurde. Dampf und Wasser waren in etwa gleichen mittleren Volumenanteilen in der Interaktionszone vorhanden. Im Falle starker anfänglicher Unterkühlung des Wassers waren der Anteil des Dampfes und mit ihm die mittlere Distanz zwischen Schmelze und Wasser in der Interaktionszone viel kleiner. In keinem Falle trat eine Dampfexplosion auf.

Der Einfluss der unterschiedlichen Parameter auf die Versuchsergebnisse wird diskutiert. Besonderes Interesse wird der Bestimmung der sog. Aufbrechlänge des Schmelzestrahls gewidmet. Die gleichfalls dokumentierten Messergebnisse bilden eine Datenbasis für die Validierung von Mehrphasen-Computerprogrammen, die gegenwärtig im Rahmen der Reaktor-Sicherheitsforschung entwickelt werden.

CONTENTS

APPENDICES

Detailed results of the PM15 to PM18 experiments are compiled in Appendices A to D, respectively. Performance and numerical simulation of the melt release are given in Appendix E. Estimation of the shares of the components in the interaction zone is given in Appendix F.

List of Figures

List of Tables

1. INTRODUCTION

Release of a hot melt into water may occur during a severe core-melt accident in a nuclear light-water reactor. In the course of the accident, the melt may drain down into the lower head of the reactor vessel which is filled with water. Quenching of the melt implies the possibility of a steam explosion which develops in several stages: premixing, triggering, propagation and expansion /1/. The energetics of the last stage depends on the extent and characteristics of mixing.

At Forschungszentrum Karlsruhe, from 1994 to 1999, an experimental programme called PREMIX has been performed in which the first stage, i.e. coarse mixing of a hot melt in water, was investigated on a small to medium scale (up to 60 kg of melt). Safety directions as well as similarity considerations led us to choose alumina as a simulating material instead of corium.

The use of a non-toxic and non-radioactive simulant material under realistic temperatures (and, thus, almost realistic heat transfer) had the big advantage that a large variety of instrumentation including video and high-speed photography could be applied. No elaborate protection was needed in measuring the escaping steam flow nor in post-test debris examination. This is reflected in a higher frequency of tests.

The PREMIX experiments aimed at identifying the phenomena that dominantly control the premixing as well as studying scaling effects. During the full R+D programme, a number of eighteen tests, PM01 to PM18, has been conducted under various starting conditions /2-8/. In the tests, we did not intentionally trigger for a steam explosion. However, the possibility of a spontaneous explosion could not be excluded. Only once, a steam explosion occurred which destroyed the test facility. This was in PM11 /4, 5/, the only test in which three parallel melt jets were simultaneous released into comparatively shallow water (0.5 m depth).

The information gained helps in validating multi-phase computer codes presently under development, i.e. MC3D at CEA Grenoble and at FZK, MATTINA at FZK, IVA5 at SIEMENS, IKEJET at IKE, Stuttgart, and COMETA at JRC /9, 10/. Codes are needed to compare the influence of different melt materials and to extrapolate results to reactor conditions.

The information can be used as well for comparison with experiments carried out with a prototypical corium melt on a similar scale. This comparison is important since the more pronounced tendency of alumina towards steam explosion compared to corium is still an open question. Experiments with prototypical materials have been performed at JRC Ispra, using the FARO and KROTOS facilities /11-14/. The KROTOS facility has also been used for tests with alumina on a 2 kg scale. These experiments may be also considered in scaling studies.

During the European Commission’s Fourth Framework Programme on Nuclear Fission Safety from 1996 to 1999 (cf. the final report, ref. 15), PREMIX was a task of a shared-cost project on molten fuel-coolant interactions (MFCI) entitled ‘Characterisation of processes which govern quenching of molten corium in water, including steam explosions’. It was intended to carry out, at JRC Ispra (FARO/FAT) and FZK (PREMIX), at least two experiments each with different melt materials. By setting, as much as possible, all other test conditions in accordance with FARO, it was hoped to attribute differences in the results directly to the different melt properties.

Differences in the properties of the melts are in the composition, in the densities, in the absolute temperatures, and in the temperature span above solidus. On the other hand, good agreement is given in the total enthalpies. The agreement is not so good in the excess enthalpy which influences, among other properties, premixing during the initial period of interaction. In Table I, physical properties and conditions are compared of a melt typical of PREMIX with those of corium melt /16/ estimated for a light water reactor (LWR). Note that the composition of the melt used in FARO is similar to that given here for an LWR. The melt release temperature in the L-28 and L-31 FARO tests was 3000 – 3050 K. In any case, the use of computer codes is essential to properly find the influence on the results of the different test conditions.

Table I: Actual properties of the melt in PREMIX compared with properties estimated for corium melt (cf. ref. 16).

	PREMIX	LWR
Composition of melt, wt%	>90% oxides (Al_2O_3 with very small portions of other oxides); <10% iron	UO_2 + 22.2%ZrO_2
Average melt density, kg/ m^3	2800	7350
Melt release temperature, K	2600	3300
Temperature at solidus, K	≈2313	2815
Total enthalpy, MJ/m^3	$11.9 \cdot 10^3$	$12.3 \cdot 10^3$
Excess enthalpy above solidus, MJ/m^3	$\approx 1.45 \cdot 10^3$	$\approx 5 \cdot 10^3$

Table II gives essential conditions of PM12 to PM18 and the corresponding numbers settled in the above EU-MFCI project, where PM12 to PM14 are regarded as reference tests. For details see Chapter 3.

By extending the vessel height by one meter during reconstruction of the PREMIX test facility after PM11, the potential was increased for larger water depths together with larger melt masses scheduled for the following tests. Note that the large falling height in FARO, around 0.9 m, could not be realized in PREMIX. To adjust the speed of melt penetration into the water in PREMIX to those verified in FARO, a small overpressure in the crucible was applied.

A few differences being less important remained: the conditions of steam release, the expansion volume and the freeboard volume. The latter is defined as the volume between initial water surface and nozzle. For details see Chapter 6.

Table II: Nominal PREMIX test conditions, EU-MFCI numbering, and correspondent JRC FARO tests.

		Nominal conditions						
FZK number	Date	Melt mass [kg]	Water	System pressure [MPa]	Duration of melt release [s]	Steam venting pipes	EU-MFCI /	JRC numbers
PM12	06.06.97	20	sat	0.1	2	open	P2	
PM13	13.10.97	20	sat	0.1	2	open	P2	
PM14	10.03.98	20	sat	0.1	2	open	P2	
PM15	16.09.98	20	sat	0.5	2	open	P3	
PM16	03.02.99	50	sat	0.5	6	open	P1	FARO L-28
PM17	20.04.99	15	sub, 104 K	0.2	2	closed	P4	FARO L-31
PM18	07.07.99	15	sub, 26 K	0.2	2	closed	P5	

The present report gives in its first part results of the PM12 to PM18 tests in a comprehensive form. Comparison with FARO results is given in Chapter 6. Detailed results of PM12 to PM14 have been reported earlier /8/, those of PM15 to PM18 are compiled in the Appendices.

2. EXPERIMENTAL FACILITY

The PREMIX test facility (Fig. 1) was housed in a 220 m^3 steel vessel which primarily served as a safety container. It could also be pressurised to allow experiments under elevated system pressures. The test rig consisted mainly of a vertical, largely cylindrical vessel, 4 m high and 0.7 m in diameter. The design pressure was 0.6 MPa. The bottom part of the vessel contained water, the melt source was installed in the upper part. The test vessel was closed except for the four venting pipes, equipped with water separators, through which the steam formed during quenching escaped. The steam venting lines were closed in PM17 and PM18.

The melt was provided by an exothermal thermite reaction of powdered aluminium and iron oxide densely filled into the crucible. The melt generator was designed to retain the liquid iron and to release mostly alumina into the water. The water level was adjusted to the desired pool depth.

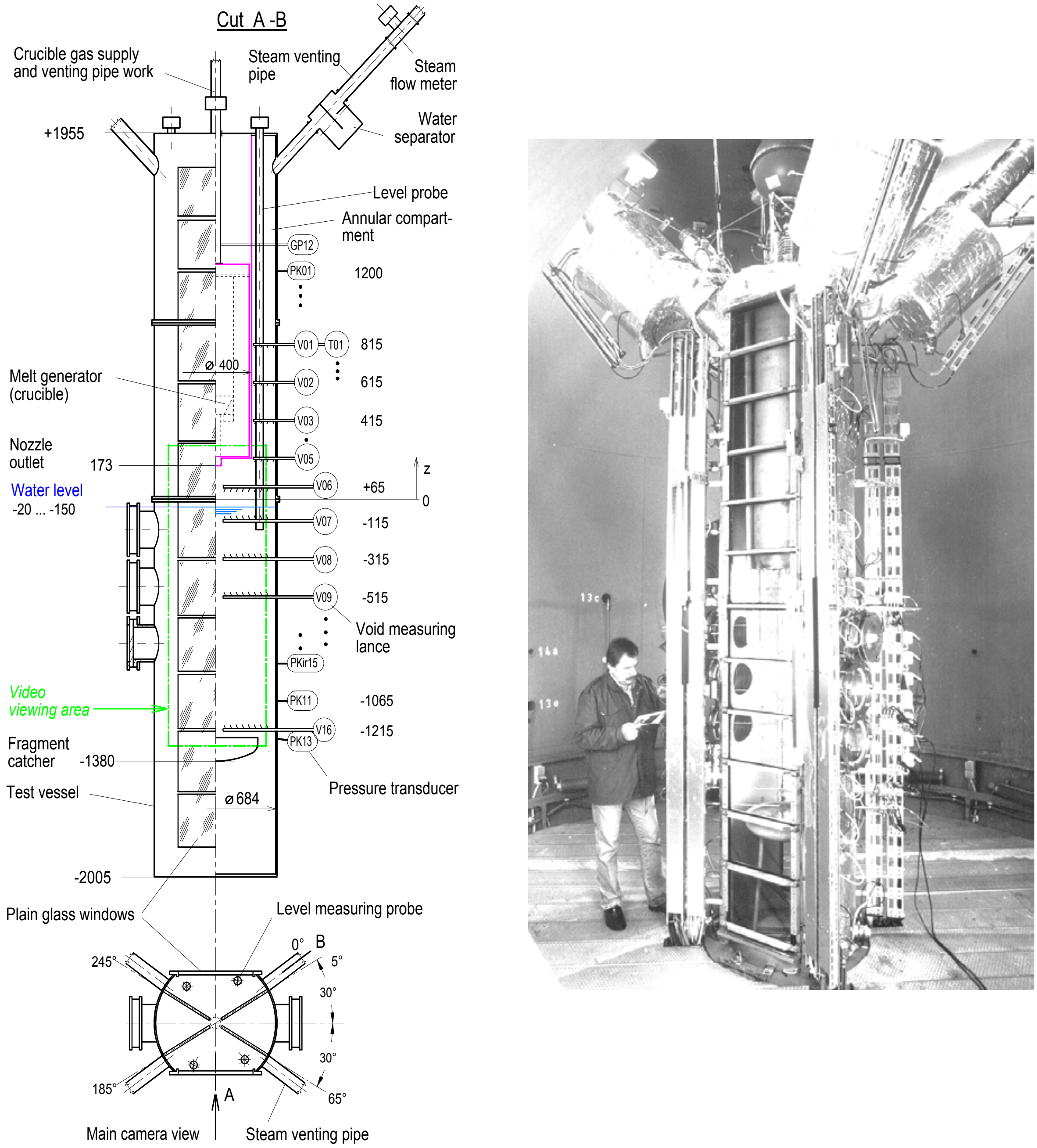

Fig. 1: Premix test facility, schematically. The photography shows the facility during preparation of a test. The video viewing area indicated in the sketch points to the section given in Fig. 2.

The facility was extensively instrumented with pressure transducers, level meters, thermocouples, and local void detectors. The instruments were distributed over the height as well as the azimuthal co-ordinate. Glass windows enabled video and high-speed filming which helped to identify characteristics of the mixing process.

Pressure transducers were mounted in the water, the freeboard volume, the venting tubes, and the melt generator. Mostly three types of pressure transducers were used: piezo-electric transducers, strain gauges, and piezo-resistive transducers.

Several *measuring lances*, equipped with eight (respectively three) *void sensors* and a thermocouple (abbrev. TC), were mounted at various axial levels and azimuthal positions in the water pool as well as in the freeboard volume. The sensors indicated whether or not there was water at their measuring tips. The *steam flow* was recorded by vortex flow meters mounted in the venting tubes.

The change of the *water level* was measured by use of four capacitive probes which were housed in steel tubes plunged into the water. The lower ends of the tubes were open, i.e. the water level within the tubes was measured. The probes were calibrated at room temperature a few hours prior to each test. The curves shown in the respective figures of this report have been shifted to account for the actual water level noted at the start of the test. The shift gives the effect of different temperature conditions (e.g. 373 K) at the start of the test. Very fast changes of the water level could not be reproduced by the system. It should also be noted that only the liquid water phase contributed to the signal voltage. Steam bubbles, that had been transported from the centre to the outer regions of the pool, i.e. where the level probes were situated, caused the actual water surface to be higher than the measured one. This condition was more pronounced at later times during the test.

Six evacuated *steel bottles* were used to take *gas samples* prior to and during the interaction. The bottles were connected to the freeboard volume via solenoid valves.

The output signals of the measuring instruments were recorded by data logger, transient recorders, and digital tapes. Most of the signals were picked up twice, with different registration speeds in order to get data even in the case of an unexpected steam explosion. Video and high speed filming (2000 f/s) helped in the interpretation of the test phenomena.

3. TEST PERFORMANCE AND TEST CONDITIONS

Providing the melt

The thermite powder was ignited at its top. During the reaction, the melt components, alumina and iron, separated due to their different densities. Gas and smoke escaped from the crucible (Fig. 1) from the very beginning through a venting line which was closed before the end of reaction. When the reaction front reached the bottom of the crucible, an annular compartment, integrated in the bottom, closed by a steel membrane and evacuated, was opened by melting the membrane. The heavier iron was collected in this compartment.

The reaction front proceeded through the bottom into the upper part of the nozzle tube. On its way down the tube, the melt front ruptured a second steel membrane (located 90 mm below the bottom) which initially separated the thermite filling from the free-board volume overlying the water pool. Immediately before the rupture, a sensor was contacted. This event triggered both the closure of the venting line and the activation of a gas pressure monitoring system (see Appendix E). The melt release started.

Since the melt release rate could not be measured, it was calculated on a simple numerical model, essentially consisting of a momentum equation that describes forced flow of melt in a pipe. Driving forces are gravity and the difference of pressure measured inside and outside of the melt generator (for more details see Appendix E).

Test conditions

The actual experimental conditions are given in Table III. The first three tests, PM12, PM13 and PM14, were performed under nominally identical starting conditions in order to prove reproducibility of the PREMIX tests. Of course, deviations in the results appeared which are due to (inevitable) variations in the starting conditions, e.g. in the melt mass or the driving pressure. The influence of a higher system pressure was investigated in PM15. PM16 was conducted with a larger melt mass than in previous PREMIX tests. High water subcooling (104 K) was applied in PM17.

Test PM18 aimed at further investigating the influence of water subcooling by applying moderate subcooling (about 30 K). The other test parameters agreed with those of PM17. The desired subcooling in PM18 was obtained by use of electrical heaters mounted at the bottom of the vessel. The heating produced a radial temperature gradient in the water (370 K in the centre and 362 K at the outside, see Table III).

The conditions of PM16 and PM17 were adjusted to those of L-28 and L-31, respectively, of FARO/FAT concerning the volumes of melt, nozzle diameter, duration of melt release, and speed of melt on contact with water. The latter required a small driving pressure to account for the larger falling height in the FARO tests. To compensate the pressure rise in the test vessel, an operational monitoring system, called control system in the following, maintained the pressure difference between crucible and interaction zone at a low level (0.005 – ≈0.015 MPa) by backfeeding gas to the crucible atmosphere from a reservoir. For more details see also Appendix E.

The melt released in the PREMIX tests in question (Table I) generally consisted of more than 90 % of oxides (alumina plus small fractions of iron oxide and other oxides). Less than 10 % consisted of iron and small fractions of impurities. The iron was due to incomplete separation during chemical reaction.

Table III: Actual conditions of the PM12 to PM18 PREMIX tests.

EXP.	MELT						WATER			SYSTEM
	Mass released [kg]	Nozzle diam. [mm]	Init. driv. press. [MPa]	Speed[1] [m/s]	Falling height [mm]	Release time [s]	Depth [mm]	Temp. [K]	ΔT_{sub} [K]	Press. p [MPa]
PM12	29.0	60	0.046	3.8 – 4.2	193	0.95	1360	372	1	0.1
PM13	23.8	60	0.052	4.0 – 4.2	213	1.05	1340	372	1	0.1
PM14	23.2	60	0.066	4.5 – 4.7	213	0.95	1340	372	0	0.1
PM15	23.1	60	0.03	3.2 – 3.3	323	1.25	1230	416	8	0.5
PM16	60.4	48	0.01[2]	1.9 – 2.5	223	5.0	1330	419	5	0.5
PM17	16.0	48	0.01[2]	1.7 – 2.6	223	1.70	1330	292	104	0.22
PM18	14.6	48	0.015[2]	1.9 – 2.9	223	1.50	1330	370-362[3]	26-34	0.22

1) on first melt/water contact – maximum; both values are calculated;

2) average value; pressure was controlled during melt release;

3) the scatter was due to internal convection prior to the start of melt release.

4. GENERAL COURSE OF A TEST AND EVALUATION OF DATA

General course of events

The information given in this section is mainly based on the evaluation of video and high-speed movies. Figure 2 gives, taking PM13 for example, a sequence of video frames.

Typically, the melt release started as single droplets which quickly increased in number. A few tenths of a second later, the droplet shower was followed by a stream of melt whose contour was cylindrical.

By the penetration of the melt into the water, an interaction zone was formed composed of melt, steam, and water. The formation of steam went along with a pressure rise. Water was displaced which led to an increase in the water level. The boundaries of the interaction zone expanded in axial and radial directions. The steam that escaped from the interaction zone flowed through the annular compartment between melt generator and vessel and through the venting lines (if open) into the container vessel.

The steam moved upward in highly turbulent flow, counter-current with the melt, carrying water drops and fine melt particles. The view to the melt stream soon became opaque, an identification of the melt release mode was no more possible. Water separators mounted in each tube separated water droplets and fine melt particles carried with the outgoing steam. At a later stage of the interaction, water drops became larger in size and even water slugs were carried up by the steam through the annulus. These temporarily blocked the entrances to the steam venting pipes. Part of the water carried with the steam was not retained in the separators and expelled into the container vessel.

When the leading edge of the melt reached a certain penetration distance, typically half a metre, the advance of fragmentation was such that the interaction became more violent. Subsequently, the steam generation was enhanced, the pressure as well as the water level increased at a larger rate than before. The melt penetrated further down and reached the fragment catcher. The more material gathered there, the more violent became the boiling in the lower part of the pool.

The melt stream, on its way down, fragmented due to hydrodynamic interaction with the water and the steam. Due to the long travel distance, the melt particles solidified or got at least a solid crust before they settled at the fragment catcher. In some cases, a portion of the melt formed a cake at the fragment catcher.

A substantial mass of melt reached the fragment catcher after typically 1.2 to 1.7 s. Melt release was finished at 1.2 to 1.4 s (in PM16 after about 5 s). The dimension of the cake was small in most cases. Possibly, part of the solid fragments became integrated in the cake, the majority of the fragments were found on top of it. Settling of the smaller fragments supposedly took a rather long time.

Evaluation of data

This section is to explain how the data were evaluated and to help in judging the results presented below. Note that the time when a substantial melt mass first contacted the water surface is defined as the origin of the time axis (t = 0) in all tests.

Melt flow rate Since the actual melt flow rate could not be measured, it was calculated on a small computer programme. The numerical model is based on a momentum equation that describes the flow of melt in a pipe. Simplifications are made,

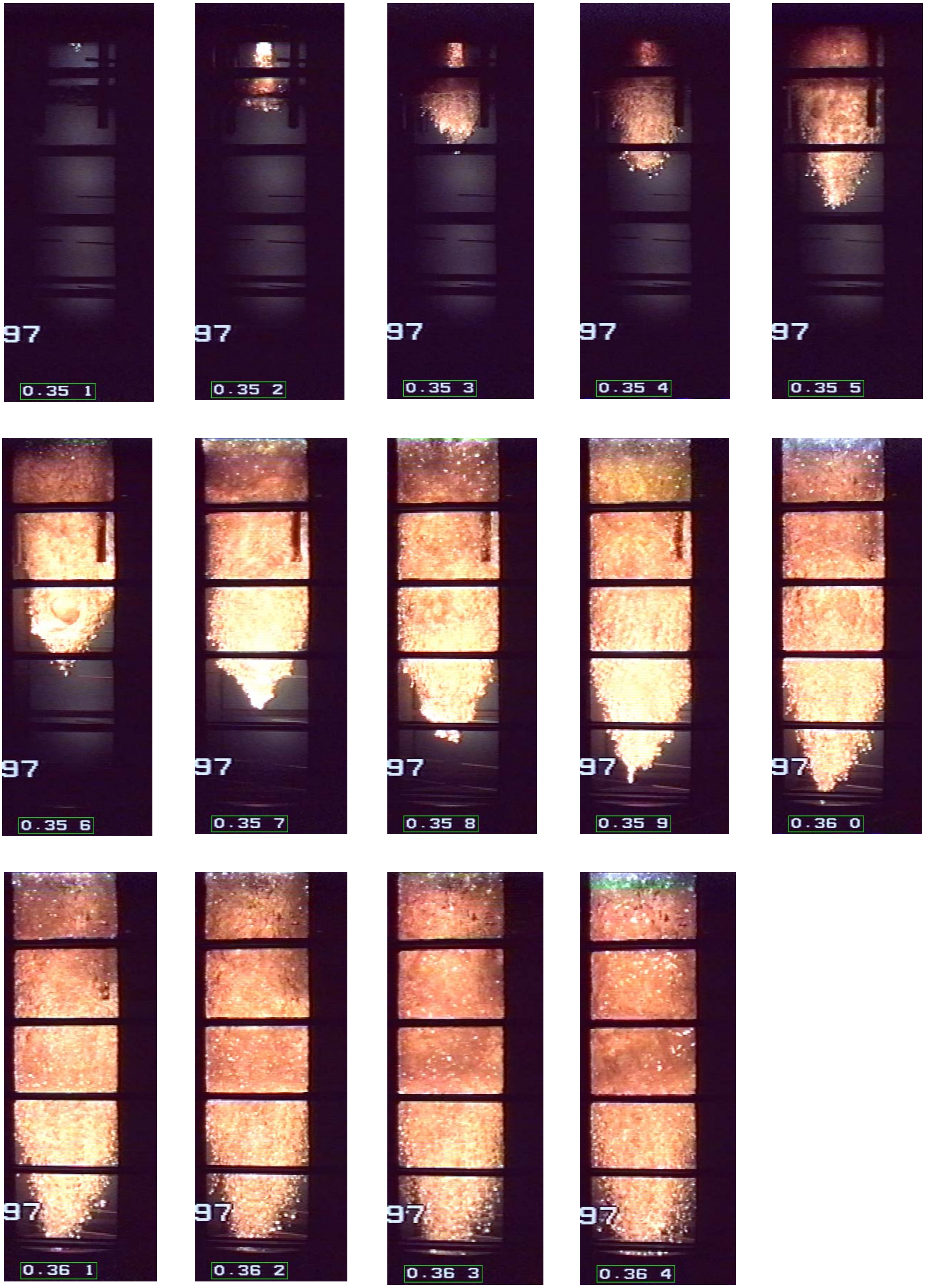

Fig. 2: Selected frames of the video film taken during test PM13. The time difference between two frames is 0.100 s, where the second frame corresponds to time about zero.

such as constant flow cross section and loss coefficients, respectively. Input are the impressed pressure difference and the melt mass. For more details see Appendix E.

Development of the interaction zone The progression of the interaction zone in the axial and radial directions were evaluated on basis of film pictures as well as of void data (first signal change from water to steam). The lines drawn in the r-z diagrams given in this report (e.g. Fig. 9) represent the outmost boundary of steam towards the bulk of water. Axial symmetry was assumed in the evaluation.

Size and composition of the interaction zone The evaluation of the most relevant data like the volume of the interaction zone and the average volume fractions of the three components - melt, steam, and water particles - inside of this zone, all of them as functions of time, is briefly described in the following. For more details see Appendix F. Two basic relations concerning the interaction zone are

Volume of steam $\approx$ volume of level rise - volume of melt.

Volume of liquid $\approx$ volume of interaction zone - volume of steam - volume of melt.

The volumes of the interaction zone and the melt were calculated from the boundary lines mentioned above and from the calculated melt release, respectively. The actual water level is considered as the upper boundary of the interaction zone. The volume of the level rise is obtained from the measurement.

Local distributions of steam and water in the pool at distinct times are given in Appendices A-D. The phase conditions were determined from the signals for the distinct sites of the void probes, i.e. eight radial and six axial coordinates (see Fig. 1). During evaluation, the data, recorded at a frequency of one Kilohertz, were averaged by passing a gliding window, having a width of 10 data points, over the data. By this, one obtains information about local phase conditions averaged over a time period of 0.01 s. One lastly gets a 8x6 matrix of numbers ranging from zero (=liquid water) to one (=steam) which is figured as data points in an r-z plot, e.g., see Fig. A14. Elevation of the points from the base line indicating the height of the probe and the change of their colour indicate the fraction from zero (black) to one (elev. 4 mm, white).

Jet break-up length When plotting the axial height of the leading edge of the melt jet, we sometimes observe a sudden change in penetration speed at a certain depth. We interprete such a change as indicating that the melt jet was compact up to this depth and was broken below. Unfortunately, not always such a clear change occurred. An additional information comes from the thermocouples which tend to be damaged by the compact jet while individual drops may flow around the TC without affecting it. However, this gives only very course and sometimes not reliable information, as even a single drop may damage a TC. The speed of melt penetration was evaluated from film pictures and TC signals. In some cases, the TC indicated the presence of steam (i.e. melt) with varying delay in time, e.g., see Fig. C10.

When the jet penetration length is derived from the data, the initial height of the water surface must be accounted for. The jet break-up results of all tests are discussed in Section 5.6.

Post-test examination Major points were the mass balances of melt and water, respectively, sieve and chemical analyses of the melt fragments, and gas analysis. From the sieve analysis, the mass mean diameter was calculated using the relation

$$d_m = 1/M \ \Sigma (m_i d_i),$$

where M is the total mass of the melt debris, m_i and d_i are the mass fraction and the mean fragment size of the various shares within the size spectrum. The total surface of the fragments was calculated from the mean diameters assuming spherical particles.

5. RESULTS

The objective of this chapter is to discuss essential results of all (seven) tests, such as the time histories of the melt release, melt penetration, and energy transfer, the increase in pressure, and the development of the interaction zone including its composition. By this, the influence of the various parameters on the results is shown.

Results of the PM12, PM13, and PM14 test series have been reported in detail earlier /8/.

Relevant measurements of the PM15, PM16, PM17, and PM18 tests are given in the Appendices A, B, C, and D, respectively, at the end of this report. It should be noted here that additional information on the results can be obtained by personal observation of the video and high speed films. Copies of films can be made available on request.

5.1. Tests PM12, PM13, and PM14

Introductory remarks

The purpose of the three tests was to demonstrate reproducibility of the PREMIX experiments and to generate a standard data base. It was intended to set identical starting conditions. In fact, small variations occurred due to statistics in the speed of thermite reaction which directly influences threshold values of the monitoring system. In PM12, additionally, a small overfilling of the crucible occurred. The actual test conditions are given in Table III. Unfortunately, the steam flow measurement failed in PM12. In the following, attention is also paid to those items that are supposed to be responsible for the (small) deviations found in the results.

Melt release. Pressures measurements

Figure 3 shows pressure conditions for the time around the start of melt release. Due to the advance of the chemical reaction and depending on threshold values set by the control system, PM14 was started with the largest pressure in the crucible.

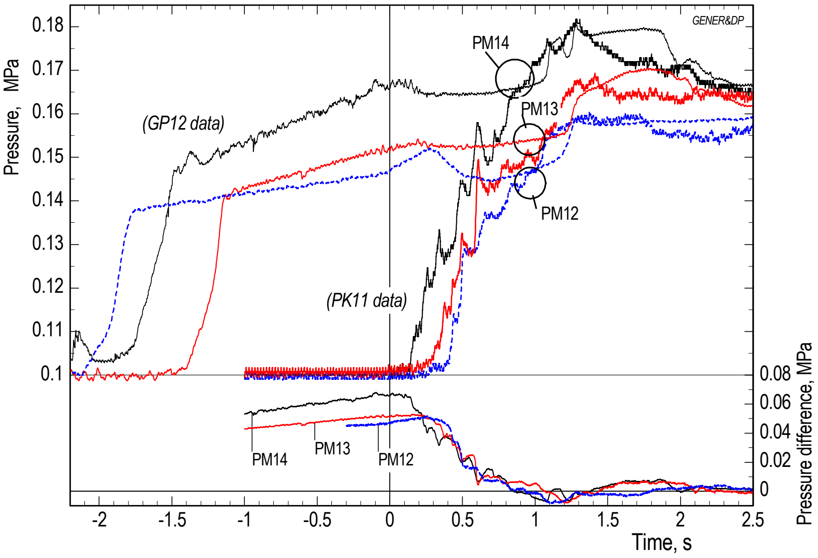

Fig. 3: Pressures determining the melt release: GP12 (in the melt generator), PK11 (in the water pool at –1065 mm), and the resulting pressure difference.

The larger driving pressure led to a larger speed of melt than in the two other tests (see the results of the calculation in Fig. 4) and, consequently, to an earlier rise in the pressure in the pool due to thermal interaction. The decrease in the pressure difference (lower part of Fig. 3) occurred earlier in PM14, too, so that from time 0.45 seconds on, in all tests, both amount and decline of the pressure difference were about the same. It was again in PM14, where the maximum pressure in the water (Fig. 5) was measured. After the maxima, the pressures came closer together.

The start of calculation (Fig. 4) was adjusted in time in order to obtain the first melt/water contact at zero time. The pictures show that the penetration of the melt in the water, visible in the film data, occurred at a slower pace compared to the speed of the melt leaving the nozzle. Note that the maximum speed is almost reached at the time of the first melt/water contact. We attribute this result to the higher driving pressure (compared to that in PM16-18, see below).

All pressure transducers positioned under water showed rather congruent pressure time histories in a test, while the transducers in the gas compartment show marked differences (not presented here).

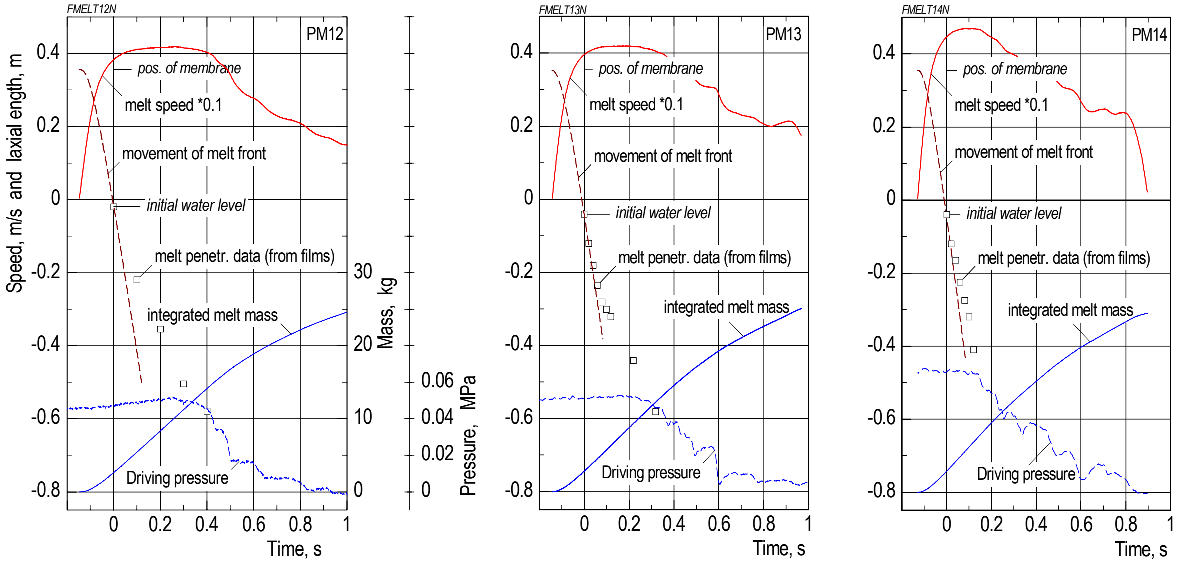

Fig. 4: Calculation of melt release. The calculation started at the time each assumed for membrane break.

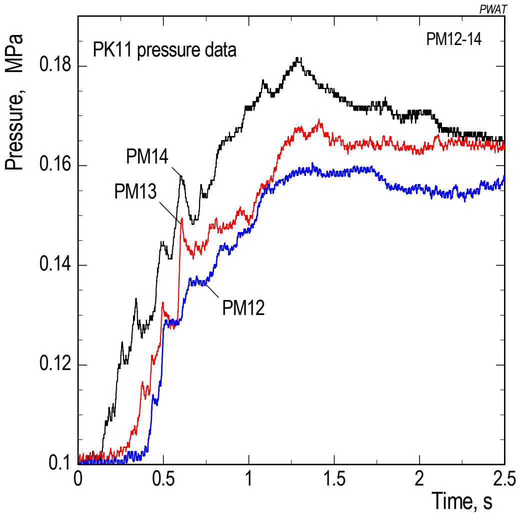

Fig. 5: Pressures measured in the water at -1065 mm height.

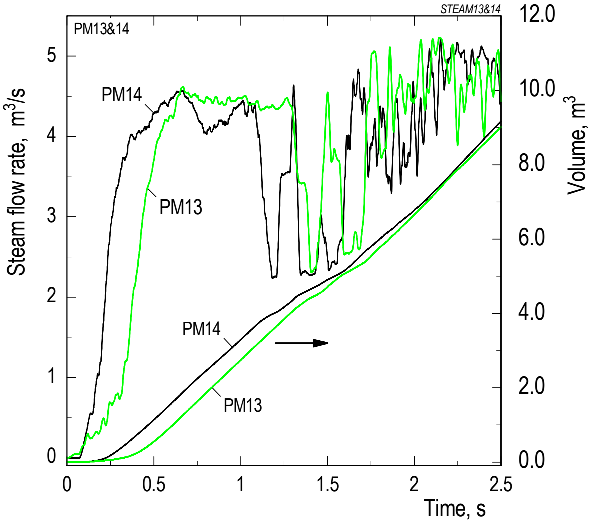

Fig. 6: Steam volume flow rates and the integrated steam volumes

Steam flow

The onset of significant steam flow (Fig. 6) occurred in PM13 and PM14 at the same time but soon after developed differently. After the first maxima, around 0.65 s, the pressure losses connected with the steam flow rate obviously increased with time as the pressure continued to increase (Fig. 5) while the steam flow rate remained approximately constant. While having confidence in the measurements, we presume that a kind of critical mass flow (choking flow) developed across the steam flow path. The movement into and along the annular compartment of the front of a two-phase flow pattern could well be observed in the void signals (changes from gas to gas/droplet environment). In this, larger water fractions were seen more close to the vessel wall.

Later, after the end of melt release, repeated break-downs are seen in the signals. We attribute these disturbances to temporary flow blockages, possibly occurring at the pipe entrance, caused by water slugs carried up with the steam. The measurements show that only two venting pipes were concerned, up to two at the same time. After the time of about two seconds, the flow disturbances disappeared again. It should be noted here that the water separators were not able to retain all the water carried with the steam.

Energy transfer

The quenching rate can be taken as a means to compare heat transfer conditions of various experiments. Under the conditions given initially (i.e. saturated water, heated structure), it was calculated, in a first approximation, from the steam flow rate using the evaporation enthalpy as a multiplying factor. The result is given in Fig. 7, where the quenching rate and the energy are drawn.

While starting at about the same rate, the energy curves diverge from about 4 seconds on. After six and eight seconds, when the flow data took on very small values, the energy transferred was 25 and 33 MJ in PM14 and PM13, respectively. These numbers correspond to 24 and 32%, respectively, of the melt enthalpy above 373 K (= boiling temperature of the water).

The reason for the earlier decrease in the quenching rate in PM14 is not clear to us yet. It may correspond to larger particle diameters found in the post-test particle size distribution (see below) which would result in a smaller total surface available for heat transfer. On the other hand, the films give the impression that, after the end of the melt release, boiling lastly became more violent in PM14.

Rise of the water level

It was in PM14 where the first significant level rise as well as the largest increase occurred (Fig. 8). This is in agreement with the pressure data discussed before and the growth rates of interaction volume (see below).

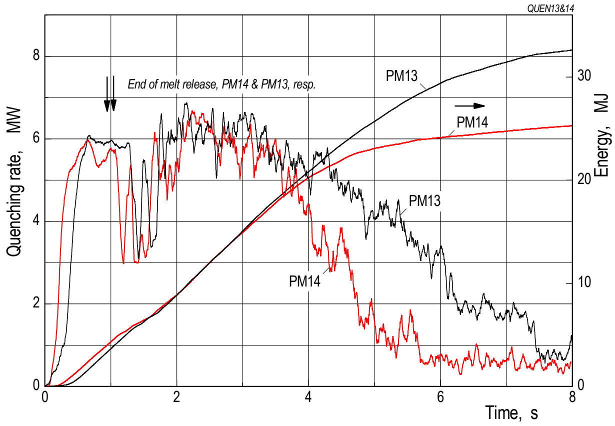

Fig. 7: Quenching rate estimated from the steam flow data and the integrated heat transferred from the melt to the water.

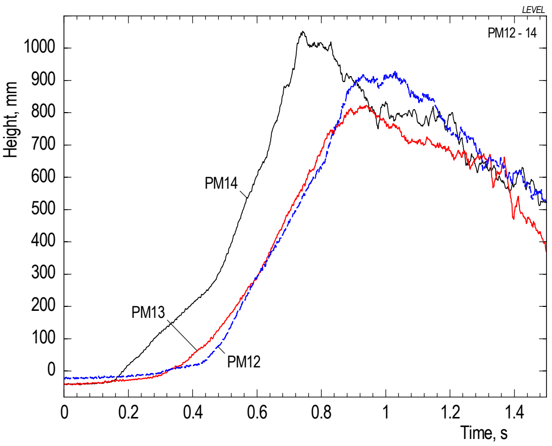

Fig. 8: Water level measurements.

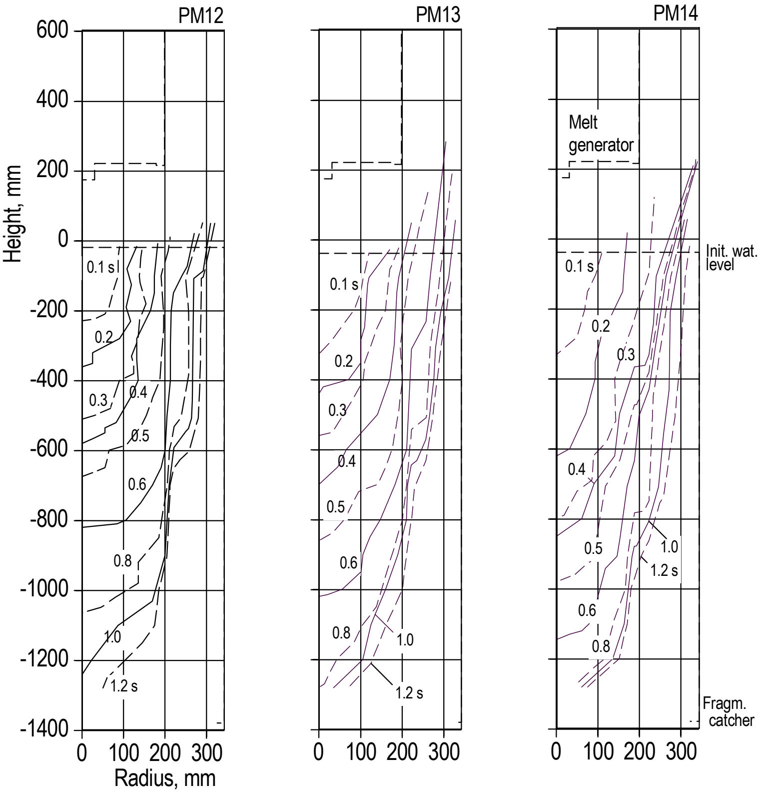

Fig. 9: Progression of the interaction zone into the water with the time as a parameter. The contour lines have been evaluated from the first changes in the void sensor signals and from film pictures.

It should be noted here that, especially during the later period of increase, when bubbles from the interaction region laterally moved into regions near the vessel wall, the measurement gave too low level data (cf. Chapter 2).

Development of the interaction zone

The different melt ejection speeds led to different melt penetration rates in axial as well as in radial direction. This can be taken from the lines in Fig. 9, which have been constructed using characteristic changes in the void signals as well as film pictures. The films also show that in PM12, unlike in PM13 and PM14, melt penetration temporarily occurred with a small offset from the vessel axis.

Volumes and average volume fractions resulting from the interaction

The graphs in Fig. 10 (top) show the growth rate of the essential volume, i.e. the volume of the interaction zone, increased from test PM12 to PM14. The time function of the interaction volume was obtained from the contour lines in Fig. 9. while the actual water level was taken as the upper boundary. The other volumes were gained as described above.

Another important result is that the average volume fractions (bottom of Fig. 10) behave rather similar in all tests. Starting from large initial values, the liquid fractions decreased gradually and approached values around 50 ±10 % after 0.4 – 0.5 s. On the other hand, the steam fractions, starting from low levels (time > 0), showed steep individual increases which can be correlated to sudden increases in boiling intensity. The times when these increases started differ from test to test (0.15, 0.27, and 0.43 s in PM14, PM13, and PM12, respectively). These times seem to be the shorter the larger the initial melt penetration speed was.

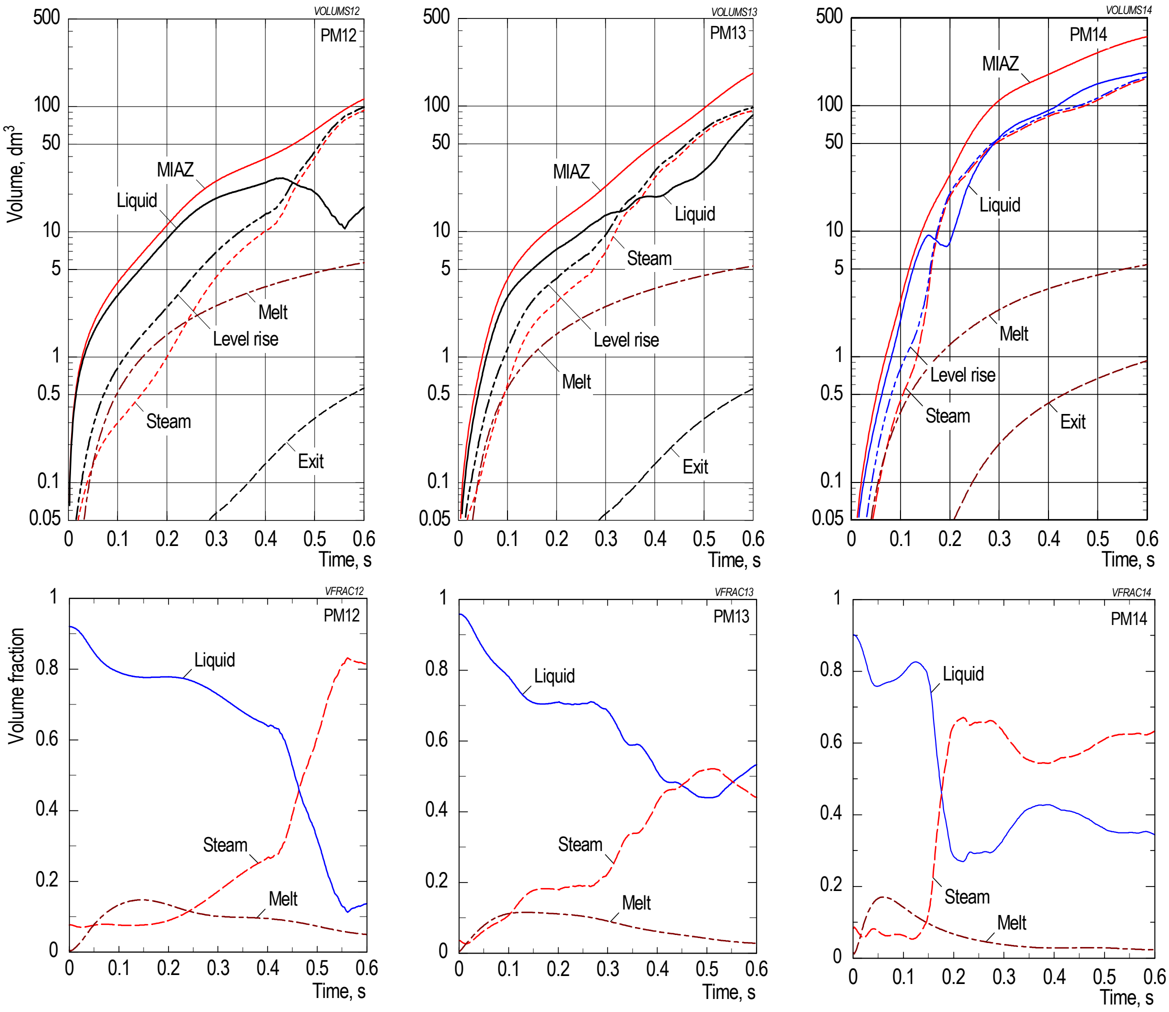

Fig. 10: Volumes resulting from the interaction (top) and the derived average volume fractions. MIAZ = multiphase interaction zone.

It should also be noted that reliable results were obtained only from about 50 milliseconds on, since the evaluated data start at absolutely very small values which implies that a relatively large error exists in the early data.

Jet break-up length

The jet penetration data have been reported in Ref. /8/. No clear change in penetration speed is observed in them. Sometimes, the speed is reduced temporarily, but resumes the same or a similar value afterwards. (These reductions may have been caused by local interactions that fragmented the leading edge of the jet.) Therefore, no break-up length can be derived from these data.

Table IV: Jet break-up lengths and a few characteristic data.

Exp.	Melt speed[1] [m/s]	Melt mass [kg]	Length from TC damage [mm]
PM12	3.8 – 4.2	29.0	895 < L < 1095
PM13	4.0 – 4.2	23.8	1075 < L < 1175
PM14	4.5 – 4.7	23.2	L > 1175

[1] on first melt/water contact – maximum; both values are calculated; (see Fig. 4).

The data derived from thermocouple damage are compiled in Table IV. It shows that the higher the melt speed was, the larger was the penetration distance of the jet in a compact form.

Sieve analysis

The result of the sieve analyses (Fig. 11) and the mean mass diameters listed in the small table below show finer fragments in PM14. The particles were recovered from the various sites within the test facility: fragment catcher, bottom of the vessel, and water separators. The result listed in the small table below does not really reflect the finding of the sieve analysis which should give the largest total surface in PM14. Among others, two reasons for the deviation are possible: errors arising from the shape assumed to be spherical and a loss of very fine melt particles transported out of the facility by the steam.

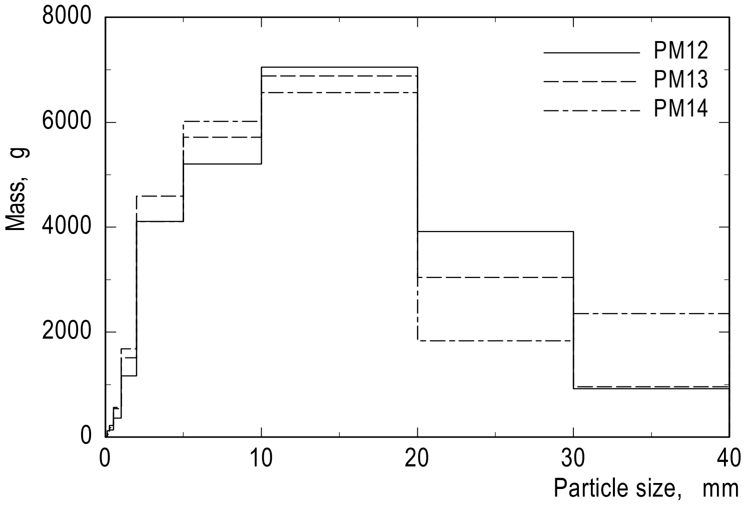

Fig. 11: Post test particle size distribution of fragments.

Figure 12 shows photographs of examples of fragments which were collected at two different sites. The samples are more or less typical of all PREMIX tests: roundish particles, partly porous, partly hollow, on one hand, and fragments of irregular shape on the other. Obviously, solidification occurred in a turbulent environment. The pictures indicate that the assumption of spherical particles in calculating the total surface, resulted in a minimum surface area. Presumably, the real surface was at least twice as large.

	PM12	PM13	PM14
Mean mass diameter, mm	10.5	9.91	9.47
Total surface, m^2	10.17	10.84	9.53

The Sauter mean diameter (i.e. the average mean diameter referred to the surface assuming spherical particles and a density of 3000 kg/m^3) of the post-test melt fragments in PM13 and PM14 was 4.38 mm and 4.96 mm, respectively. Details of particle size distributions are given at the end of this chapter.

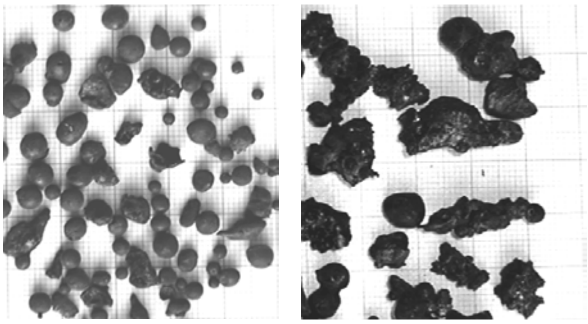
(a) (b)

Fig.12: PM12. Typical shape of fragments collected
(a) at the fragment catcher, sieve fraction 2 – 5 mm
(b) at the bottom of the facility, fraction 5 – 10 mm

Gas analysis

It was for the first time in PM14, that gas samples were drawn at various positions of the facility prior to and during the interaction for time intervals of 0.2 s at different instants. The non-condensable gas that remained in the six samples was analysed by use of a mass spectroscope with respect to hydrogen. This gas could have been the result of a chemical reaction or of steam dissociation. The result was such that the sample drawn prior to the interaction did not contain (of course) any hydrogen, whereas the others contained between 0.4 and 3.7 % hydrogen. No systematic behaviour versus time or location, respectively, could be found.

Summary and conclusions (PM12 – PM14 tests)

The results show that the initial speed played an important role in the subsequent course of the experiment. The higher the speed was, the shorter was the time between first melt/water contact and first marked increases in pressure and steam generation and the more violent was the interaction.

We conclude that, besides the variations due to the initial jet velocities, the results of the PREMIX experiments are reproducible.

5.2. Test PM15

This test was performed to investigate the influence of an increased system pressure (0.5 MPa compared to 0.1 MPa). Comparison of essential data with PM13 seems reasonable since the other test conditions were approximately the same. At first, information about the melt release in PM15 is presented.

Melt release

The pressures controlling the melt release in PM15 are given in Appendix A, Fig. A3. The way in which the melt penetrated into the water is illustrated by film pictures in Fig. A1

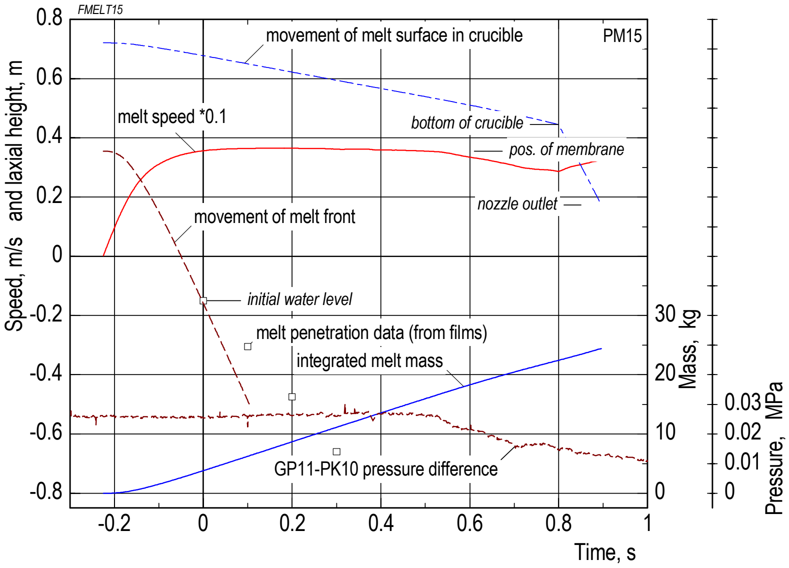

Fig. 13: Calculation of melt release. The calculation was started at the time assumed for steel membrane break.

Figure 13 gives results of the calculation together with melt penetration data. The picture shows that, as in PM12 - PM14, the penetration of the melt in the water occurred at a slower pace compared to the speed of the melt leaving the nozzle. The given mass of melt, 23.1 kg, was released within a time period of 1.1 s. At the time of 1.3 s, the pressure difference became zero (see Fig. A3) indicating the end of the melt release in the test.

The mixing zone formed by the interaction in PM15 had a rather slim shape. Compare for this the frames in Fig. A1 with those of PM13 in Fig. 2. The smaller radial extension of the mixing zone is attributed to the larger system pressure as well as to a small amount of water subcooling (see further discussions below).

Pressure and steam flow data

Figures 14 and 15 give time histories of the pressure rise and the steam flow rate, respectively. Due to the larger system pressure, the pressure increase as well as the

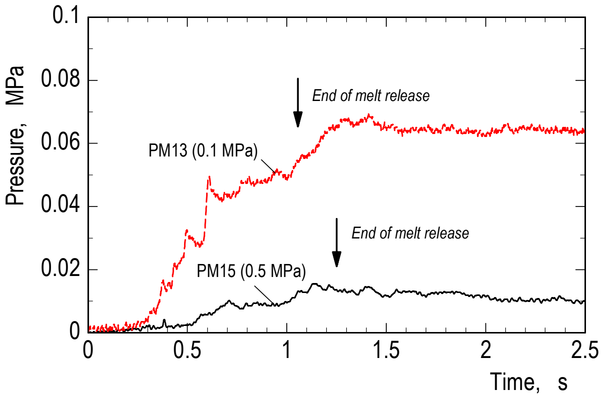

Fig. 14: Time history of the pressure rise obtained in the water at –465 mm height.

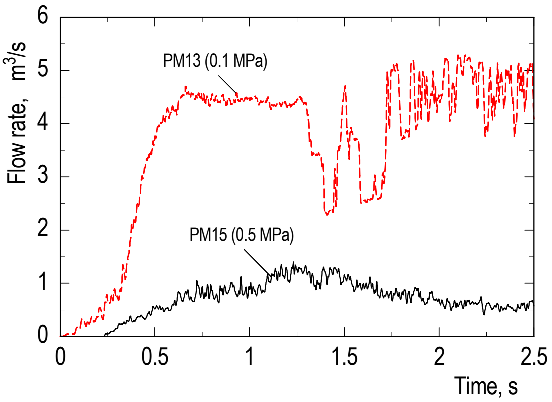

Fig. 15: Steam volume flow data.

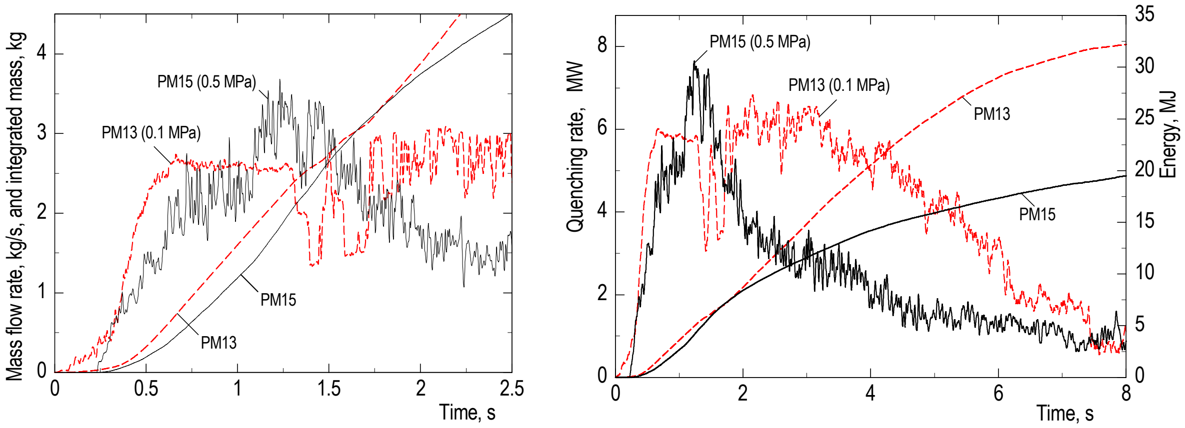

(a) (b)

Fig. 16: Steam mass flow data (a) and the derived quenching rates and energies transferred (b)

volume flow rate were smaller in PM15 than in PM13 by factors of 1/4 to 1/5. These numbers compare well with the ratio of the respective mean steam densities (0.22).

On the other hand, the steam *mass* flow rates (Fig. 16a) compare better. While starting to increase later, the steam mass flow rate in PM15 reached 85% of the first peak value of PM13 after one second. The following maximum mass flow rates were larger in PM15 than in PM13. As already stated, the break-downs in the PM13 steam flow signal were caused by excessive fractions of water temporarily carried with the steam through the venting pipes.

Substantial rises in the pressure and steam flow rates occurred in both tests a short time after the first melt/water contact, typically 0.1 – 0.3 s. This is a general result of all PREMIX experiments performed with saturated or almost saturated water. The somewhat larger delay in PM15 (0.25 s), can be attributed to the presence of a small amount of subcooling (ΔT_{sub}=8 K).

Energy transfer

The quenching rate was calculated, as described in the preceding chapter, from the steam flow rate. The amount of heat required to compensate the small water subcooling was negligible (<2%). The result of the calculation is given, together with the energy transferred, in Fig. 16b in a larger time scale.

The quenching rate decreased earlier in PM15. Consequently, the transferred energy reached lower values only. This might be a consequence of the larger particles formed in PM15 (see below).

Leaving apart the influence of other variables, one can deduce from the finding in Fig. 16 that the heat transfer between melt and water in the initial period of interaction was only little influenced by the system pressure.

Development of the interaction zone

Progression of the interaction zone into the water is drawn in Fig. 17a or the two experiments PM13 and PM15 with the time as a parameter. The upper ends of the lines in PM15 agree, up to the time of 1.0 s, with the level data (see Fig. 24 below). The comparison with PM13 shows the influence of the larger system pressure: The slim shape of the multiphase channel in PM15 is an effect of the larger pressure. It should be noted here that the melt release time was somewhat larger in PM15 than in PM13 (1.25 s compared to 1.05 s).

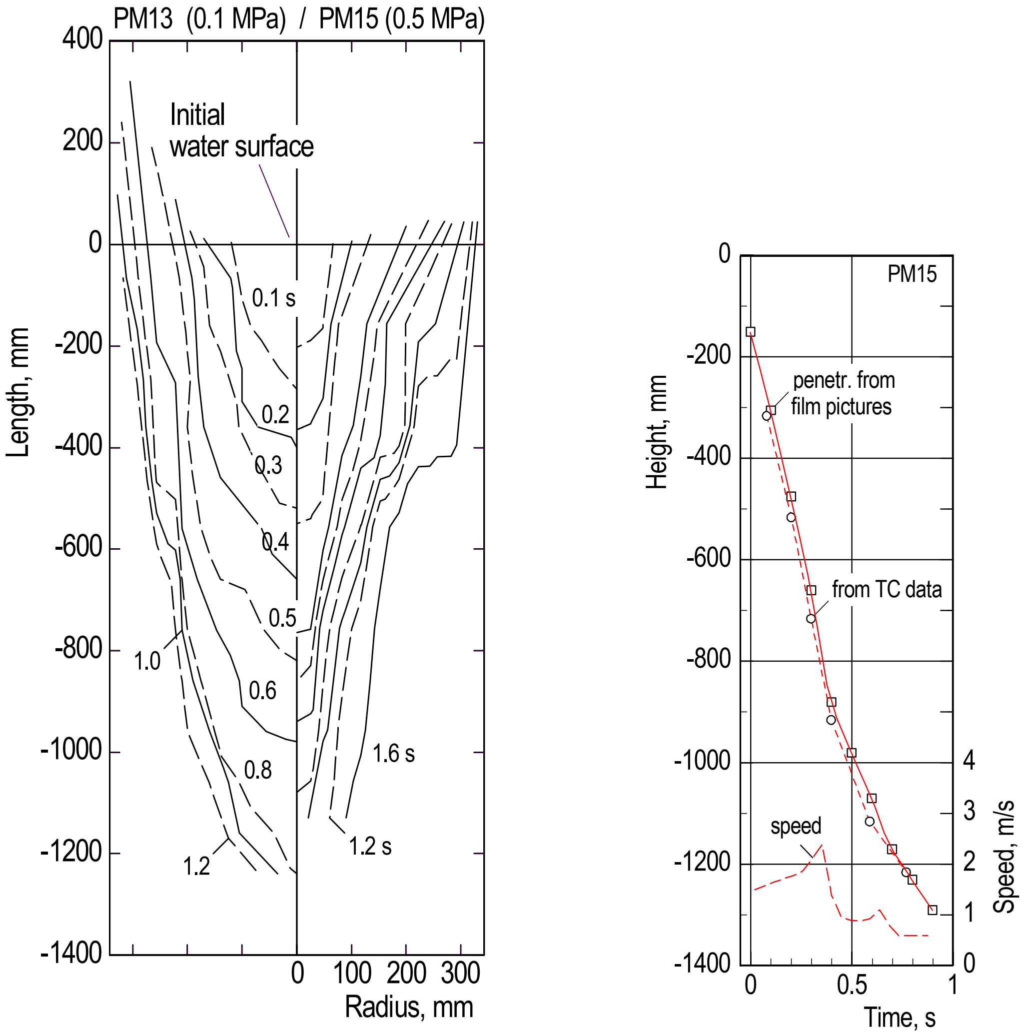

(a) (b)

Fig. 17: Developments of the interaction zone in the axial and radial directions in PM15 and PM13, respectively, with the time as a parameter (a). The axial melt progression in PM15 and the speed derived from the film data are shown on the right side.

The progression of the melt front in PM15 (Fig. 17b) evaluated from the films is confirmed by the thermocouple data. Note that the progression line shows a distinct bend at the height of -910 mm. The latter value is used in the finding of the jet break-up length (760 mm, see below).

Jet break-up length

The jet break-up length in PM15, derived from the time history of axial penetration (Fig. 17b), was found to be L ≈ 730 mm (first strong reduction of penetration rate at the height –880 mm). The conclusion to be made from the TC readings (see Fig. A9) is not so easy: The T12 and T13 TCs were not damaged, T14 TC (-1115 mm) was damaged at 0.65 s. From these findings, one can conclude L>965 mm.

Volumes and average volume fractions

The influence of the larger system pressure on the growth rate of the interaction volume is shown in Fig. 18 where the results of PM15 are compared with those of PM13 . The growth rate was much smaller in PM15. The average volume fractions of steam and liquid oscillated, after the initial period of 0.2 to 0.3 s, around a mean value of 0.5.

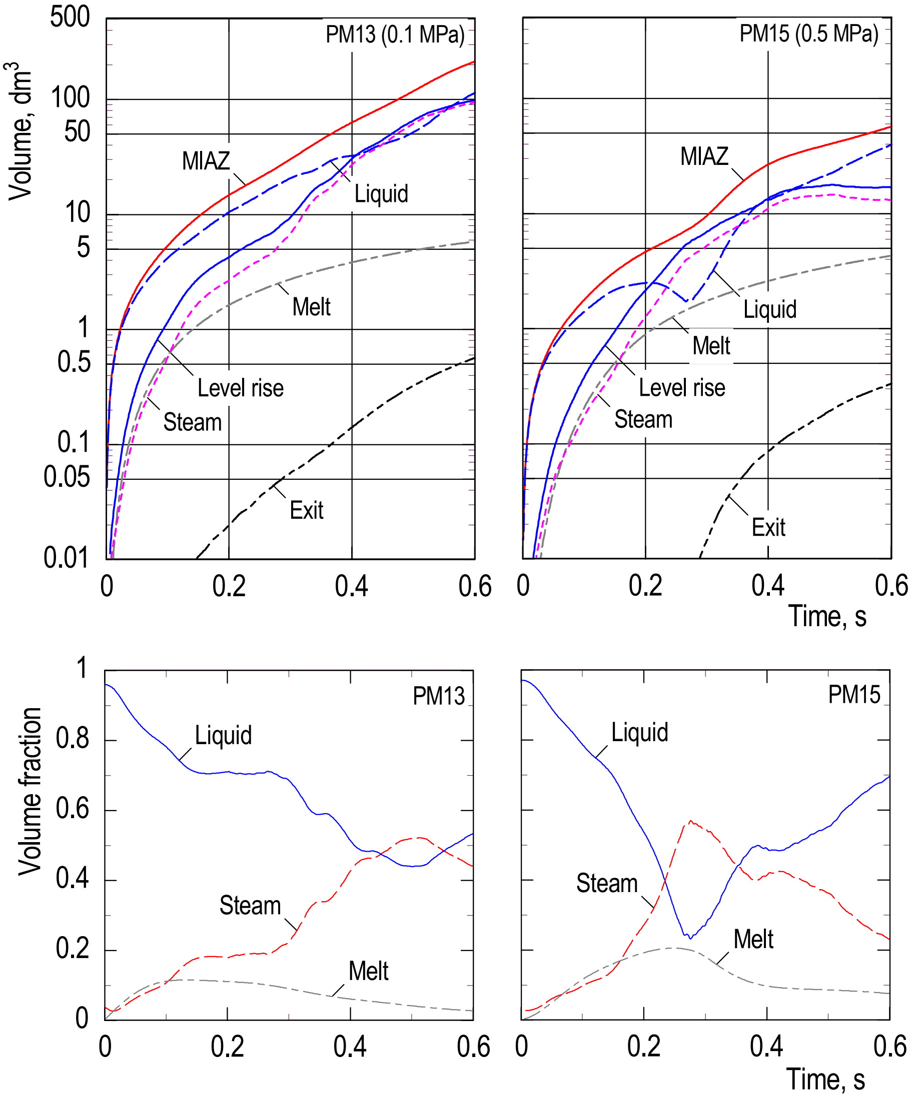

Fig. 18: Volumes resulting from the interaction and the derived average volume fractions. MIAZ = multiphase interaction zone

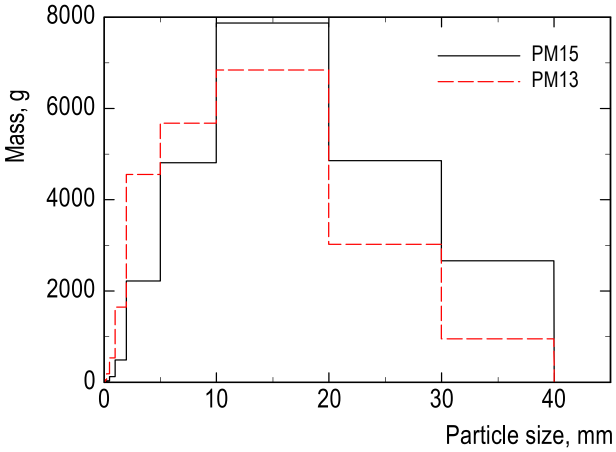

Fig. 19: Post test particle size distribution of the fragments collected at the fragment catcher, at the bottom of the facility, and from the water separators.

Post test investigations

The post-test particle size distribution of the melt fragments (Fig. 19) shows a shift towards larger sizes for the test with the larger system pressure (PM15). Larger particles would result in a smaller total surface. If the post-test distribution was given also during the first second of interaction, one could explain by this the smaller rate in the steam mass production shown in Fig. 16a.

In the gas probes taken during the interaction no hydrogen was found whereas the probe taken prior to the test showed 0.8 % hydrogen. We can not give an explanation for this result yet.

5.3. Test PM16

The conditions of this test were chosen to study the influence on the mixing of a larger melt mass released in a longer time than in the earlier PREMIX tests and to allow better comparison with the L-28 FARO test.

The *volume* of the melt mass and the nozzle diameter, 50 mm, were chosen to agree with that in L-28. To achieve the same release time, about 6 s, nearly gravity conditions were required. To this end, it was tried to keep the pressure difference between melt generator and interaction zone at a level of about 0.01 MPa by the control system described above.

Melt release

The pressures controlling the melt release in PM16 are given in Fig. B3; the way in which the melt penetrated into the water is illustrated by film pictures in Fig. B1.

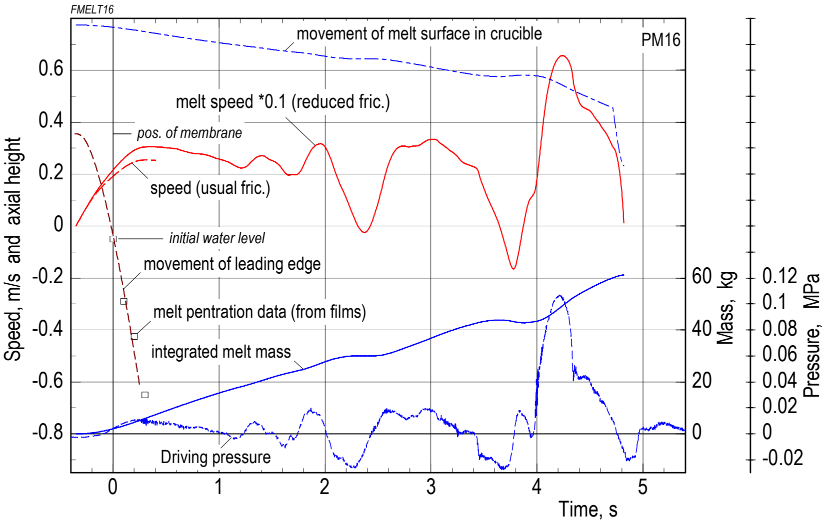

Fig. 20: Calculation of melt release.

Figure 20 gives results of the calculation of melt release together with melt penetration data. Note that the major results shown were obtained using somewhat reduced friction coefficients compared to those used in all other tests. (Use of usual friction coefficients led to a melt release time much longer than observed in the test. We attribute this to the strong pressure oscillations discussed below). The “movement of the leading edge” line was obtained using usual friction coefficients.

The control system, applied in PM16 for the first time, allowed strong oscillations in the pressure difference. The reason was that steep pressure rises occurred in the interaction zone which were not expected. These could not be compensated fast enough by the control system. The oscillations in the pressure difference caused similar oscillations in the speed. These were such that conditions of almost and complete flow reversals occurred at 2.4 and 3.7 s, respectively. We presume that, at the second time (3.7 s), water penetrated into the crucible where it was evaporated in a flash. This event caused the pressure in the crucible to increase steeply and, by this, the melt release to go on. The probable end of melt release was around 5.0 s, indicated by equalisation of the pressure inside and outside of the melt generator.

Pressure and steam flow data

Comparison of pressure and quenching data with those of PM15 seems reasonable (comparison with L-28 is made below). In both tests, the water conditions were the same whereas the melt release modes were different. Melt release in PM15, which occurred under constant crucible pressure, was finished at about the time when a substantial portion of melt had reached the fragment catcher. Melt release in PM16 was characterised by driving forces near gravity, by a much larger melt mass, and a smaller nozzle diameter. Under these conditions, the release time exceeded by far the time after which fragments began to settle on the fragment catcher.

Pressures measured in the water are given in Fig. 21, steam flow data in Fig. 22. The pressure increased in both tests as long as melt was delivered. This resulted in a much higher peak pressure in PM16. The oscillations in the pressure are approxi-

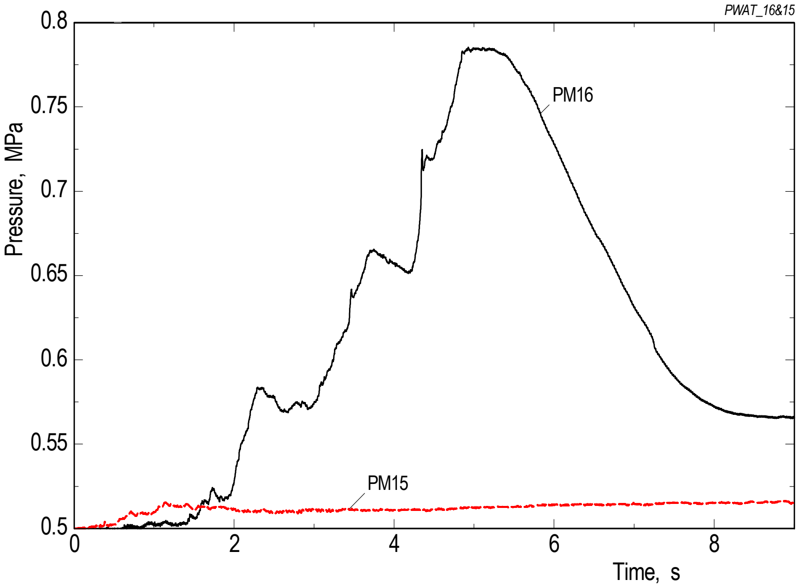

Fig. 21: Pressures measured in the water at –1065 mm height.

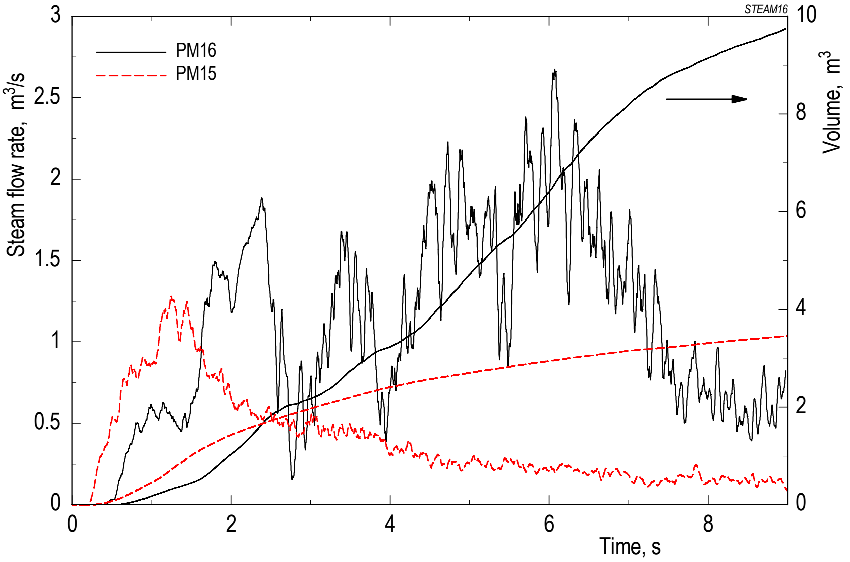

Fig. 22: Volume flow rates and integrated volumes of the steam.

mately in phase with those in the steam flow rate. We suppose that the steam flow oscillations were caused by varying fractions of water dragged with the steam as large drops or slugs which caused, as observed in the PM13 and PM14 tests, temporary flow blockages at the entrance to the steam venting pipes.

Energy transfer data

The quenching rate was calculated, as described above, from the steam flow rate. The result is given in Fig. 23 together with the integrated energy transferred. The steam flow and with it the quenching rate reached a maximum at 6 seconds. This is about the time when the majority of the melt had arrived at the fragment catcher.

The energies transferred during the first nine seconds are given, together with the melt masses, in the small table below. The energy in PM16 is by a factor of about 2.7 larger than that in PM15. This number agrees with the ratio of the melt masses in both experiments. Another information can be gained: The energy transferred up to nine seconds corresponds to 20 % of the heat content of the melt above the saturation temperature at 0.5 MPa.

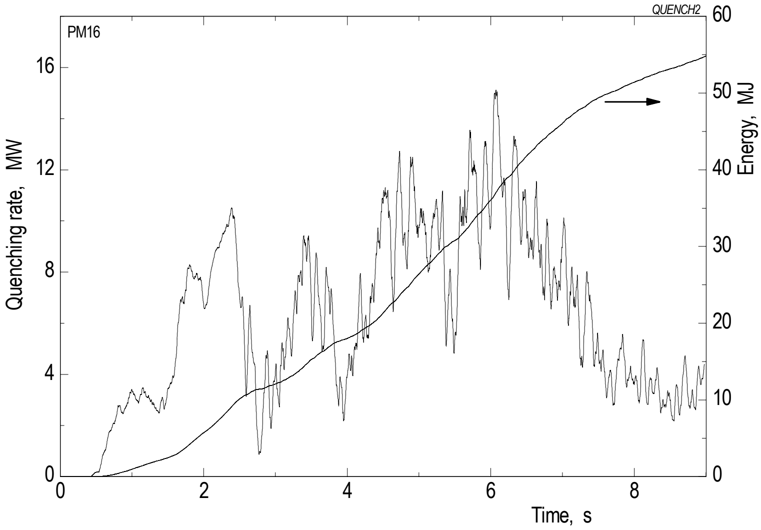

Fig. 23: Quenching rate and integrated energy transfer.

The increase in the water level gives an important piece of information about the growth rate of the interaction zone. In contrast with previous tests performed with saturated water at normal pressure conditions, where the level rise occurred more continuously, the level increased hesitantly in PM16 and PM15 (compare Fig. 24 with Fig. 8). In analysing this behaviour, firstly the different test conditions have to be considered: (1) the higher system pressure which leads to a smaller steam density, (2) a small initial subcooling of the water (cf. Table III).

	PM16	PM15
Mass released, kg	60.4	23.1
Heat transferred up to 9 s, MJ	55	20
Water dragged with the steam, kg	57	27

The presence of subcooled bulk water caused some portion of the steam produced to condense in situ. The effect was even more pronounced in the tests with larger subcooling; see PM17 and PM18 below.

In the further analysis of the initial level rises in PM16 and PM15 (see the larger-scale graph in Fig. 24), one finds that the steep initial increases ended at about the times when (a) jet break-up was assumed in PM15 at 0.4 s (see Fig.17), (b) the melt front approached the fragment catcher in PM16 at 0.8 s (see Fig. 28). The halts that followed the initial rises lasted about 0.7 s each. Note that during the stagnation in the water level, melt continued to enter into the mixing zone (see the “level swell” lines); the pressure in the mixing zone slightly increased (e.g. by 0.003 MPa in PM16, see Fig. B4) while the steam flow rate stagnated similarly (Fig. B7). Around the end of stagnation period, melt material began to settle on the fragment catcher. This led

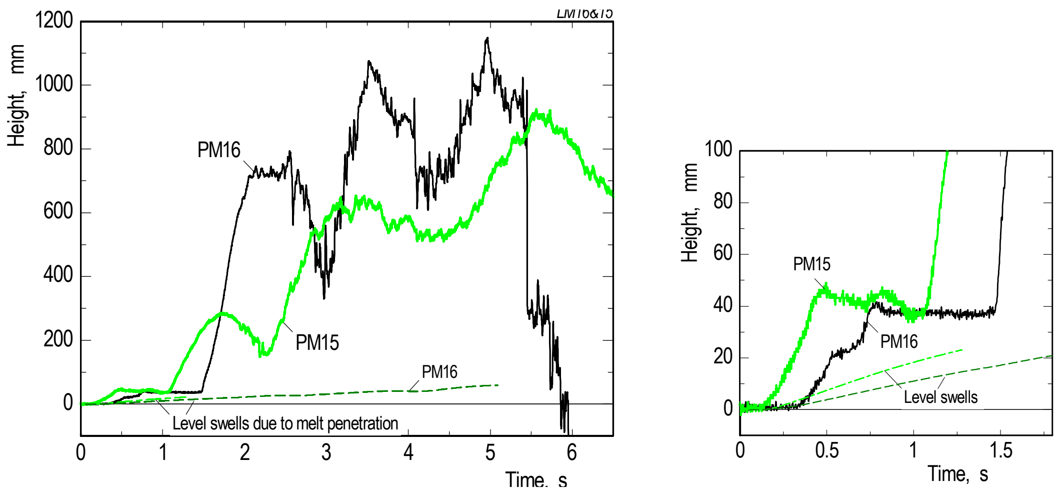

Fig. 24: Change of the water level measured. The level swell calculated on basis of the melt entering the mixing zone, where one kilogramm of melt approximately corresponds to one millimeter in height, is shown for comparison.

to an increase in fragmentation which gave rise to the increased evaporation mentioned and to essential level rises in PM16 and PM15 (Fig. 24).

A more detailed analysis can only be made by use of a multiphase computer code. (The drop in the PM16 level signal around 5 s was because the water level fell below the lower end of the level probe.)

The course of events in PM16 during melt release was characterized by strong oscillations evident in the time histories of pressure, steam flow rate, and water level (Figs. 21, 22, and 24). We are sure that this is a consequence of the oscillatory nature of the driving pressure. Applied in PM16 for the first time, the procedure was improved in the following tests.

Volumes and average volumes

These results are discussed together with those of PM17 below.

Jet break-up length

A jet break-up length of L ≈ 790 mm could be derived from the rate of axial penetration (Fig. B12). Slow-down of the rate occurred at the height of -840 mm at 0.4s. An additional information is that the T12 thermocouple, located at –915 mm, was damaged at 1.22 s, i.e. about half a second after the passage of the melt had been indicated by a small signal increase (see the TC data in Fig. B9). We conclude from this that jet break-up occurred above the height –915 mm which gives for the break-up length 665 > L > 865 mm.

Post test investigations

A large fraction of fine particles was found in PM16 (Fig. 25). This may explain the larger violence of the melt/water interaction observed in the films. About half the debris was found in PM16 as particles, the other as cake which was not considered in the data given in the figure. No cake was formed in PM15.

The larger violence of the interaction can also be deduced from the amount of water that was dragged with the steam and partly retained in the water separators. The water masses are listed in the above small table. We assume that steam condensation in the water separators can be excluded, because all structures were heated prior to test above boiling temperature.

No finite melt jet break-up length can be stated in PM16 since all thermocouples near the vessel axis were damaged. We conclude from this finding that a compact melt stream existed until the melt front arrived at the fragment catcher, i.e. L>1175 mm.

No hydrogen measurements were performed in PM16 because no substantial amount of hydrogen had been found in the previous test.

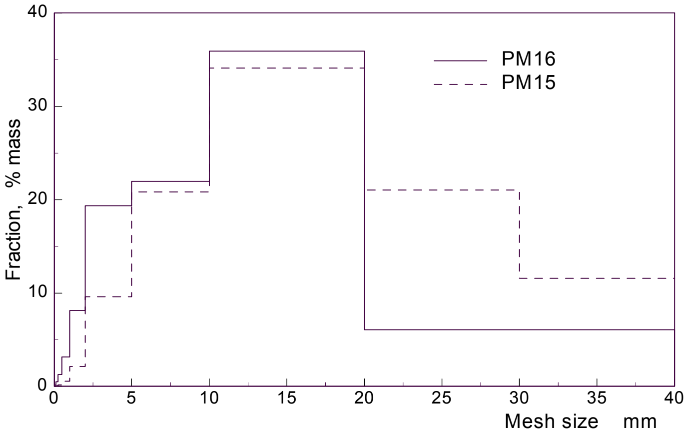

Fig. 25: Post test particle size distribution of the fragments.

5.4. Test PM17

Melt release

The main features of PM17 were a large water subcooling, 104 K, the closure of the venting pipes, and the system pressure (0.22 MPa). With that, similarity to FARO L-31 was achieved.

Figure 26 gives results of the calculation of melt release together with melt penetration data. Due to improvements made in the control system, the pressure difference did not oscillate as much as in the preceding test (PM16).

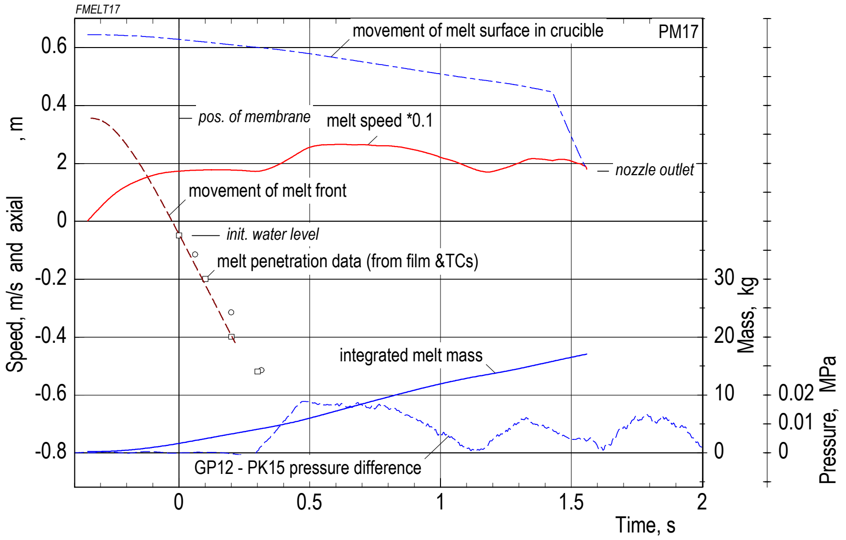

Fig. 26: Calculation of melt release.

The probable end of melt release, around 1.8 s, was indicated by equalisation of the pressure inside and outside of the melt generator. For that time, the melt release amounted to a mass of 16 kg in the calculation.

The films (see Figs. C1 and C2) and measurements show that a slim interaction zone was formed which was open to the water surface at least as long as melt was delivered. Part of the steam left the interaction zone, carrying melt and water particles with it. The V06 void probes, located ≈110 mm above the initial water surface, showed frequent changes between gas and water between 1.0 and 2.5 s. The mixture firstly occupied the volume space between initial water level and nozzle exit forming highly turbulent flow. The annular gas compartment and the closed venting pipes served as additional expansion volumes. No water droplets were indicated by the void probes in the annulus.

Pressure measurements

The pressure increased, due to the closed venting pipes, by 0.06 MPa (Fig. 27). Note that the PK11 pressure trace includes the respective geodetic height of the water. The pressure starts to rise, after the first melt/water contact, with some delay. The maximum, 0.295 MPa, was reached 0.7 s after the end of melt release.

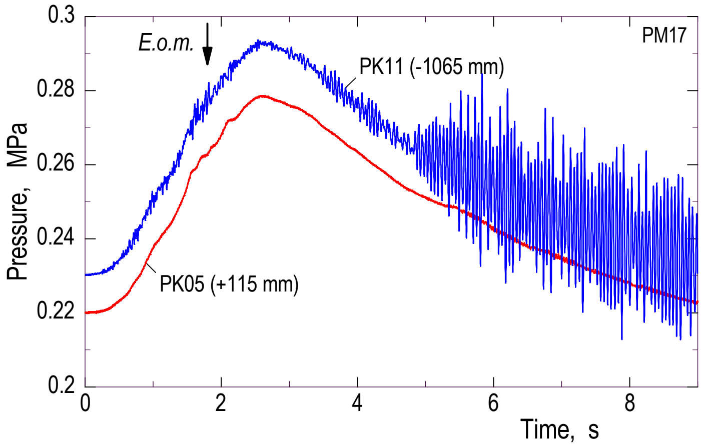

Fig. 27: Pressure obtained in the water (–1065 mm) and in the gas compartment (+115 mm). E.o.m.=end of melt release

Later, during the decrease, the pressure in the water shows superimposed oscillations. Pressures obtained in the gas space do not show these oscillations. I.e., the space above the water was decoupled from the source of oscillations. The oscillations are characterized by frequencies of 19 Hz and peak-to-peak values of up to 0.04 MPa. Pressure oscillations of this kind have not been observed in former PREMIX tests.

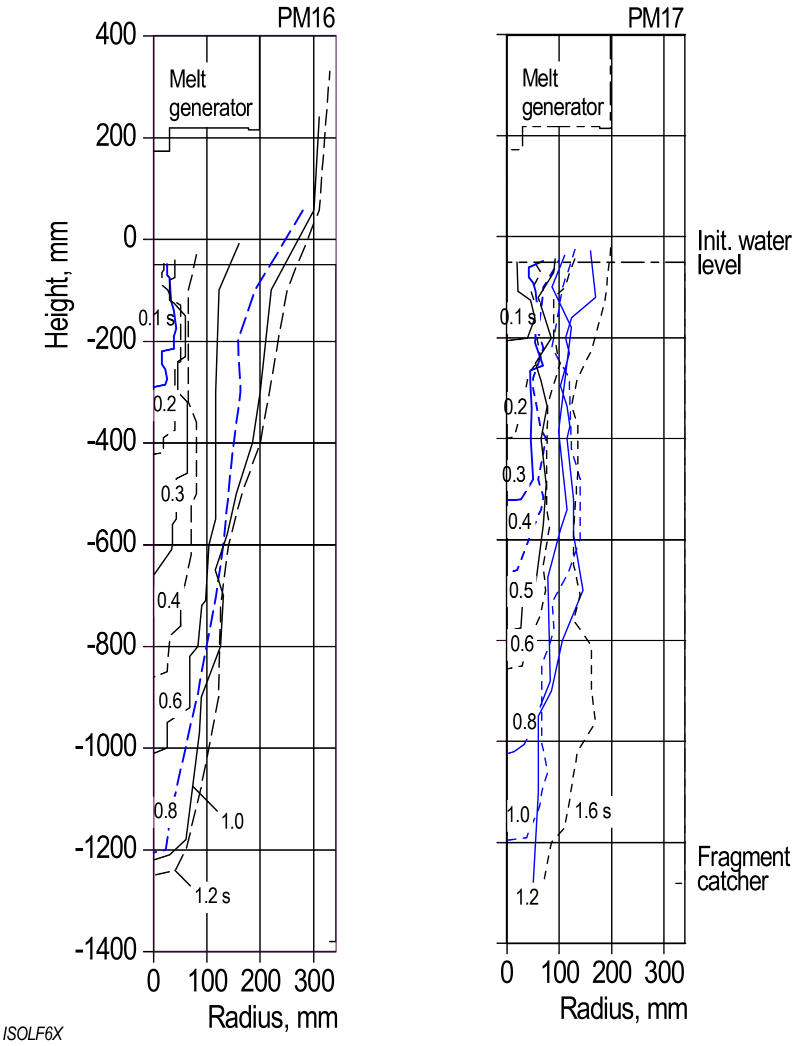

Fig. 28: Development of the interaction zone derived from void signal responses and from the films. Parameter is the time. Essential difference in the test conditions was the water subcooling. PM16: 5 K, PM17: 104 K.

The source of the oscillations appeared to be some sort of subcooled boiling within the water although there is no clear evidence from the films in PM17. However, one gets the impression that the interaction zone was closed at the water surface from 4.8 s on, at which time the oscillations started. More information was gained from films taken in PM18 (see below).

Development of the interaction zone; volumes and volume fractions

The essential difference in the PM17 test conditions (compared to PM16), was besides system pressure and steam expansion capability, the large water subcooling. The melt speeds were comparable during the first second. The progression of the interaction zone in axial and radial directions is depicted in Fig. 28. The comparison with PM16 shows the slim shape in PM17 mentioned above. Comparison is reasonable as long as melt was released (melt release ended in PM17 at 2.0 s). The void measurements, also used in the construction of the contour lines, support the observation made in the films, namely, that the opening of the interaction zone towards the overlying gas space increased with time. The rise of the water level in PM17 was comparatively small (see the upper ends of the contour lines). The maximum extension of the opening, which was about at the end of melt release (1.7 s), was several times larger than the diameter of the melt jet.

Figure 29 shows volumes generated as a consequence of the interaction and average volume fractions of the three components (melt, liquid water, and steam) within the interaction zone. It should be stressed again that reliable results were obtained only from about 50 milliseconds on, since the measurements start at very small absolute values. This results in a relatively large error in the very initial time. After that,

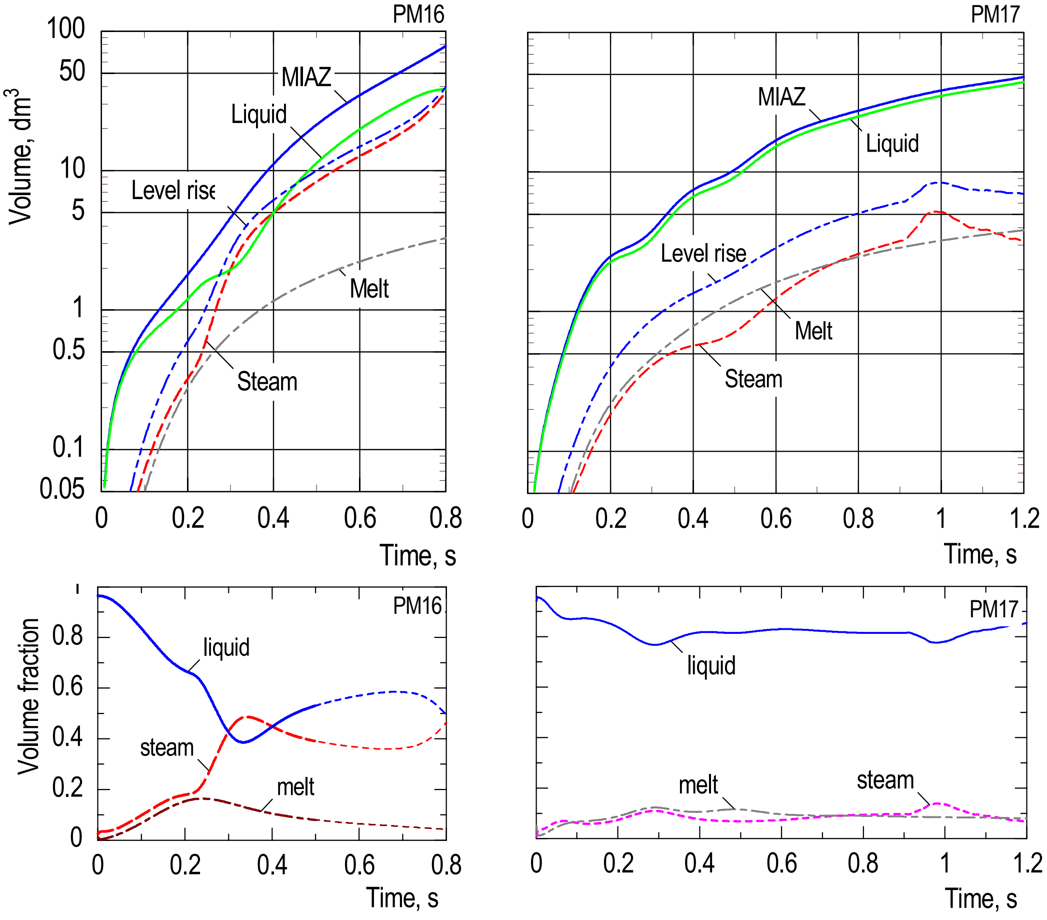

Fig. 29 Volumes resulting from the interaction and the derived volume fractions

reasonable results can be obtained only up to 1.2 s (PM16) and 1.6 s (PM17) because determination of the steam/liquid interface in the pool as well as the upper limit of the interaction zone becomes uncertain.

Jet break-up length

The jet break-up length, derived from Fig. C10, was L ≈630 mm. From the thermocouple readings (Fig. C8), one can only deduce L>465 mm.

Post test investigations

The overwhelming part of the melt fragments was found at the fragment catcher (7.1 kg). A substantial portion of this, 5.9 kg, had formed a solid cake. Smaller amounts were found in the water separators (0.76 kg) and at the bottom of the facility (0.66 kg).

The surface of the cake showed agglomerations of solid particles. The fragments were generally very brittle and tended to break to finer pieces during sampling. A sieve analysis was therefore omitted. Figure 30 shows a large particle formed by agglomeration of drops which obviously are hollow. The picture also shows remainders of drops that have been broken off.

Fig. 30: Particle collected after the test showing broken edges and a shrinking crack.

The analysis of the gas probes showed no hydrogen. The water level increased during the test by about 22 mm. The volume of the increase compares well with the volume of the melt plus the increase in water volume due to temperature increase.

5.5. Test PM18

The objective of the experiment was to investigate quenching under the condition of water subcooling that was less than that in PM17 (=104 K). In doing so, a value of about 30 K was chosen. The other test conditions in PM18 were set as in PM17.

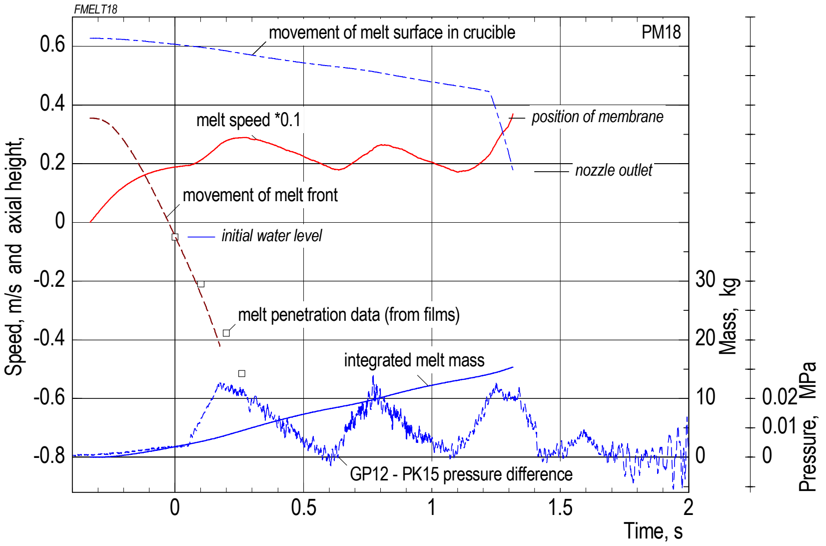

Fig. 31 Calculation of melt release.

Melt release

Figure 31 shows results of the melt release calculation together with melt penetration data. Backfeeding of gas to the crucible atmosphere occurred three times, the first one shortly after the first melt/water contact. The driving pressure varied between zero and 0.02 MPa. The first maximum of the calculated speed, 2.9 m/s at 0.25 s, is larger than that obtained from film evaluation (2.5 m/s, Fig. D13). A mass of 14.6 kg is released after 1.4 seconds.

About at that time, from 1.4 to 1.5 s, pressure equilibrium occurred across the nozzle tube which was due to a short relative minimum in the pressure in the interaction zone (see Fig. D7).

A noticeable result of PM18 is that the mass of melt released as well as the release time were smaller than in PM17 (see Table III). This result can be ascribed to (1) slightly different pressure conditions formed in the melt generator and (2) the faster pressure build-up due to interaction in PM18 (see below). Both conditions influenced the actual response of the control system concerning frequency and rate of gas backfeeding. Eventually, the average driving pressure was slightly larger and so the release time was shorter in PM18 than in PM17.

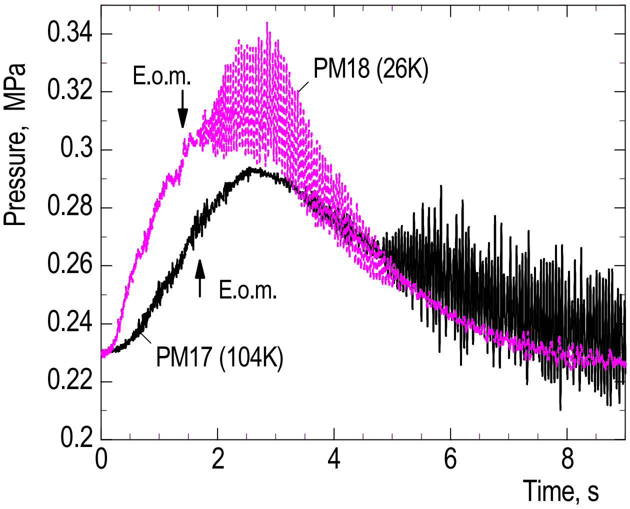

Fig. 32: Pressure readings obtained at –1065 mm height. E.o.m. = end of melt release.

Pressure measurements

Pressures measured in the water in PM18 and PM17 are drawn in Fig. 32. As expected from the lower subcooling, the onset of the pressure rise was earlier and the peak pressure was higher in PM18. As in PM17, pressure oscillations occurred in PM18 where they started earlier. Trying to clear up this appearance, we got the following information from the films.

In PM18, soon after the end of melt release, radial contractions of the interaction zone appeared which varied in size and the axial location. At the

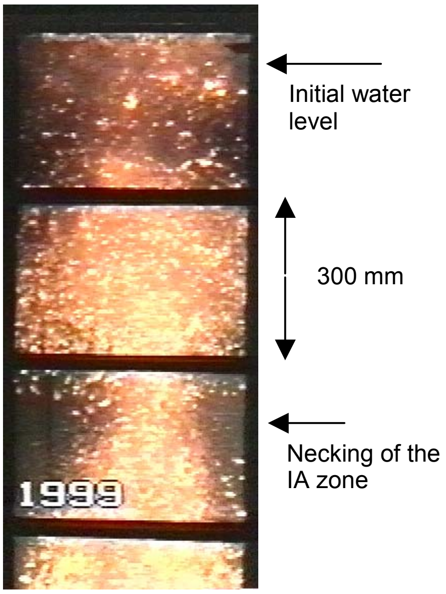

Fig. 33: Video frame taken at t = 1.9 s. The necking was at –700 mm height.

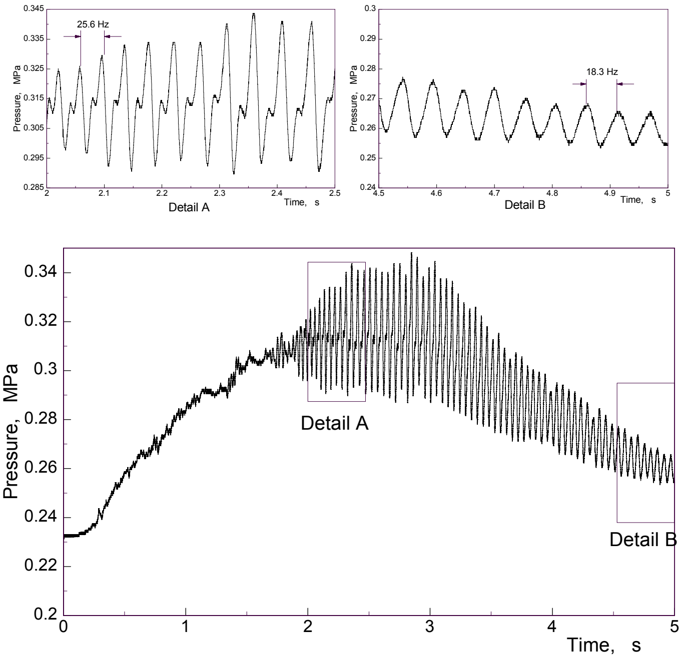

Fig. 34: Pressure history obtained at –1065 mm height. The upper graphs show periods at the beginning and end of the oscillations.

same time, clouds of shining melt fragments came into zones of continuous water surrounding the core of the interaction zone (Fig. 33). Presumably, the quantity of melt fragments, that was in continuous subcooled water, was in the state of subcooled boiling. This kind of boiling is characterized by frequent evaporation/condensation processes which produce pressure oscillations.

The frequency as well as the amplitudes of the oscillations decreased with time (Fig 34). The two small diagrams give full signals at a larger time scale at the very beginning (detail A) and at the end (detail B). (Note that the signal in the large diagram has been drawn using a reduced plotting rate.)

In PM17, such information could not be gained from the films since the view to the interaction zone through the bulk of water became increasingly opaque from 2.5 s on. Probably, a (still unknown) chemical reaction occurred during quenching. We also presume that the condition encountered in PM18 leading to subcooled boiling (i.e. melt fragments in continuous water) occurred in PM17 at a later time.

Development of the interaction zone; volumes and volume fractions

In this section, three tests, performed under different initial conditions of water subcooling, are compared to show its influence on the development of the interaction zone. The graphs in Fig. 35 give the growth of the mixing zones in the axial and radial directions with the time as a parameter. In PM17 and PM18, the construction of the lines has been made mainly on basis of films since, because of the narrow mixing channel, there were too few void data available for a reasonable construction. The upper ends of the lines mark the actual water level. The comparison shows that the larger the subcooling was, the smaller was the ratio of radial to axial expansion and the smaller was the rate of level rise during the initial time. The melt release times were between about 1.0 s in PM13 and 1.7 s in PM17.

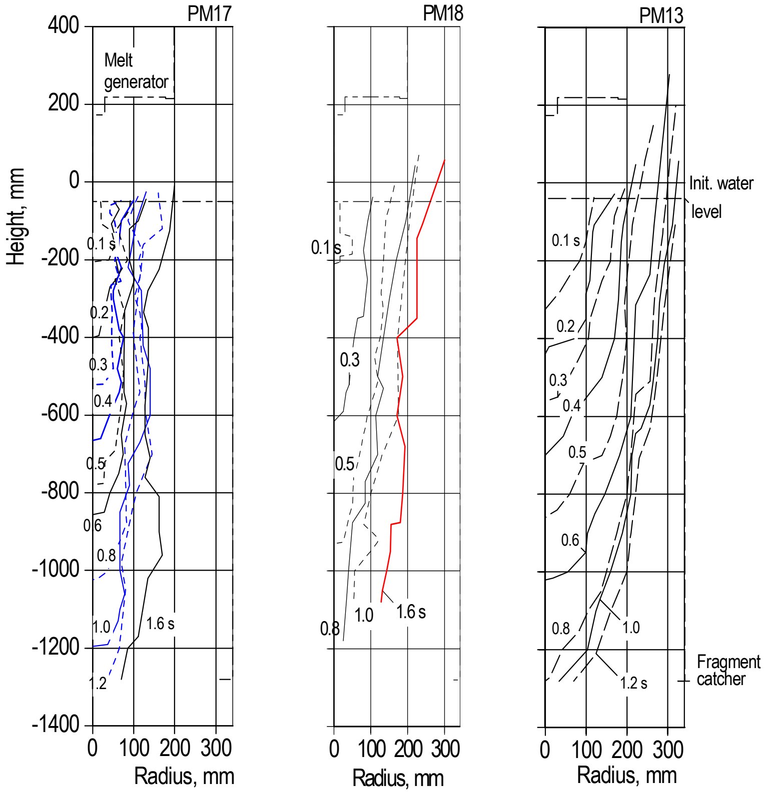

Fig. 35: Influence of water subcooling on the development of the interaction zone. Subcooling in PM17: 104 K, in PM18 = 26 K; PM13: saturated water.

The time functions of the volumes of the interaction zone and of the volumes due to level rise (Fig. 36) complement the information given in Fig. 35. Another very interesting piece of information is obtained from the time functions of the average volume fractions (lower diagrams in Fig. 36).

The most remarkable result is the large value of the liquid volume fraction (around 0.8) in case of large subcooling (PM17) which remained constant during the time considered. The result seems reasonable regarding the very small level rise in PM17. Thereby, the volume fraction of steam remained low.

In the cases of moderate water subcooling and saturated water, respectively, the volume fractions of liquid and steam came closer together after the very initial period of time: about 0.65:0.35 in PM18 and about 0.5:0.5 in PM13. The result leads to the conclusion that the average distance of the melt to water in the interaction zone and to the bulk water was the smaller the larger the water subcooling was.

It should be noted here that in PM18 the level time function used in the calculation was corrected towards larger values from about 0.35 s on. The reason for the correction were findings gained from thorough evaluation of film pictures as well as of void signals. The level marking at the glass window, which could well be followed in the films up to 0.4 s, moved out of the window after that time, while the development of an extended churned steam/water mixture could be observed through the window lying farther up. Moreover, the void probes located in the freeboard volume indicated the presence of water drops, while both the number of drops per unit of time and the axial height of detection increased. The mean of the level measurement and a time function describing the upper bound of droplets was considered as a best estimate for the upper boundary of the interaction zone to be used in the calculation (Fig. D12).

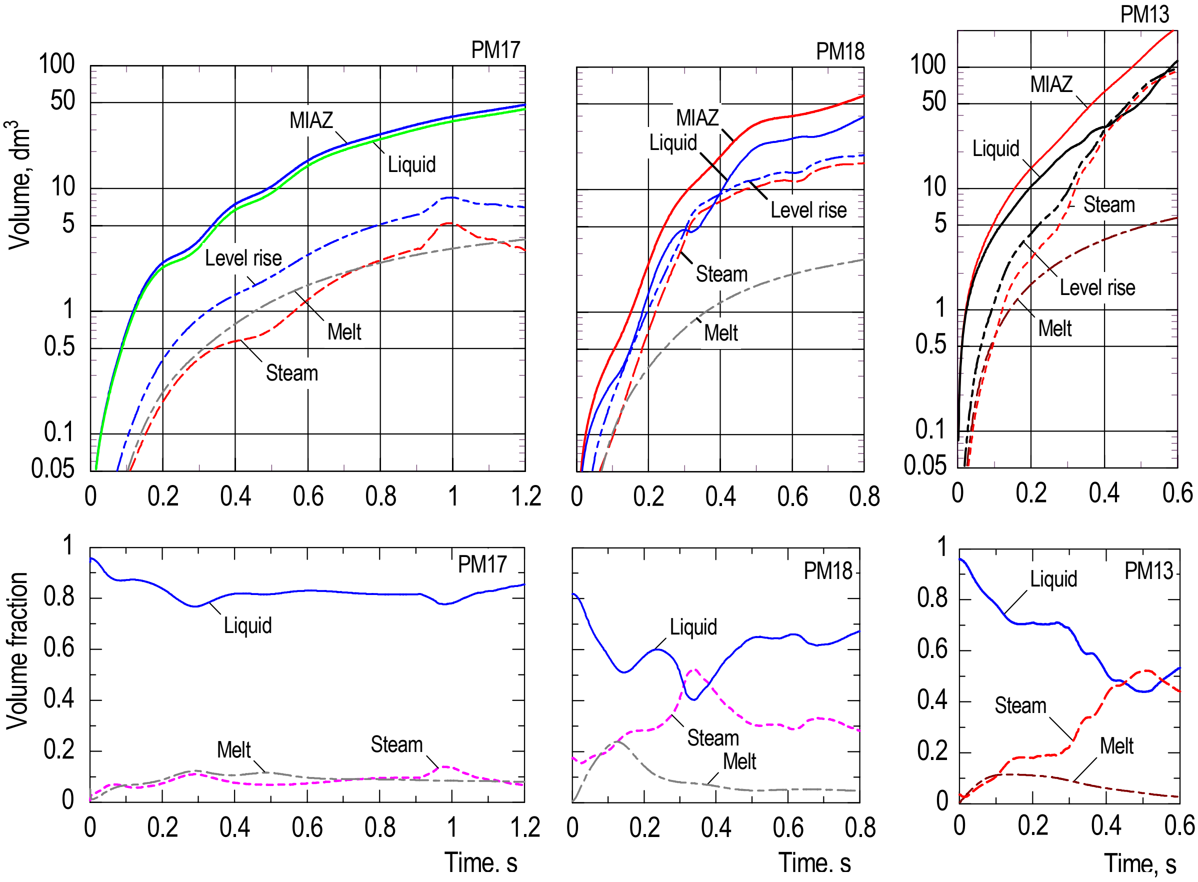

Fig. 36 Volumes and volume fractions under different subcooling conditions. The volume of the multiphase interaction zone (=MIAZ) was evaluated from the contour lines in Fig. 35.

From the whole information gained in PM18, we can state that the development of the interaction resembles more that of tests performed with initially saturated water conditions, e.g. PM13, than that of PM17 performed with large subcooling.

In this context, the actual water subcooling has to be taken into consideration which depends on the pressure time history. I.e., even if the water was saturated at the beginning, it became subcooled because of the pressure increase during interaction. Taking the maximum pressure rises in each test as a basis, the maxima of subcooling were 17 K in PM13, 26 K + 8 K = 34 K in PM18, and 104 K +15 K = 119 K in PM17. Under this aspect, the maximum subcooling in PM18 was only twice that of PM13. In PM17, subcooling was about one order of magnitude larger.

Jet break-up length

From the penetration rate (Fig. D13), a jet break-up length L ≈ 870 mm was derived. The thermocouple readings give L>665 mm (Fig. D10, T11 TC was damaged at 0.8 s).

Post test investigations

The masses of fragments collected at the various sites after the test were: 5.68 kg as a cake at the fragment catcher plus 5.48 kg of loose particles on top of the cake; 3.44 kg of loose particles at the bottom of the vessel.

The sieve analysis made separately for the two sites (Fig. 37) gives a predominance of medium sized particles (2.5 to 10 mm) in both sites. The fragment catcher dominates in the fraction of very fine particles. The particles were not as brittle as in PM17. Breaks to smaller pieces during sieving can not be excluded, however. The photograph given in Fig. 38 show spherical as well as broken particles. We do not know when the breaks occurred, during quenching or during the sieving process.

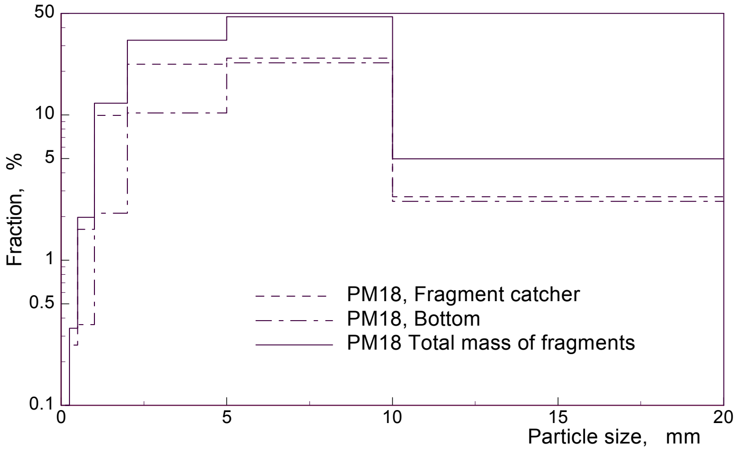

Fig. 37: Sieve analysis performed with loose particles only.

Fig. 38: Particles sampled at the fragment catcher, sieve fraction 5 – 10 mm.

The analysis of gas samples taken prior and during the experiment has resulted in no hydrogen or 0.2 to 0.3 % of hydrogen related to the non-condensable gas fraction. It is estimated from the pressure in the bottles after the test compared to the system pressure during the experiment, that about 50 % of the gas probe during sampling had consisted of steam. Thus, it is concluded that the amount of hydrogen generated during melt-water interaction is very small in this case.

An increase in the water level of 20 mm was stated after the test.

5.6. Summary of the jet break-up lengths

The jet break-up lengths and the L/d ratios found in the PM12 – PM18 tests have been summarized, together with other data, in Table V. For comparison, results from the literature have been entered in the last column that were obtained using a formula of Saito et al. /17/. This correlation reads as follows:

$$L/d = 2.1\,(u^2/g/d)^{0.5}\,(\rho_j/\rho_a)^{0.5},$$

where u and d are the speed and jet diameter, respectively, g is the acceleration due to gravity. The ρ_j/ρ_a ratio has a value of 2.8, where the suffices j and a refer to the jet and ambient fluids, respectively. The correlation was used by the authors to represent the data of their tests performed with Freon-11 and liquid nitrogen.

Table V: Jet break-up lengths, L, PM12 to PM18; d is the nozzle diameter.

Exp.	Melt mass [kg]	Nozzle diam. [mm]	Release time s	Melt speed [1] [m/s]	Length from speed – [mm]	TC damage [mm]	L/d in Fig. 39 Experim. – -	Saito
PM12	29.0	60	0.95	3.8 – 4.2	-[2]	895<L<1095	14.9 - 18.3	18.3
PM13	23.8	60	1.05	4.0 – 4.2	-[2]	1075<L<1175	17.9 – 19.6	18.8
PM14	23.2	60	0.95	4.5 – 4.7	-[2]	L>1175	>19.6	21.1
PM15	23.1	60	1.40	3.2 – 3.3	730	L>965	12.2[3]	14.9
PM16	60.4	48	5.0	1.9 – 2.5	790	665<L<865	16.5[3]	12.8
PM17	16.0	48	1.70	1.7 – 2.6	630	L>465	13.1[3]	13.3
PM18	14.6	48	1.50	1.9 – 2.9	≈870	L>665	18.1[3]	14.8

[1] on first melt/water contact – maximum, both values from calculation;
[2] no clear change in speed observed; [3] from speed

Figure 39 shows that, generally speaking, the penetration lengths observed in the experiment are consistent with each other and with Saito´s formula. We observe mostly somewhat larger values in the experiments. Beyond the effect of jet velocity, the influence of single parameters is obscured by the scattering of the data. There are two cases with a system pressure of 0.5 MPa (with the water still almost saturated): PM15 and PM16. They show opposite tendencies: PM15 is smaller and PM16 is larger than predicted by Saito. (We mention that the large penetration length observed in PM16 is not caused by the long melt delivery time because jet break-up is already detected after 0.4 s). There are also two cases with 0.22 MPa system pressure and large coolant subcooling. PM17 with 104 K subcooling agrees perfectly with Saito´s formula while PM18 with only about 30 K subcooling shows a much larger break-up length. So, no conclusion can be drawn concerning the influence of system pressure and coolant subcooling.

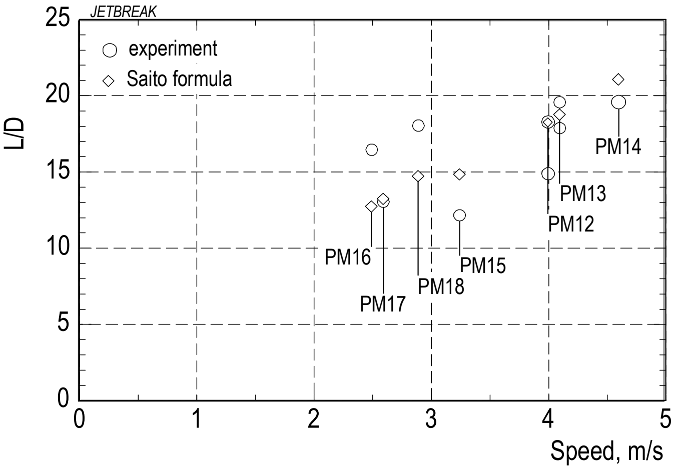

Fig. 39 Jet break-up length to diameter ratio vs. speed. The speeds are average values (PM12 – 15) and maximum values (PM16 – 18) from Table V.

6. RELATIONS BETWEEN PREMIX EXPERIMENTS AND FARO/KROTOS EXPERIMENTS

6.1. The EU-MFCI project

As already stated in Chapter 1, the PREMIX alumina tests may be related and compared to FARO corium tests on a similar scale and to KROTOS alumina tests on a smaller scale. FARO and KROTOS were experimental programmes at JRC Ispra. The comparison will provide material effects in the first case and scale effects in the second case.

All three programmes were parts of the MFCI project in the Fourth Framework Programme of the EU on fission reactor safety, beginning in Jan. 1997 and ending in June 1999. This project investigated melt stream fragmentation and mixing in water, focusing on the role of melt physical properties and water subcooling, in view of characterising the main processes which govern quenching of molten corium in water during core melt down accident and relocation in lower head and cavity. A summary report is given in ref. /12/.

6.2. PREMIX - FARO

Close similarity between PM16/PM17 PREMIX tests and L-28/L-31 FARO tests, projected with respect to initial parameters and boundary conditions, was a special feature of the MFCI project.

In the FARO tests within the project, the melt quantities were up to 175 kg at 3100 K. The melt, a mixture of 80 wt% UO_2 and 20 wt% ZrO_2, was generated in a furnace by direct heating, then delivered to a release vessel and, after isolating the furnace, released into the water pool by gravity. The pool had a diameter of 0.71 m and the water depth was typically 1.5 m. In addition to the jet break-up and mixing aspects, the tests provided global data on quenching and debris bed characteristics. The tests were performed in the FAT vessel provided with view ports for visualisations, which allowed to characterise the melt entry conditions. One test was performed with saturated water (in-vessel typical, L-28), the other with subcooled water (ex-vessel typical, L-31). No spontaneous steam explosion occurred.

The conditions of L-28 were a jet diameter of 5 cm, a melt mass of 175 kg and a system pressure of 0.5 MPa. The test demonstrated an important feature never yet obtained experimentally, i.e., that the quenching rate rapidly stabilised at a constant value ($\approx$ 30 MW) for all the duration of the jet flow.

Subcooled water test L-31 was performed at 0.22 MPa and a reduced quantity of melt (92 kg) for safety reasons. No fundamental differences in quenching were observed with respect to other tests with saturated water. The particle size of the debris was of the same order as that of the particulate debris found in saturated water test. However, no cake was present.

PM16 was similar to L-28, PM17 to L-31. The most important features and parameters of these tests are listed in Table VI. Concerning the melt, it has to be noted that the heat per volume of alumina is nearly the same as that of corium. So, one third of the melt mass in L-28 has been used (as alumina) in PM16. In PM17, compared to L-31, this ratio has even been reduced, mainly for safety reasons with view to the likelihood of a spontaneous explosion. To simulate a gravity-driven melt release in the PM16 / PM17 tests, a pressure regulating system was used as outlined in Chapter 3. So, the long release time (5 s) in L-28 was reproduced in PM16, although some fluctuations in the driving pressure occurred due to delay time effects inherent in the regulating system.

Pool geometries and water temperatures were quite similar. However, strong differences existed with respect to gas (expansion) volumes and steam release modes. In L-28 and L-31, the volume was approx. 3.5 m^3. In PM16, the test vessel was open via four steam venting tubes to the 220 m^3 FAUNA vessel. In PM17, these tubes were closed at their outlets, which meant a strong reduction of the gas volume to 0.9 m^3. These differences are the main reason why a simple and direct comparison of the test results is not possible. It will be necessary to use the results of both types of tests as an input to computer codes.

Typical pressure readings are given in Fig. 40. Obvious differences are the rate of increase and the maximum of the pressure, respectively. The major reason for this was, of course, the larger volume for steam expansion in PM16. On the other hand, similar behaviour was found in that the pressure increased in both tests as long as melt was delivered. This means that there was no ‘upper limit’ under the conditions of

Table VI: Most important features of the PREMIX and FARO experiments in question.

		PM16	L-28	PM17	L-31
Melt					
Material		≈ 90% Al_2O_3 10% iron	80% UO_2 20% ZrO_2	≈ 90% Al_2O_3 10% iron	80% UO_2 20% ZrO_2
Mass	kg	60.4	174.9	16.0	92
Temperature	K	2600	3052	2600	2990
Volume	m^3	$21 \cdot 10^{-3}$	$\approx 19 \cdot 10^{-3}$	$5.7 \cdot 10^{-3}$	$\approx 10.2 \cdot 10^{-3}$
Total heat	MJ	258	247	68.4	≈ 125
Heat per volume	MJ/m^3	$12.3 \cdot 10^3$	$\approx 13 \cdot 10^3$	$11.9 \cdot 10^3$	$\approx 12.2 \cdot 10^3$
Speed	m/s	2.4	2.34	2.6	≈ 2.2
Orifice	mm	48	50	48	50
Release time	s	5.0	5.25	1.75	2.52
Water					
Mass	kg	512*	517	512*	480
Temperature	K	419	424	293	291
Subcooling	K	5	0	104	106
Diam. of vessel	mm	692	710	692	710
Depth	mm	1330	1440	1330	1450
Gas / Steam					
Initial pressure	MPa	0.5	0.5	0.22	0.22
Volume	m^3	220^+	3.5	0.9	3.5

*Above the fragment catcher

$^+$Volume of safety container; steam expanded via venting lines into this volume

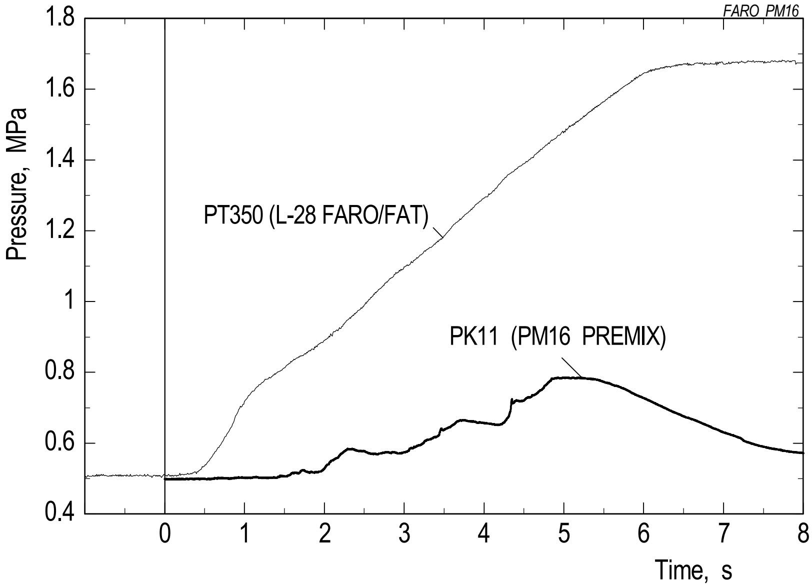

Fig. 40: Comparison of pressure readings typical of L-28 FARO/FAT and PM16 PREMIX experiments.

these tests. The quenching rate approached 10 MW in PM16 in comparison with 30 MW in L-28. The difference may be due to the different melt temperatures (3052 K vs. 2600 K) and – to some extent – to the different actual pressures.

The pressure rise in L-31 was small, similar to PM17. A significant amount of hydrogen was found during L-31, whereas practically no hydrogen was found in PM17. The pressure rise in L-31 is mainly attributed to hydrogen generation during corium-water interaction, whereas it was due to steam production in PM17. So, hydrogen generation is regarded one of the important differences between corium-water and alumina-water interaction, respectively.

6.3. PREMIX - KROTOS

Within the MFCI project, four KROTOS tests with corium melt were performed. In addition to that, in an earlier test series /13/, alumina melt has been used as well. The KROTOS test facility consisted of a radiation furnace, a release tube and the test section. The test material was melted in a crucible held in place in the furnace by means of a pneumatically operated release hook. The crucible was then dropped onto a puncher which broke its bottom. By this, melt was released to the water. Depending on crucible design and melt composition, melt masses in the range of about 1 to 6 kg could be produced. The maximum achievable temperature was 3300 K. The pressure vessel was designed for 4.0 MPa at 493 K. It housed the test section, which consisted of a thick stainless steel tube whose inner diameter was 200 mm. The outer diameter was 240 mm. The water level was variable; water depths of up to about 1.3 m could be set. The bottom of the test section consisted of a plate which housed a trigger device (gas or explosive charge).

A number of alumina tests were performed under both subcooled and saturated water conditions. The tests with subcooled water normally resulted in spontaneous steam explosions. The tests under almost saturation conditions were performed to confirm, on the one hand side, common experience, namely suppression of spontaneous steam explosions under such conditions and, on the other, to show that a steam explosion can yet be triggered by using an external initiator. Other test parameters in the KROTOS alumina tests were melt superheat and the initial pressure.

All tests in the melt superheat range investigated (150 K – 750 K) ended with a steam explosion. No evidence was obtained of explosion suppression in the alumina tests by elevated initial pressures (set in a small range of 0.1 – 0.375 MPa). In most cases, the conversion ratio, i.e. the energy released divided by the initial thermal energy, was about 2.5 percent.

On the other hand, none of the tests with corium produced an energetic steam explosion. However, propagating low energy events with a maximum energy conversion ratio of about 0.15 % were observed when an external pressure trigger was applied.

Comparing PREMIX and KROTOS tests, e.g. PM17 to K-43, values for melt temperature, pool temperature and height, and initial vessel pressure were found very close to each other.

Inherent differences existed in the melt mass (one order of magnitude), pool diameter, and water mass (one order of magnitude). A selection of parameters is listed in Tab. VII (the KROTOS data are from ref. /13/).

Table VII: Comparison of most important features of a PREMIX and a KROTOS experiment both performed with alumina.

		PM17	K-43
Melt			
mass	kg	16	1.5
temp.	K	2600	2625
superheat	K	286	311
orifice	mm	48	30
Water			
mass	kg	512	34.6
temp.	K	293	295
subcooling	K	104	100
depth	mm	1330	200
diam. vessel	mm	692	1100
Gas			
pressure	MPa	0.22	0.21
Explosion		no	yes

The most striking difference between KROTOS and PREMIX tests, as far as being performed with subcooled water, is that no spontaneous explosion occurred in PREMIX, neither in PM17 nor in PM18. In this report, we can not give an explanation for the different behaviour.

7. CONCLUSIONS

The PREMIX tests were performed to improve the understanding of the premixing phase during thermal interaction of a hot melt and water. Different parameters influencing the course of the mixing were varied in eighteen experiments: melt mass, degree of subcooling, system pressure, duration of melt release, and condition of steam release. The results of the last seven tests of this series (PM12 to PM18) are described herein. In two of these tests, conditions were established similar to FARO/FAT experiments with corium, to allow for a comparison and to evaluate the influence of different melt materials on the mixing and quenching processes.

By video and high speed filming in combination with measurements of pressures, water level, temperatures, steam flow and void conditions, a large data base was generated to describe the development of the interaction and of related phenomena. This information is essential for the validation of computer codes such as MC3D, MATTINA, IKEJET, COMETA and IVA. These codes are needed to calculate for the course of severe reactor accidents and for the consequences arising.

With tests PM12, PM13, and PM14, a standard set of data has been generated for code validation. It has also been shown that the results are well reproduced, typically within 15 %. Deviations in the results could be attributed to inevitable differences in the starting conditions, especially to the driving pressure for melt release.

By the PM15 test, it was shown that a larger system pressure at otherwise same conditions leads to a less violent interaction and a narrower reaction zone. The steam mass flow is similar to PM14 (the test which fits best with respect to the starting conditions), but the steam volume flow and the pressure rise are significantly smaller. The debris particle size is shifted to somewhat larger fragments.

In test PM16 with larger melt mass and longer release, but similar rating at the beginning, as in PM15, steam production and pressure rise were larger than expected. Long-term melt release obviously has a strong effect on steam production. After the test, about half the melt was found as particles, the other as a cake.

During test PM17 with strong subcooling (104 K), the venting pipes were closed Only little steam was produced. A narrow interaction channel with escaping steam was formed by the penetrating melt, causing a pressure rise of 0.06 MPa. The course of PM18 with less subcooling (30 K) was not much different from PM17. Escaping steam caused a pressure rise of 0.09 MPa.

The break-up lengths of the alumina jets were derived from the melt penetration history and/or thermocouple data. Comparing them with Saito’s formula /17/ shows relatively good agreement. Especially tests PM12 to PM15 show the expected influence of the melt velocity. On the other hand, the experiments give no clear indication of the influence of system pressure and coolant subcooling on the break-up length.

No energetic event (steam explosion) occurred in the PM12 to PM18 tests performed within the project. Hydrogen generation was found to be of minor importance and never had an influence on pressure build-up.

To compare results of PREMIX and FARO/FAT tests and to localise differences that result from different melt properties, calculations are needed using the codes listed above. Calculations are also needed because of the different venting and expansion conditions. For example, pressure rise in PM16 versus FARO L-28 is 0.3 MPa versus 1.5 MPa, since PREMIX had a much bigger expansion volume. In PM17 with closed venting lines, a rather similar behaviour to FARO L-31 was observed, namely rise from 2.2 to 2.6 MPa. On the other hand, the contribution of hydrogen to the pressure rise has to be determined carefully, since unlike PREMIX a significant amount of hydrogen was found in FARO/FAT.

The consequences of a steam explosion are not only defined by the amounts of melt and water in the interaction zone, but also by the conversion coefficient for the transfer of thermal to mechanical energy. A new test series (ECO) has been established at FZK in April 2000, in which the conversion ratio during a steam explosion is measured in well-controlled and confined conditions similar to PREMIX, but with an artificial trigger. In the ECO tests, the same technique to provide a melt/water mixture as in PREMIX is applied. Thus the experience gained so far is being used for evaluating the mentioned results. Knowledge from PREMIX is essential since filming the start condition of the explosion is not possible and the instrumentation is less extended.

8. REFERENCES

/1/ Corradini, M. L.,
Vapor explosions: A review of experiments for accident analysis, Nuclear Safety **32** (1991) 337-62

/2/ Will, H., Kaiser, A., Steinbrück, M.
Experimental investigation on a possible inherent limitation of masses involved in an in-vessel steam explosion, Jahrestagung Kerntechnik 1996, Proc. pp 230-235

/3/ Huber, F., Kaiser, A., Steinbrück, M., Will, H.
PREMIX, Documentation of the results of experiments PM01 to PM06, FZK-Bericht 5756, March 1996

/4/ Kaiser, A., Schütz, W., Will, H.
Melt water interaction tests, OECD/CSNI Specialists Meeting on Fuel-Coolant Interactions, May 19–21,1997,Tokai-Mura, Japan, Proc. Vol. 2 pp. 646 - 657

/5/ Kaiser, A., Schütz, W., Will, H.
PREMIX PM11, an experiment on melt-water interaction with steam explosion, Jahrestagung Kerntechnik 1997, Proc. pp. 244-250

/6/ Huber, F., Kaiser, A., Schütz, W., Will, H.
PREMIX, an experimental approach to investigate the mixing of a hot Melt being poured into water, Second Int. Conf. On Advanced Reactor Safety, ARS´97, Orlando, USA, June 1-4, 1997

/7/ Will, H., Kaiser, A., Schütz, W.
Influence of the system pressure on the mixing of a hot melt released into water Jahrestagung Kerntechnik 1999, Proc. pp 275, May 1999

/8/ Kaiser, A., Schütz, W., Will, H.
PREMIX Tests PM12, PM13 and PM14, documentation and evaluation of experimental data, FZK-Bericht 6370, INV-MFCI (99) D050[1], Sept. 1999

/9/ Meyer, L., Schumacher, G., Jacobs, H., Thurnay, K.
Investigation of the premixing phase of a steam explosion with hot spheres, Nuclear Technology **123** (1998) 142-55

/10/ Magallon, D., Annunziato, A., Will, H., Lummer, M., Vaeth, L., Turland, B.D., Dobson, G.P., Horvath, G.L., Valette, M., Valisi, M.,
High temperature melt/water mixing: Results and calculations of FARO, PREMIX, and MIXA experiments,
Van Goethem, G. [Hrsg.], FISA-95 Symp. EU Research on Severe Accidents, Luxembourg, L, November 20- 22, 1995, EUR-16896 EN (1996), S. 140-64

/11/ Alemberti, A., Berthoud, G., Buerger, M., Colombo, G., Kolev, N., Magallon, D., Sehgal, R., Schütz, W., Turland, B., Zero, S.,
Characterisation of processes which govern quenching of molten corium in water including steam explosion,
Van Gothem, G. [Hrsg.], FISA –97 EU Research on Severe Accidents: Mid-Term Review Symp. on Shared-Cost and Concerted Actions in Reactor Safety, Luxembourg, L, November 17-19, 1997,
European Communities, EUR-18258-EN (1998), S. 93-102

/12/ Magallon, D., Huhtiniemi, I., Dietrich, P., Berthoud, G., Valette, M., Schütz, W., Jacobs, H., Kolev, N., Grazios, G., Sehgal, R., Bürger, M., Buck, M., Berg, E. V., Colombo, G., Turland, B., Dobson, G., Monhard, D.
Molten fuel coolant interaction (MFCI), Van Goethem, G.[Hrsg.),
FISA-99: EU Research in Reactor Safety, Conclusion Symp. on shared-Cost and Concerted Actions, Luxembourg, L, November 29 - December 1, 1999, Luxembourg: Office for Official Publ. of the European Communities, EUR-19532-EN (2000), S. 211-19

/13/ Magallon, D., Huhtiniemi, I., Hohmann, H.
Lessons learnt from FARO/THERMOS corium melt quenching experimentsm,
Nucl. Eng. Des. **189** (1999) 223 - 238

/14/ Huhtiniemi, I., Magallon, D., Hohmann, H.
Results of recent KROTOS FCI tests: Alumina versus corium Melts
Nucl. Eng. Des. **189** (1999) 379 - 389

/15/ Magallon, D., Huhtiniemi, I., Dietrich, P., Berthoud, G., Valette, M., Schütz, W., Jacobs, H., Kolev, N., Grazios, G., Sehgal, R., Bürger, M., Buck, M., Berg, E. V., Colombo, G., Turland, B., Dobson, G., Monhard, D.
Characterisation of Molten Fuel Coolant Interaction Processes (MFCI),
Final Report, EUR-19567-EN (2000), INV-MFCI (99)-P007

/16/ Nazare, S., Ondracek, G., Schulz, B., Properties of Light Water Reactor Core Melts, Nuclear Technology **32** (1977) 239-246.

/17/ Saito, M., Sato, K. and Imahori, S., “Experimental study on penetration behaviours of water jet into Freon-11 and liquid nitrogen”, ANS Proc. of 1988 Natl. Heat Transfer Conf., Houston, TX, July 24-27, 1988

ACKNOWLEDGEMENT

The authors thank all colleagues from IRS who helped performing the experiments and evaluating the data. We also thank Dr. H. Jacobs (IKET) for valuable discussions, and Dr. C. Adelhelm (IMF) for chemical analysis.

The PREMIX tests were funded in part by the European Community (under contract FI4S-CT96-0037), SIEMENS and a consortium of German electricity utilities.

Appendix A: Test PM15

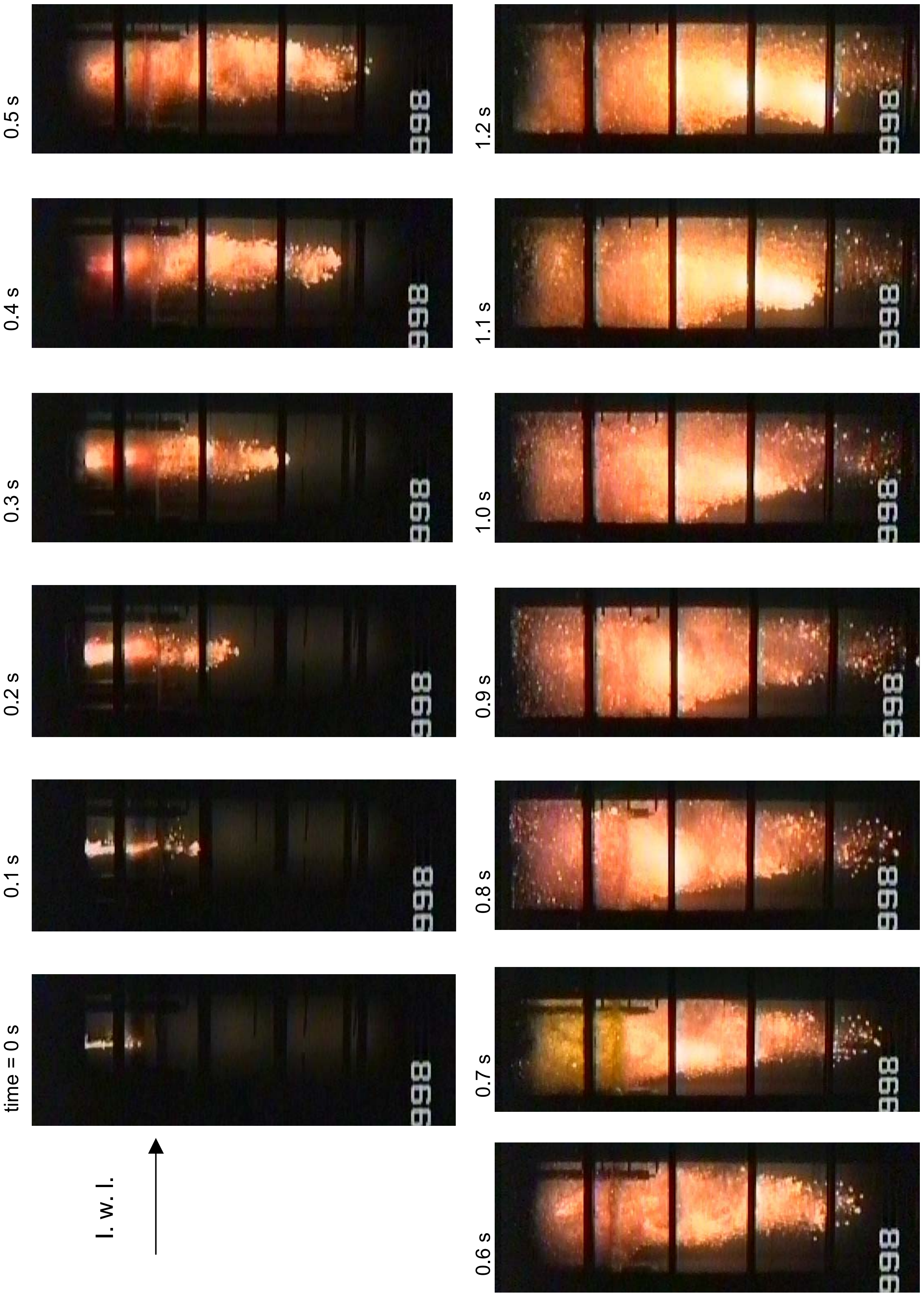

Fig. A1: PM15. Melt progression shown by a sequence of video frames. I.w.l. = initial water level.

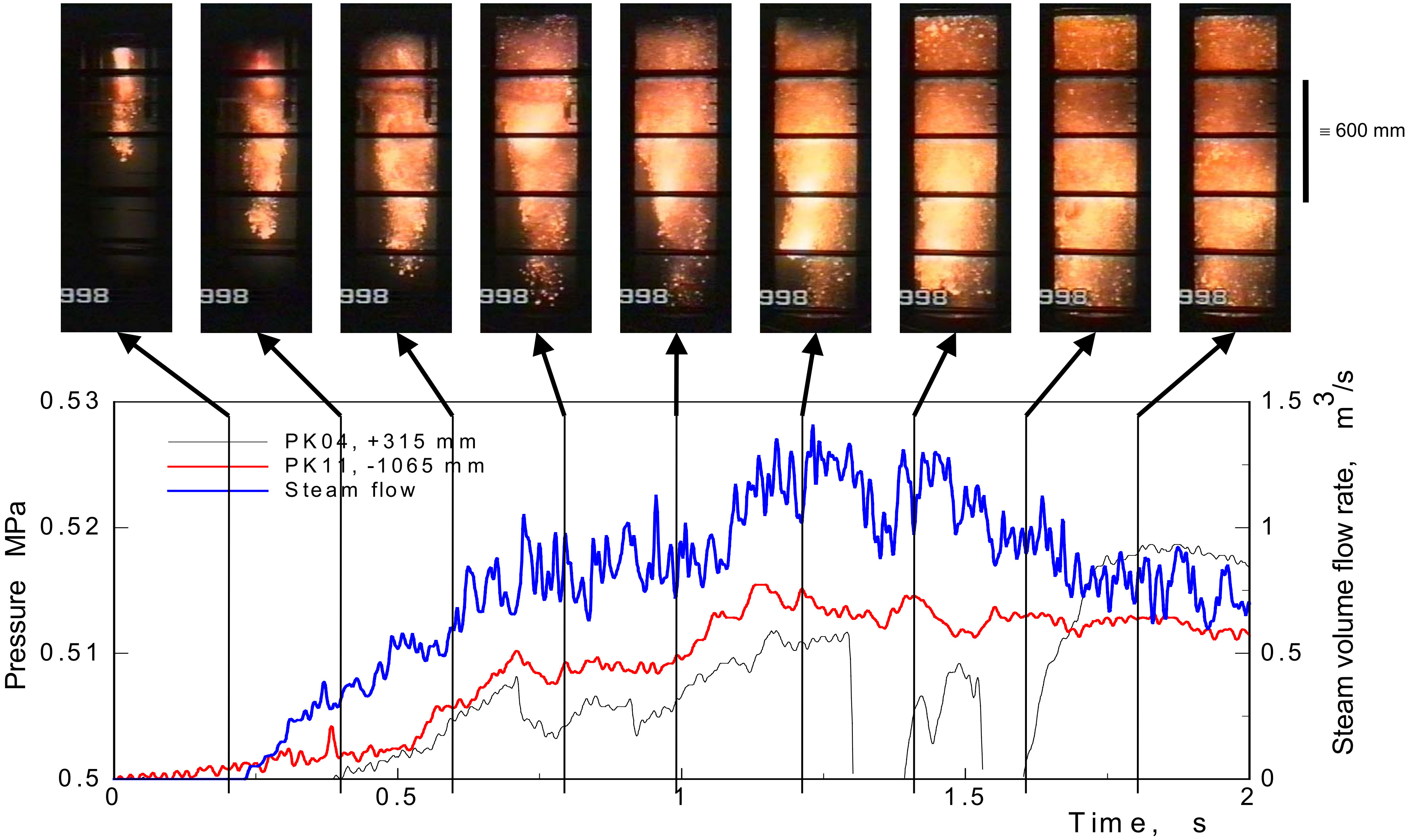

Fig. A2: PM15. Video frames showing distinct stages during melt penetration also visibly in the various signal traces of pressures in the water and in the gas space and of the steam flow rate.

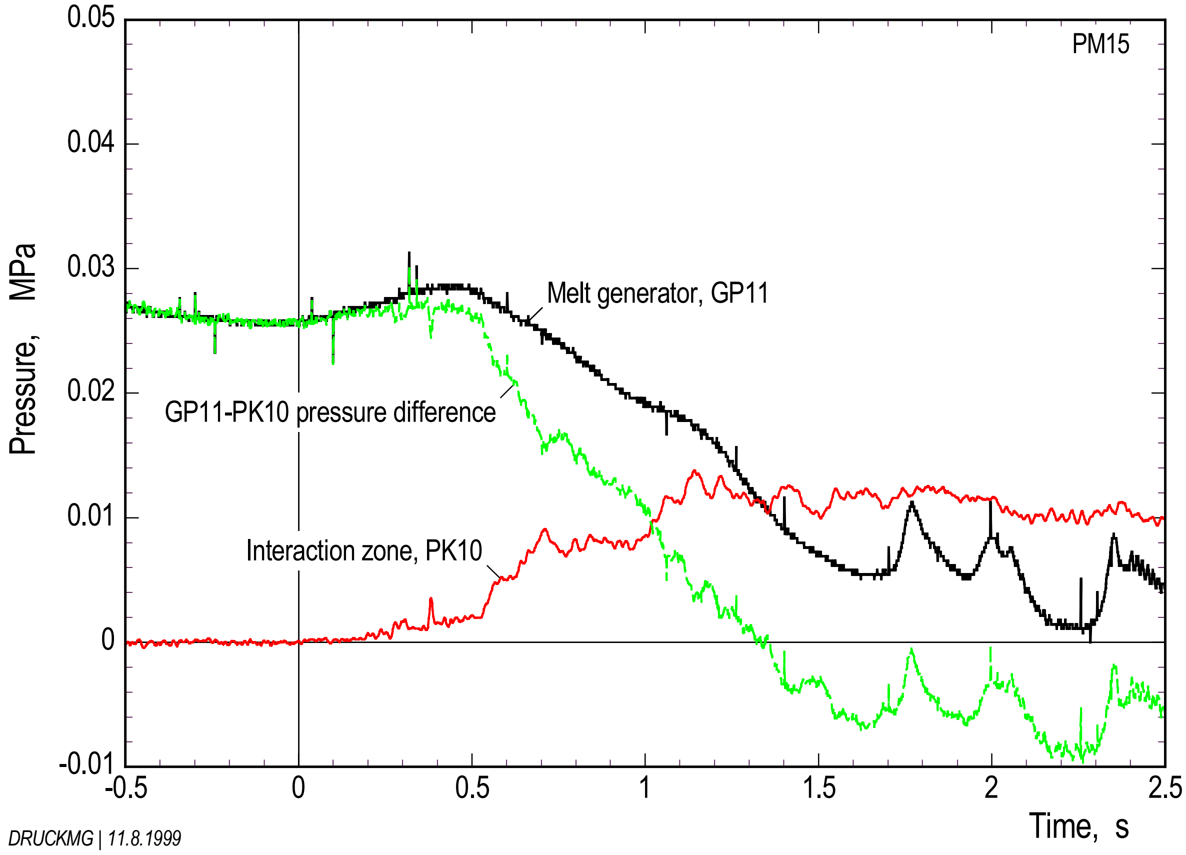

Fig. A3: PM15. Pressures determining the melt release

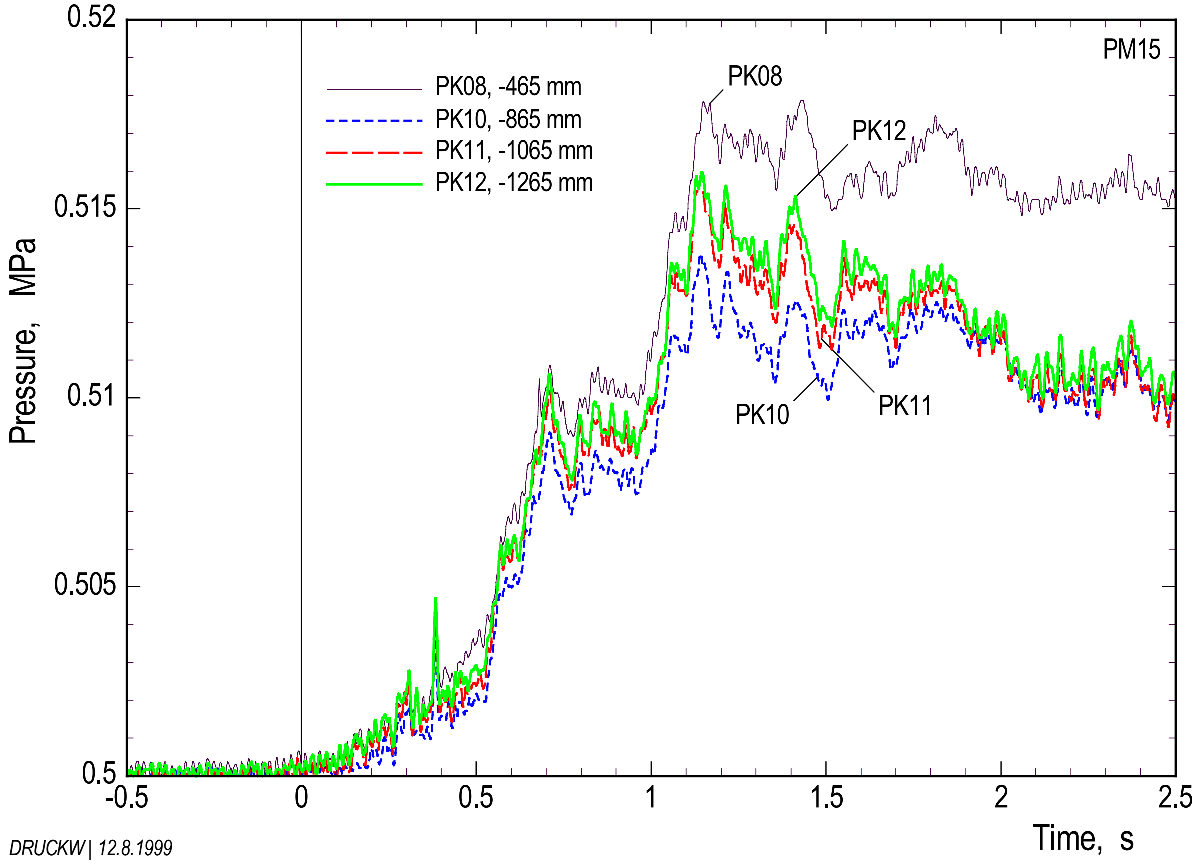

Fig. A4: PM15. Pressures measured in the water.

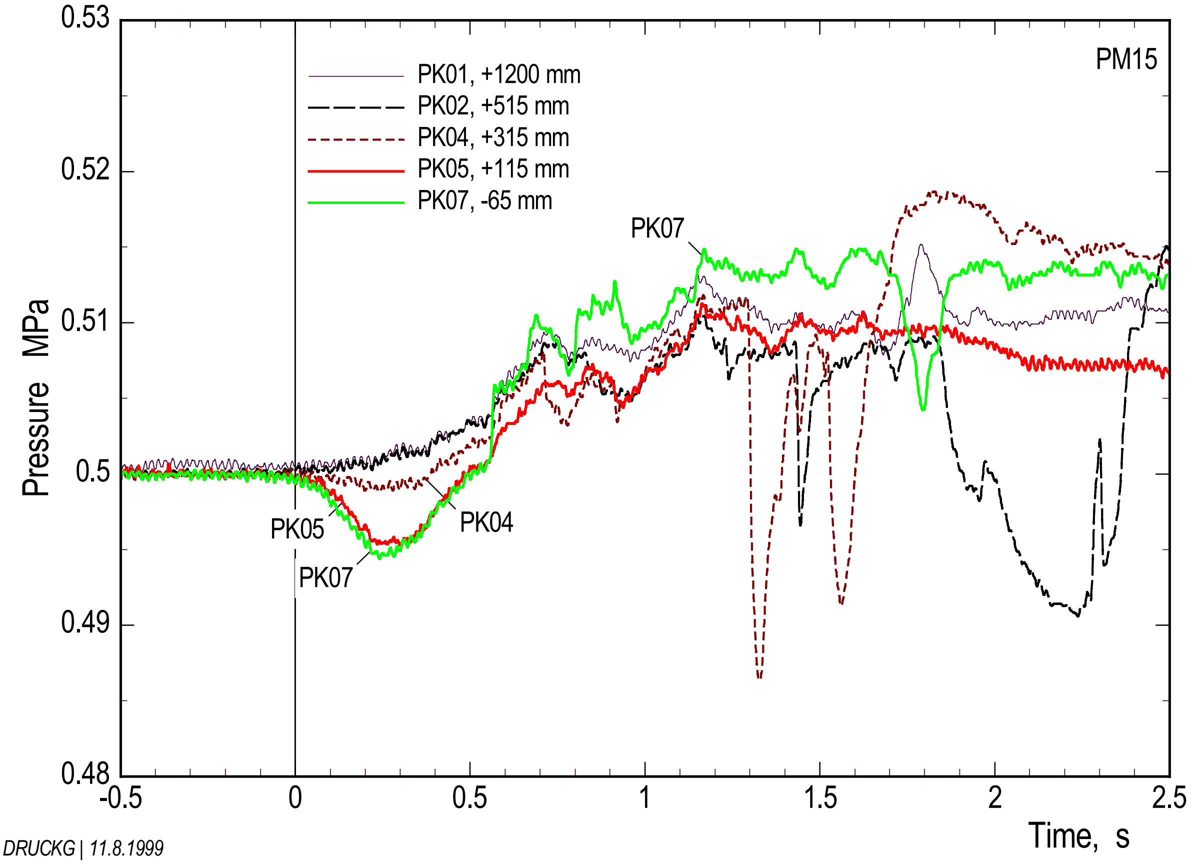

Fig. A5: PM15. Pressures measured in the gas space.

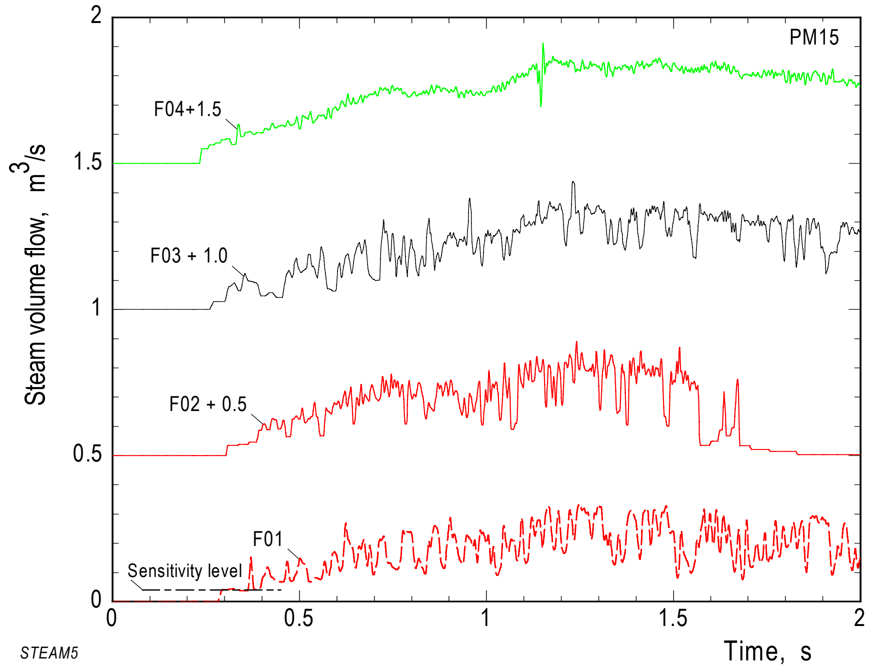

Fig. A6: PM15. Steam flow measurements

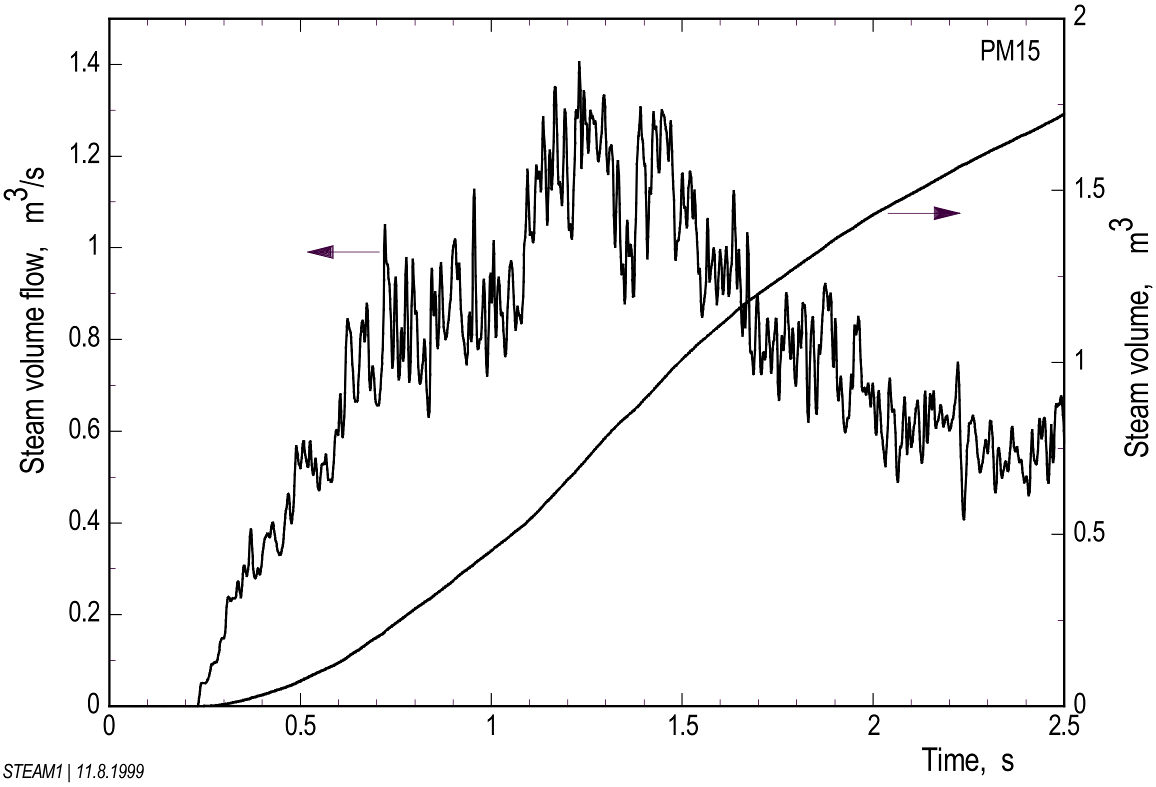

Fig. A7: PM15. Total steam flow rate and time integrated flow rate.

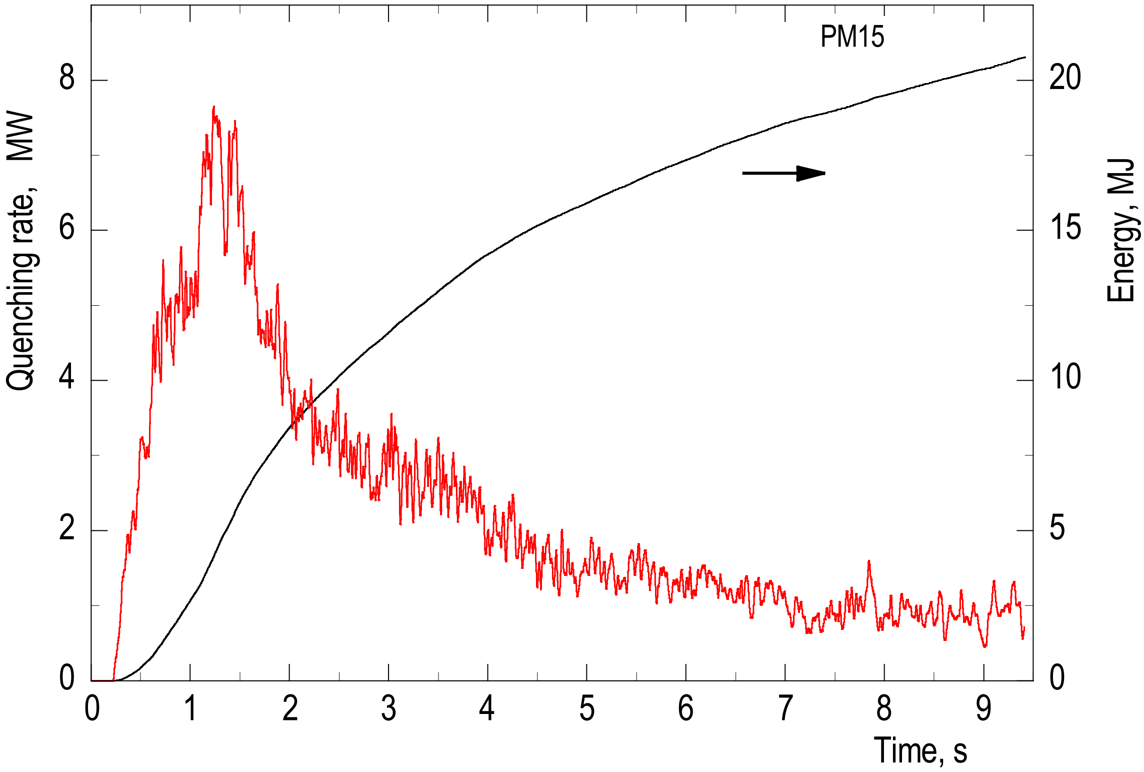

Fig. A8: PM15. Quenching rate and energy transferred.

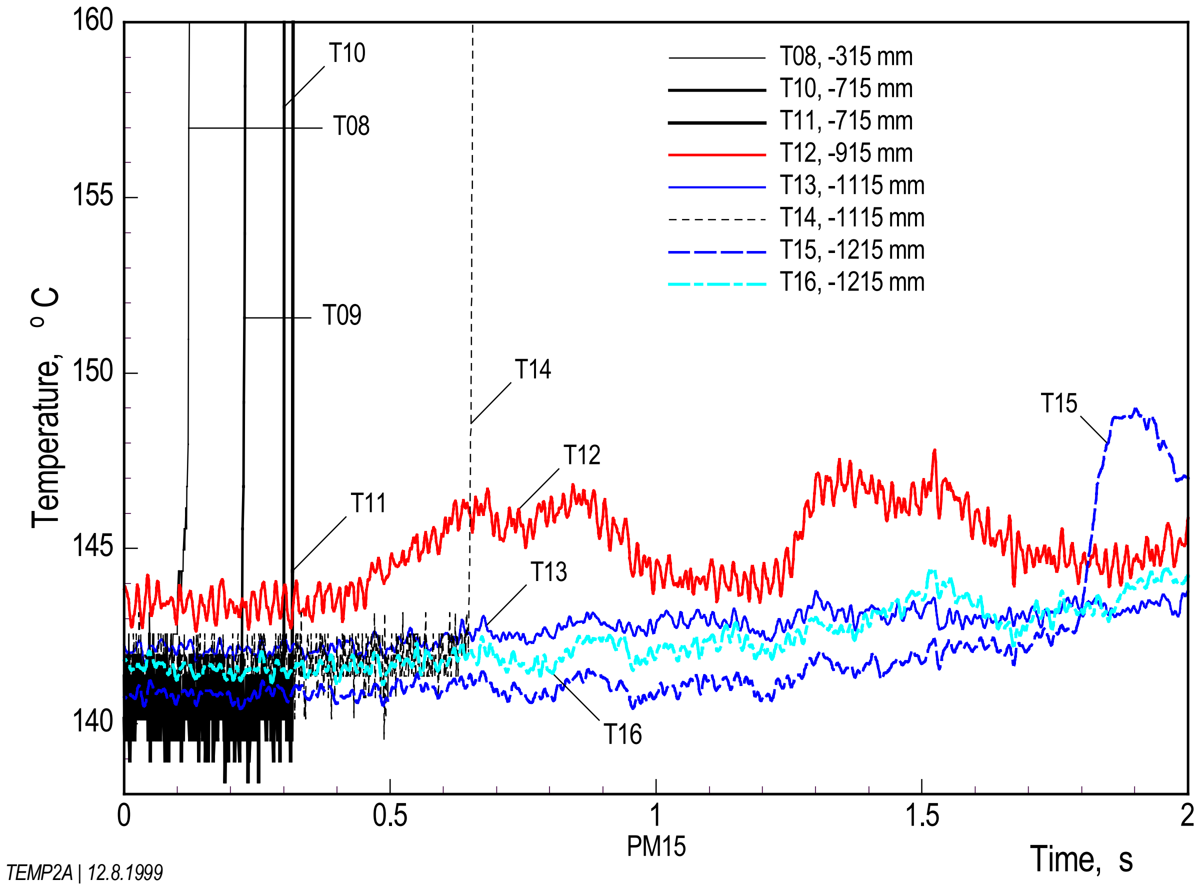

Fig. A9: PM15. Temperatures in the water at radius 25 mm.

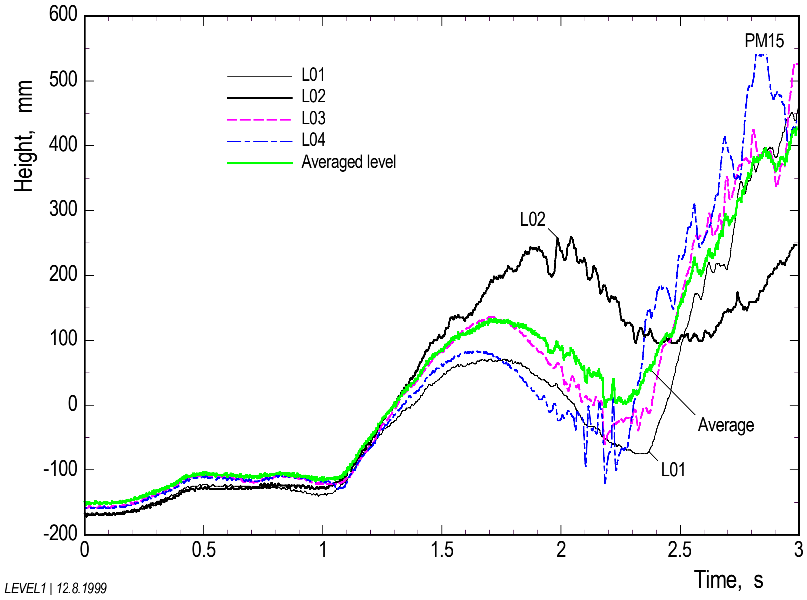

Fig. A10: PM15. Level measurements

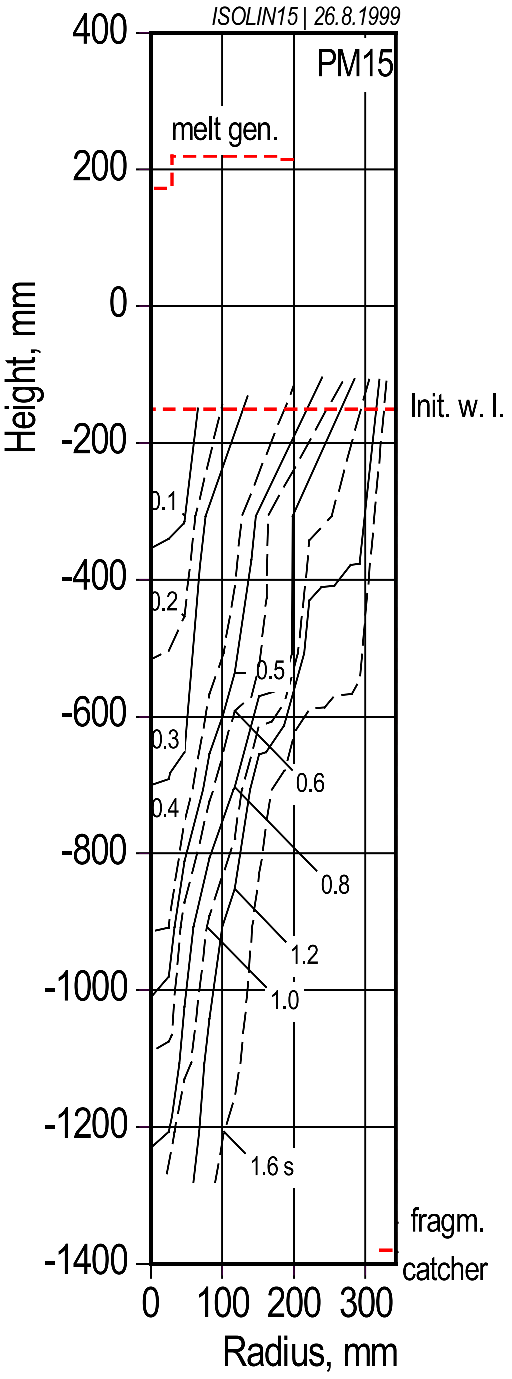

Fig. A11: Progression of the interaction zone into the water with the time as a parameter.

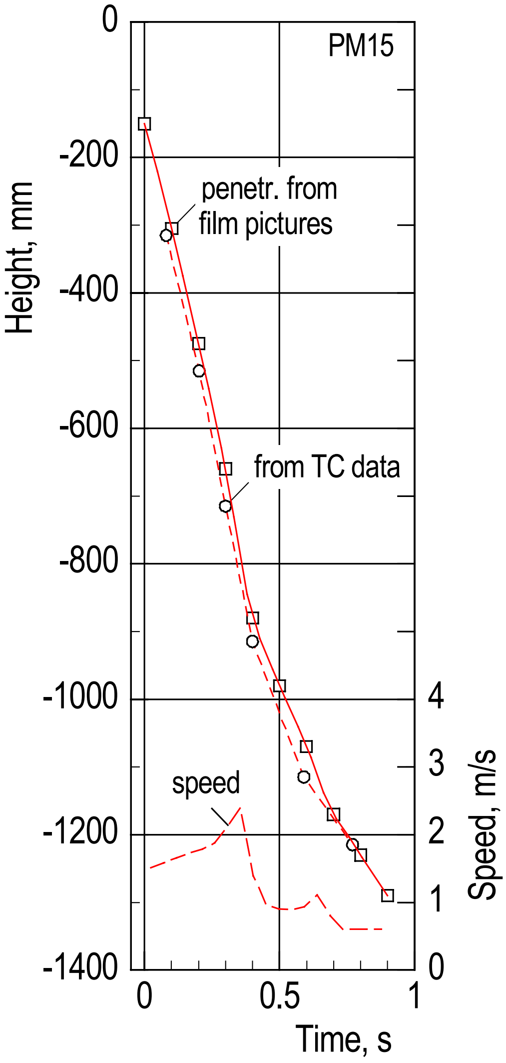

Fig. A12: Progression of the interaction zone in the centre of the pool. The speed is derived from the film data.

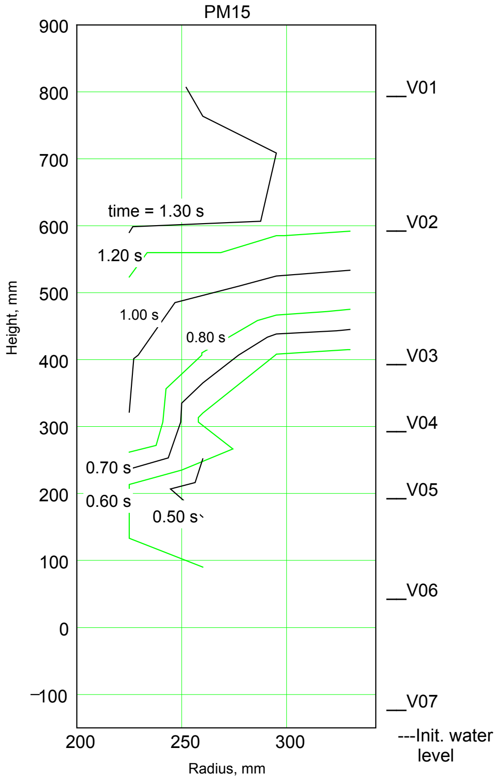

Fig. A13: PM15. Progression of the water drop front into the annular gas space, shown with the time as a parameter.

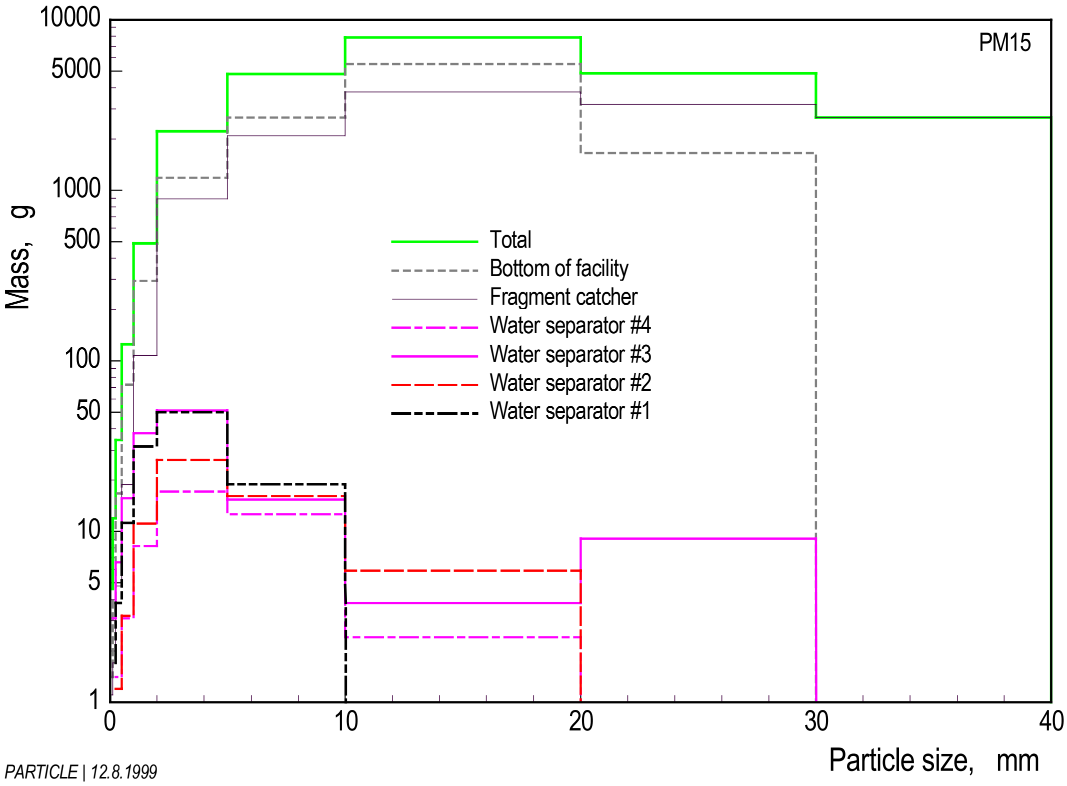

Fig. A14: Post-test particle size distribution.

Fig. A15: PM15. Local distribution of steam and water obtained from void probes at selected times. Dark points on base line=water; bright elevated points=steam.

APPENDIX B: Test PM16

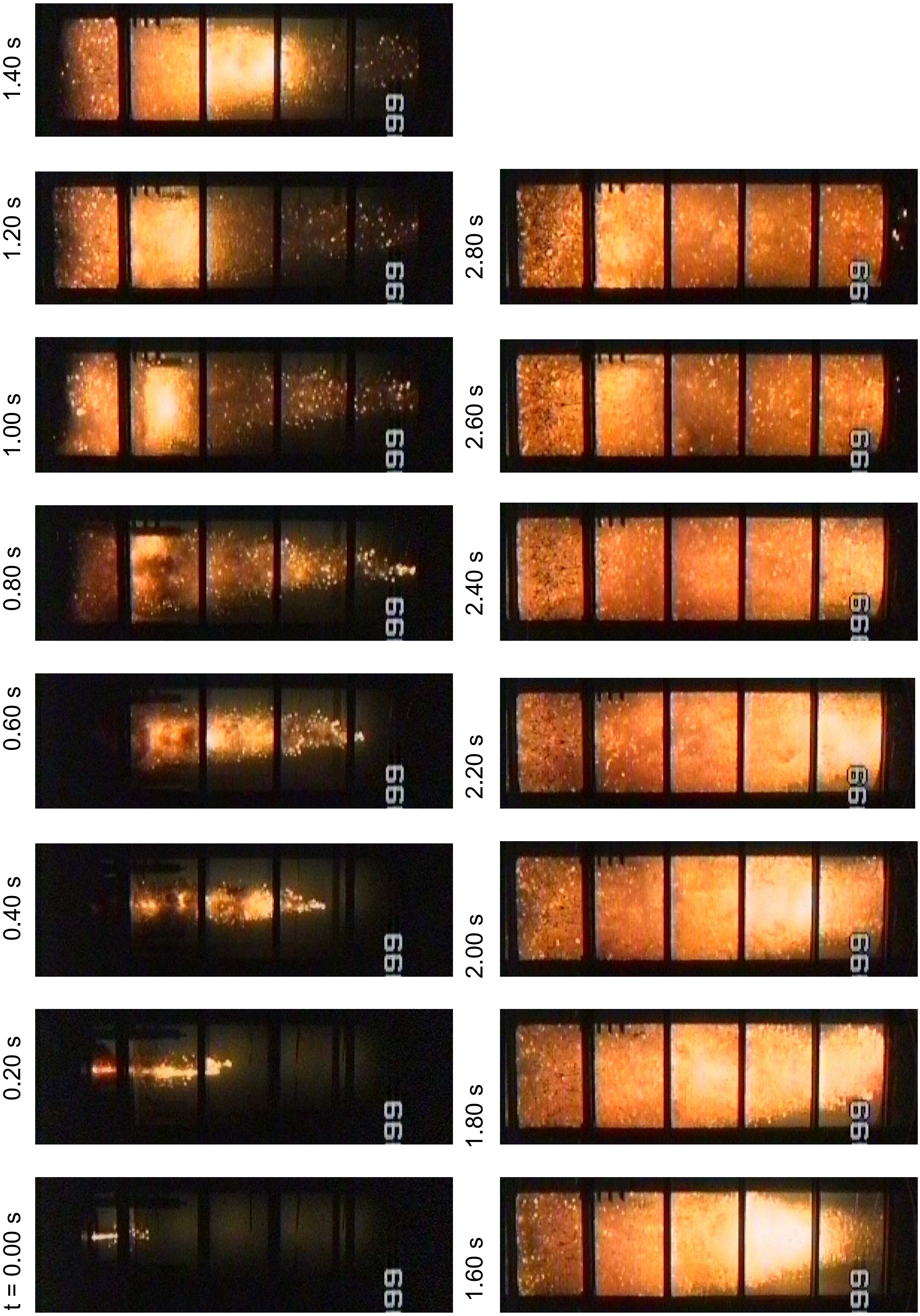

Fig. B1: PM16. Melt progression shown by a sequence of video frames.

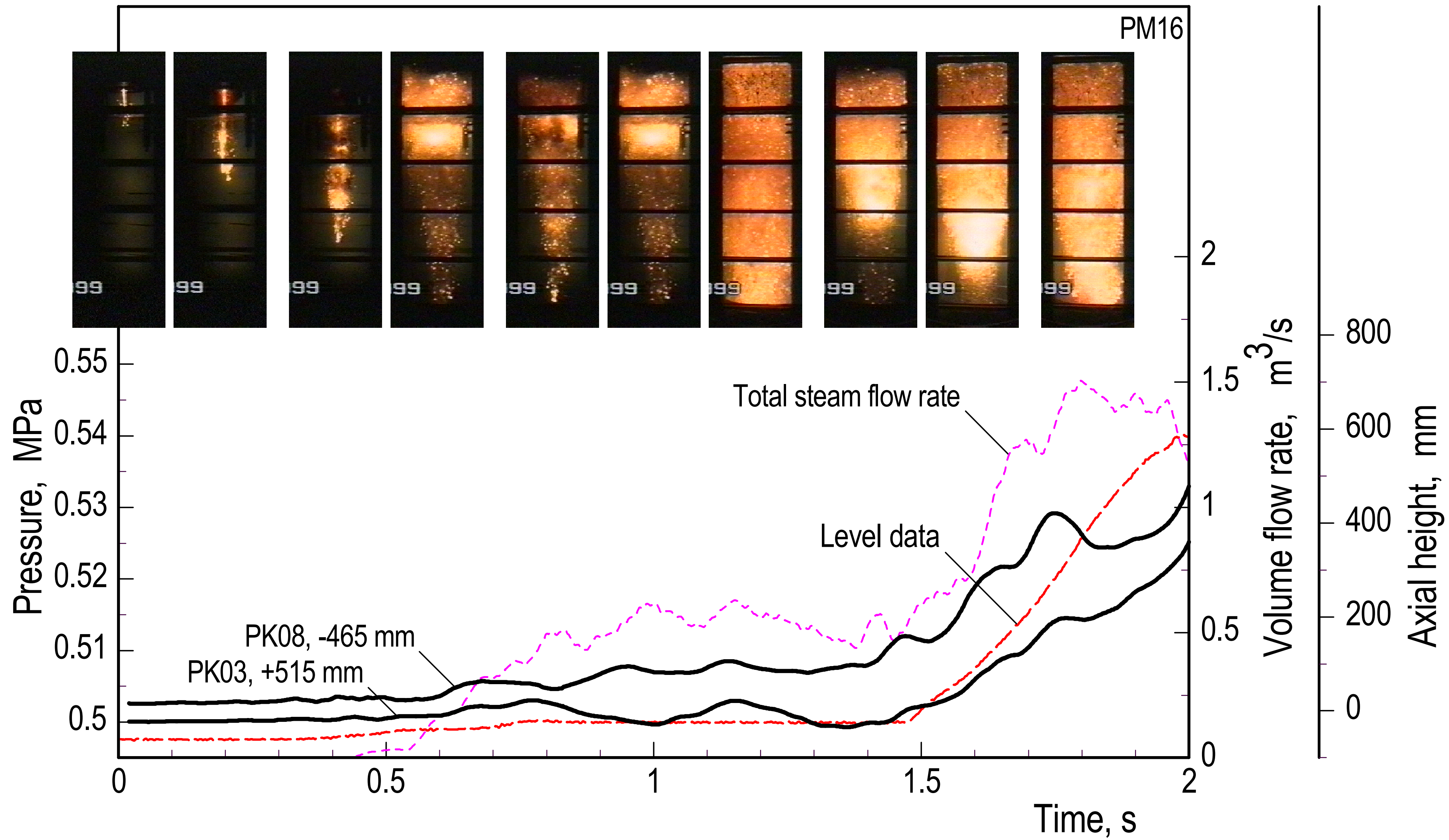

Fig. B2: PM16. Video frames referring to peculiar events visibly in the signal traces.

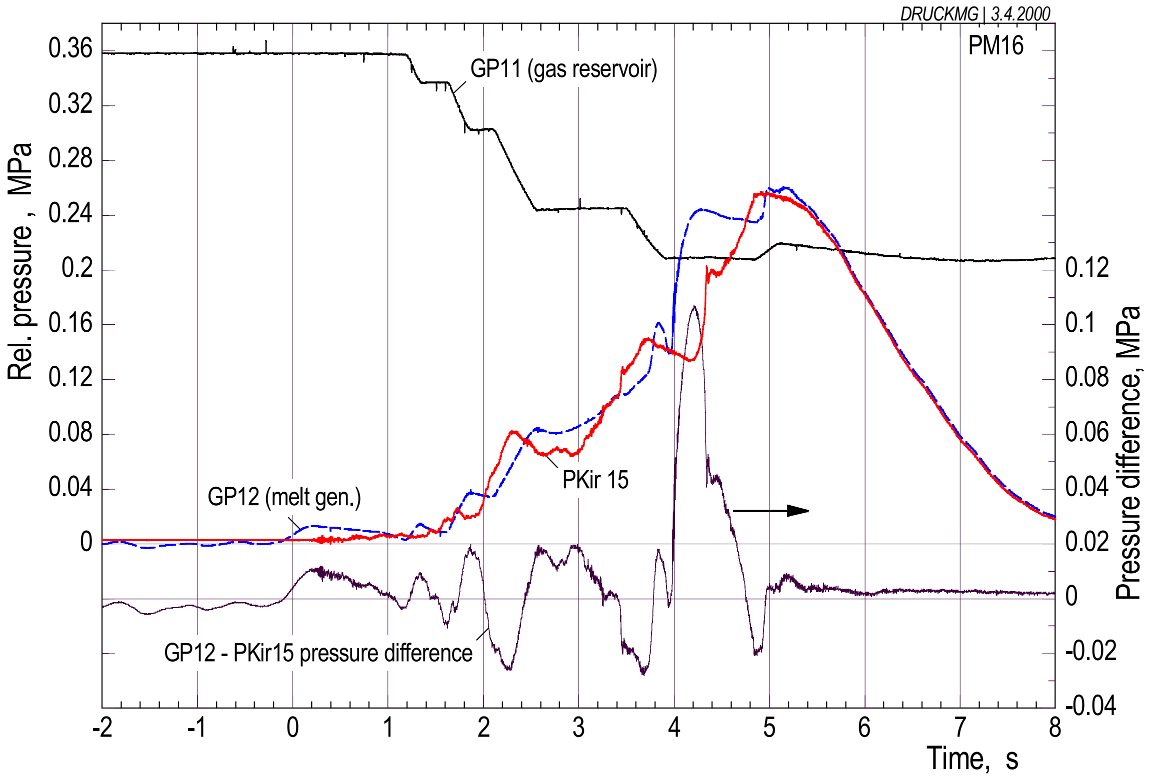

Fig. B3: PM16. Pressures controlling the melt release.

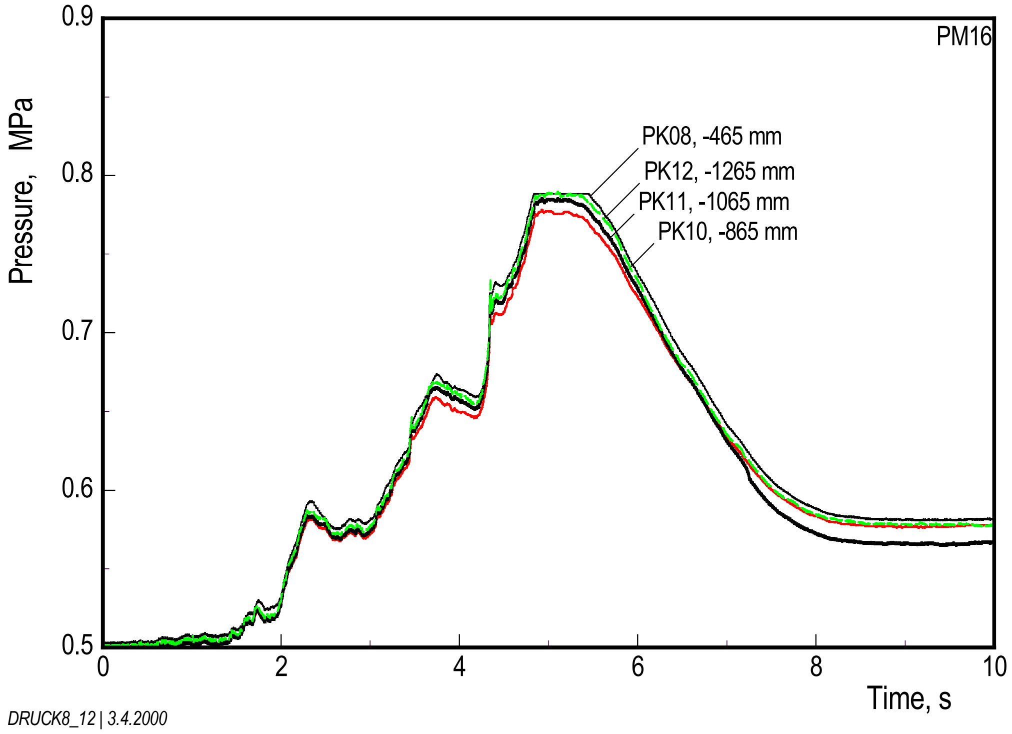

Fig. B4: PM16. Pressures measured in the water.

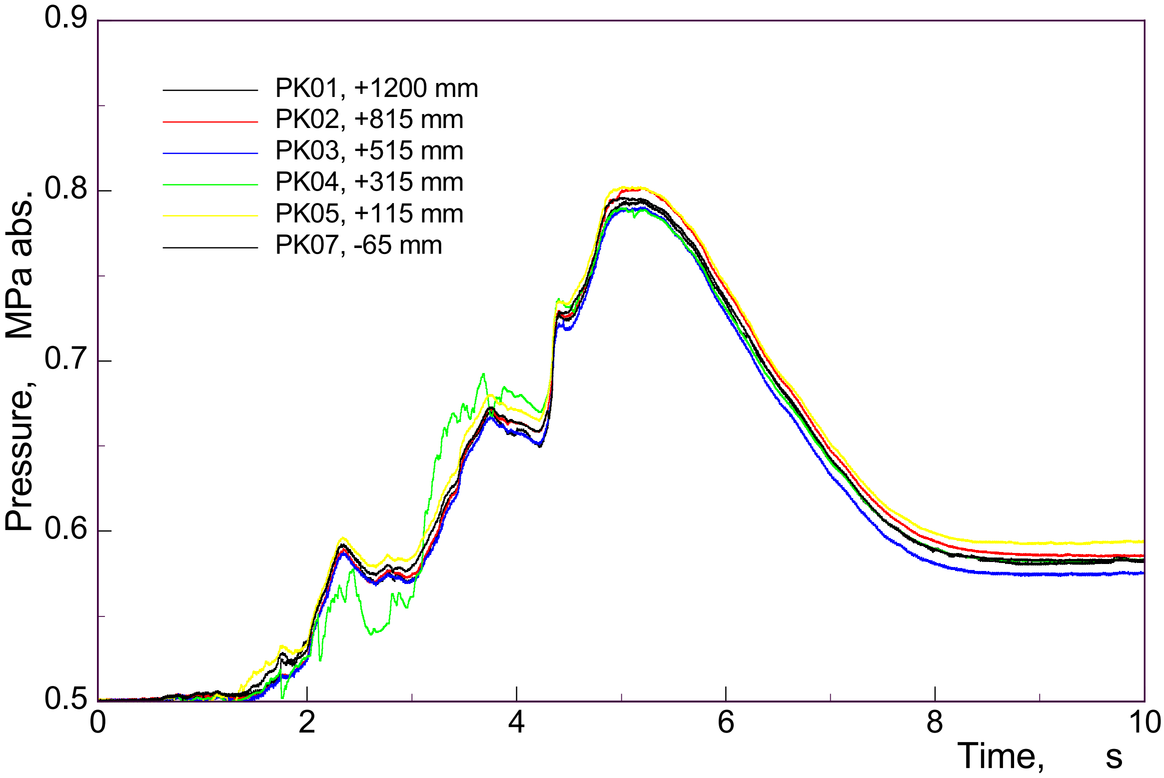

Fig. B5: PM16. Pressures in the gas compartment.

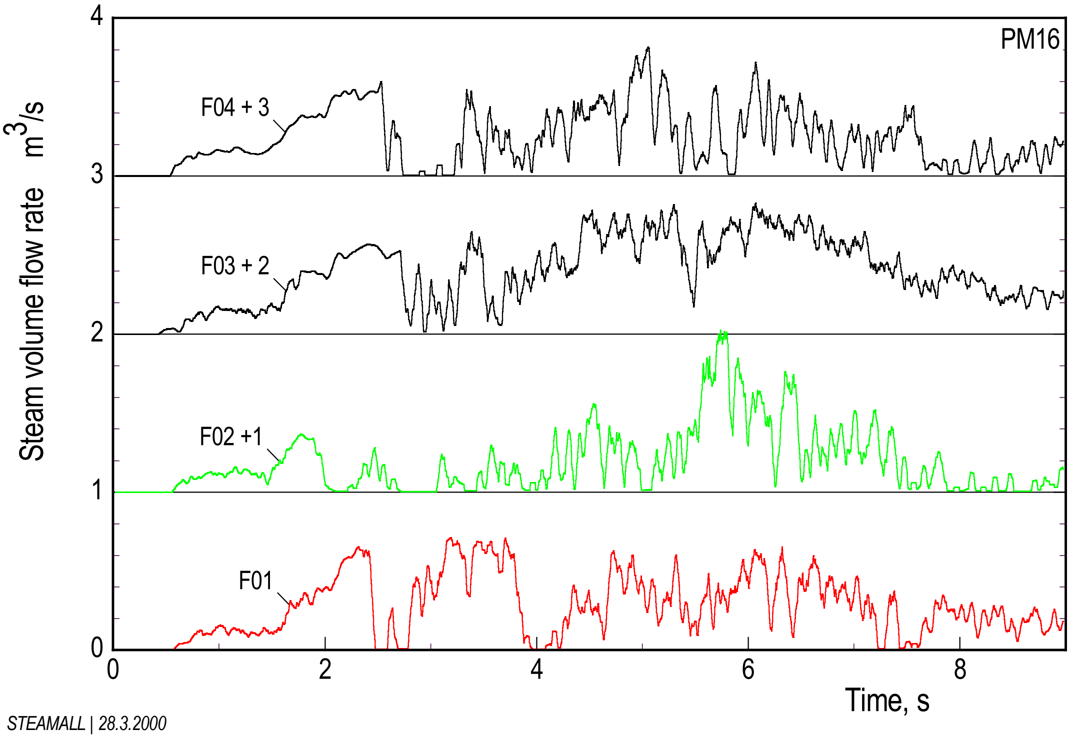

Fig. B6: PM16. Measured steam generation rate.

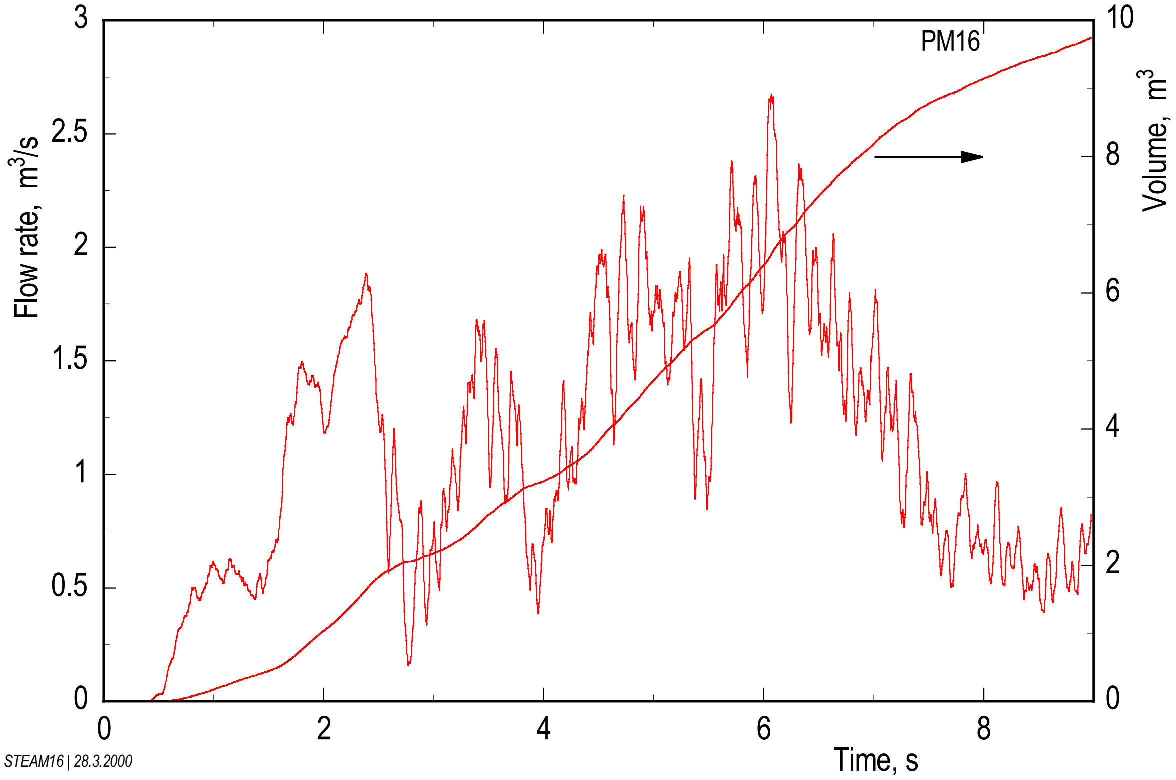

Fig. B7: PM16. Total steam volume flow and integrated steam volume.

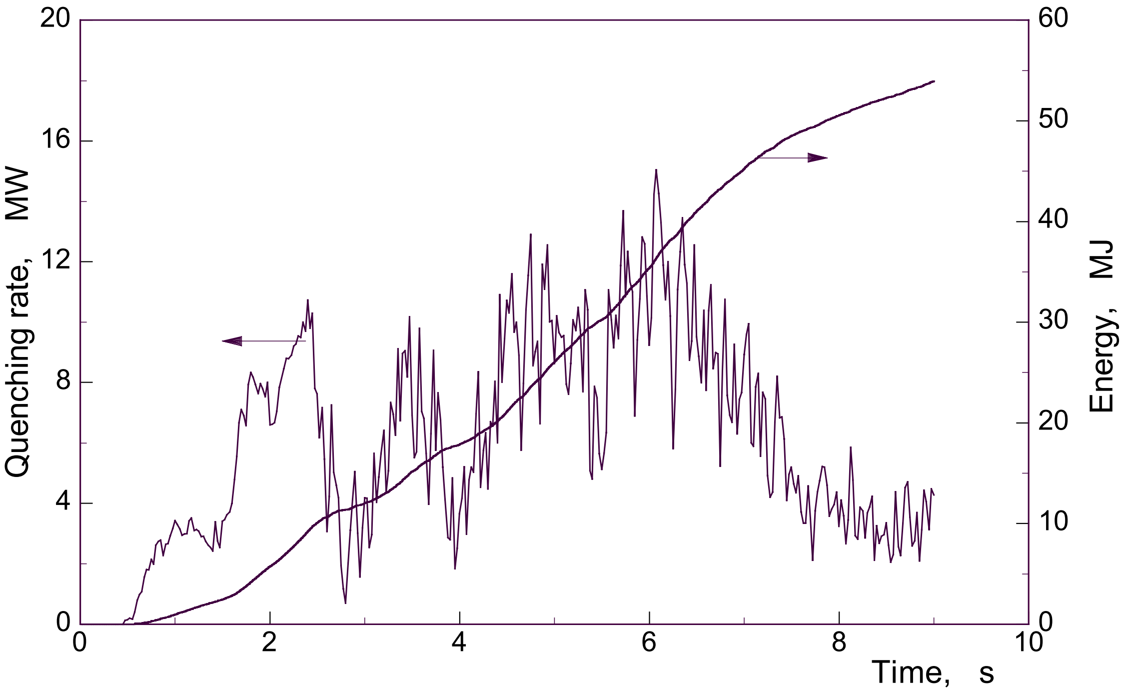

Fig. B8: PM16. Quenching rate calculated from steam production rate and integrated energy transferred.

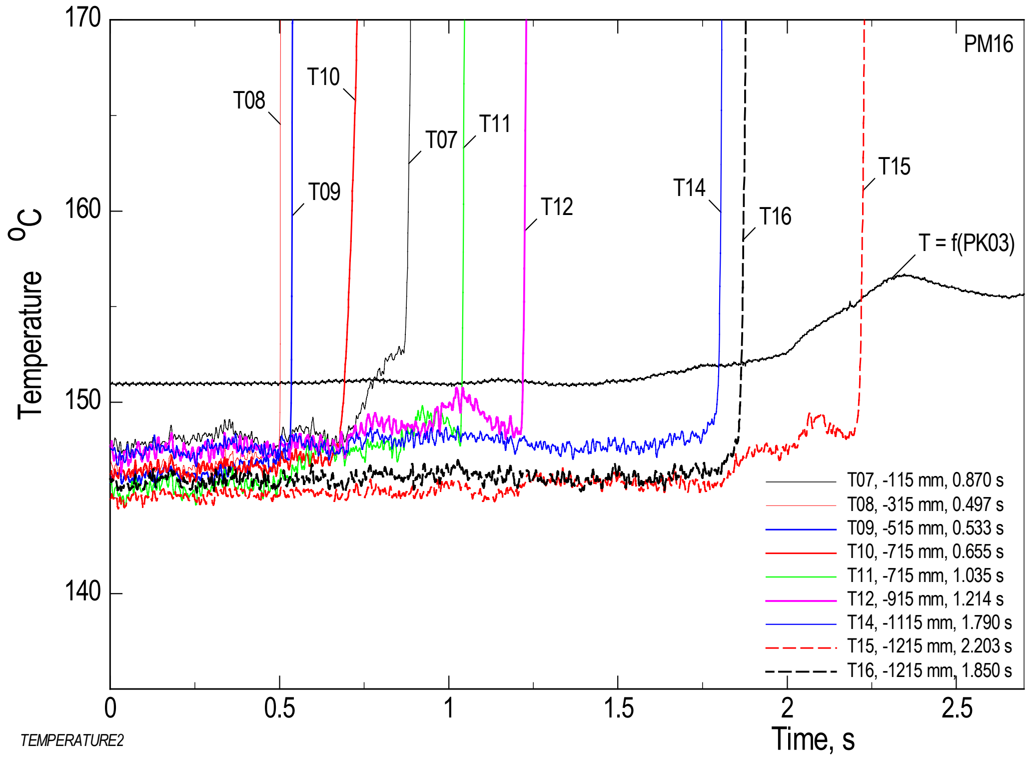

Fig. B9: PM16. Temperatures measured in the water together with the saturation temperature corresponding to the PK03 pressure. The times give the instants postulated of thermocouple damage.

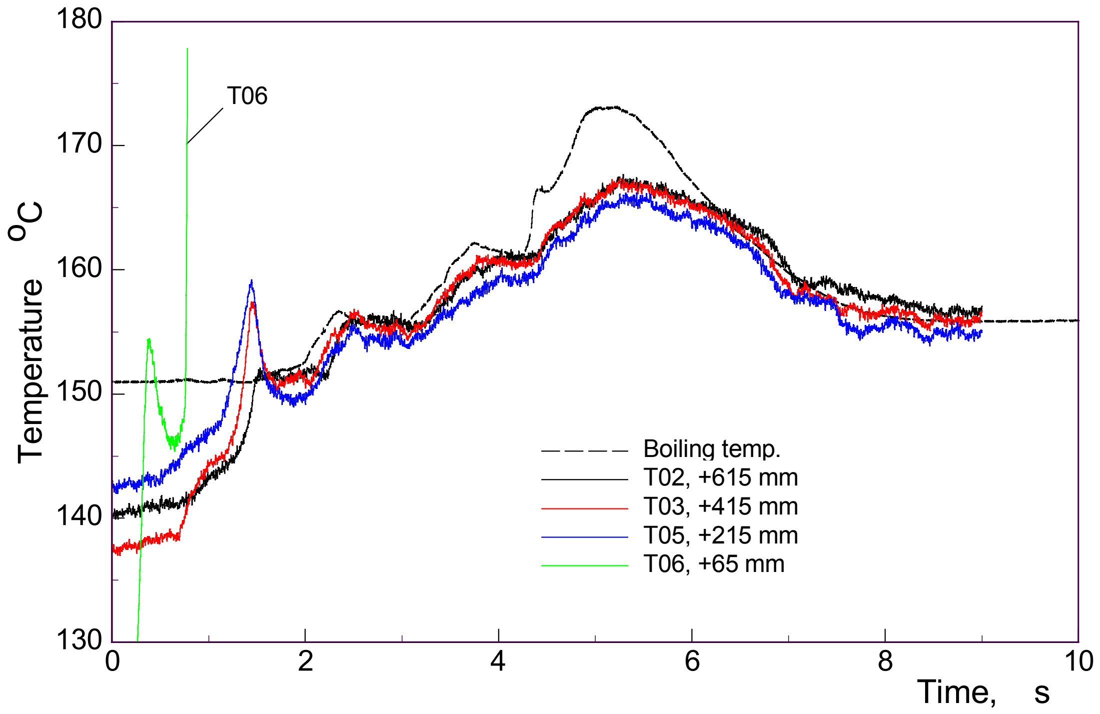

Fig. B10: PM16. Temperatures measured in the gas space. Comparison is made with the saturation temperature which corresponds to the pressure measurement.

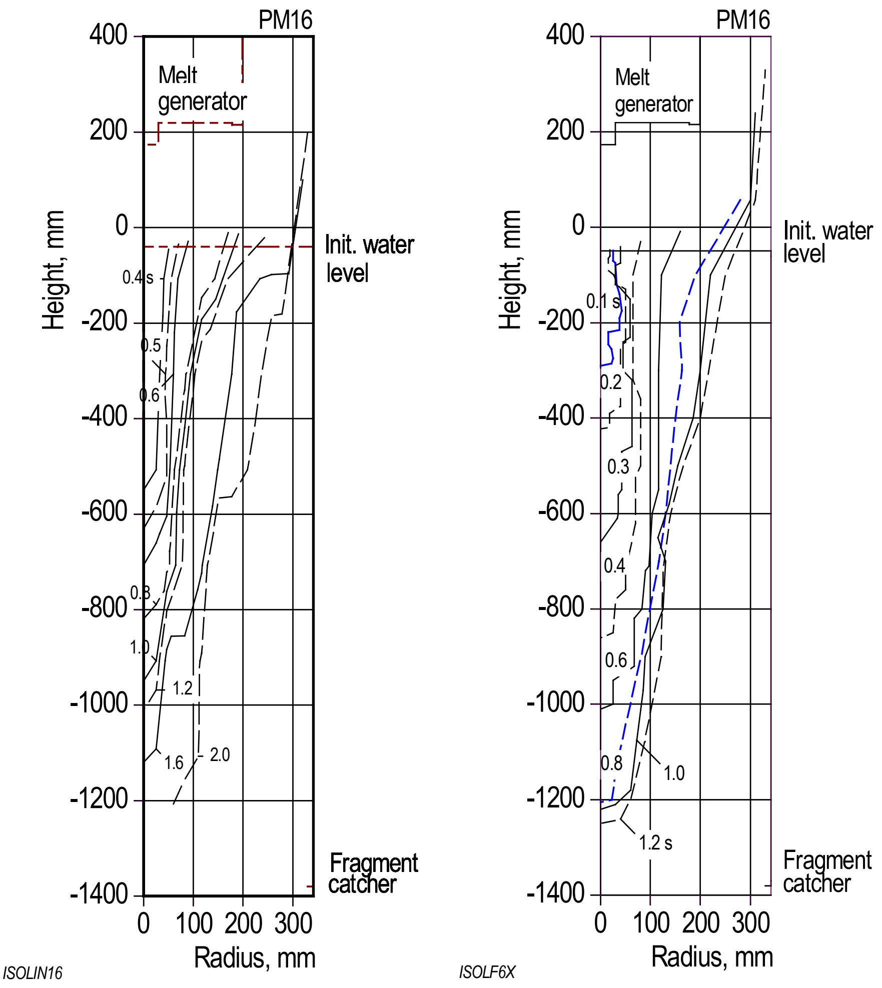

(a) (b)

Fig. B 11: PM16. Progression of the interaction zone into the water with the time as a parameter obtained on basis of void signals (a) and of film pictures (b).

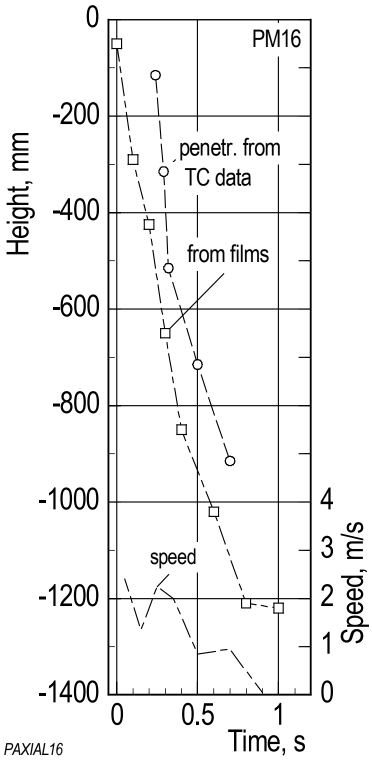

Fig. B 12: PM16. Axial progression of the melt and the speed of the leading edge. The latter is derived from the film data.

Fig. B 13: PM 16. Local distribution of steam and water obtained from void probes at selected times. Dark points on base line=water; bright elevated points=steam.

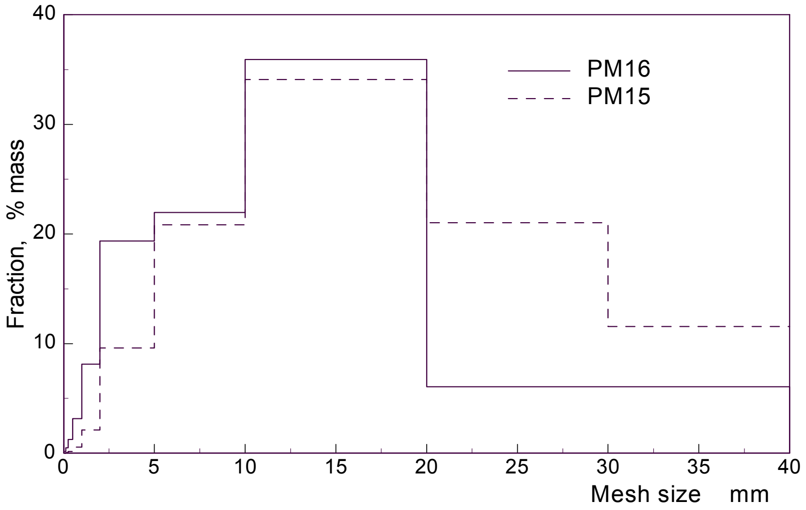

Fig. B 14: Sieve analysis of the loose particles.

Appendix C: Test PM17

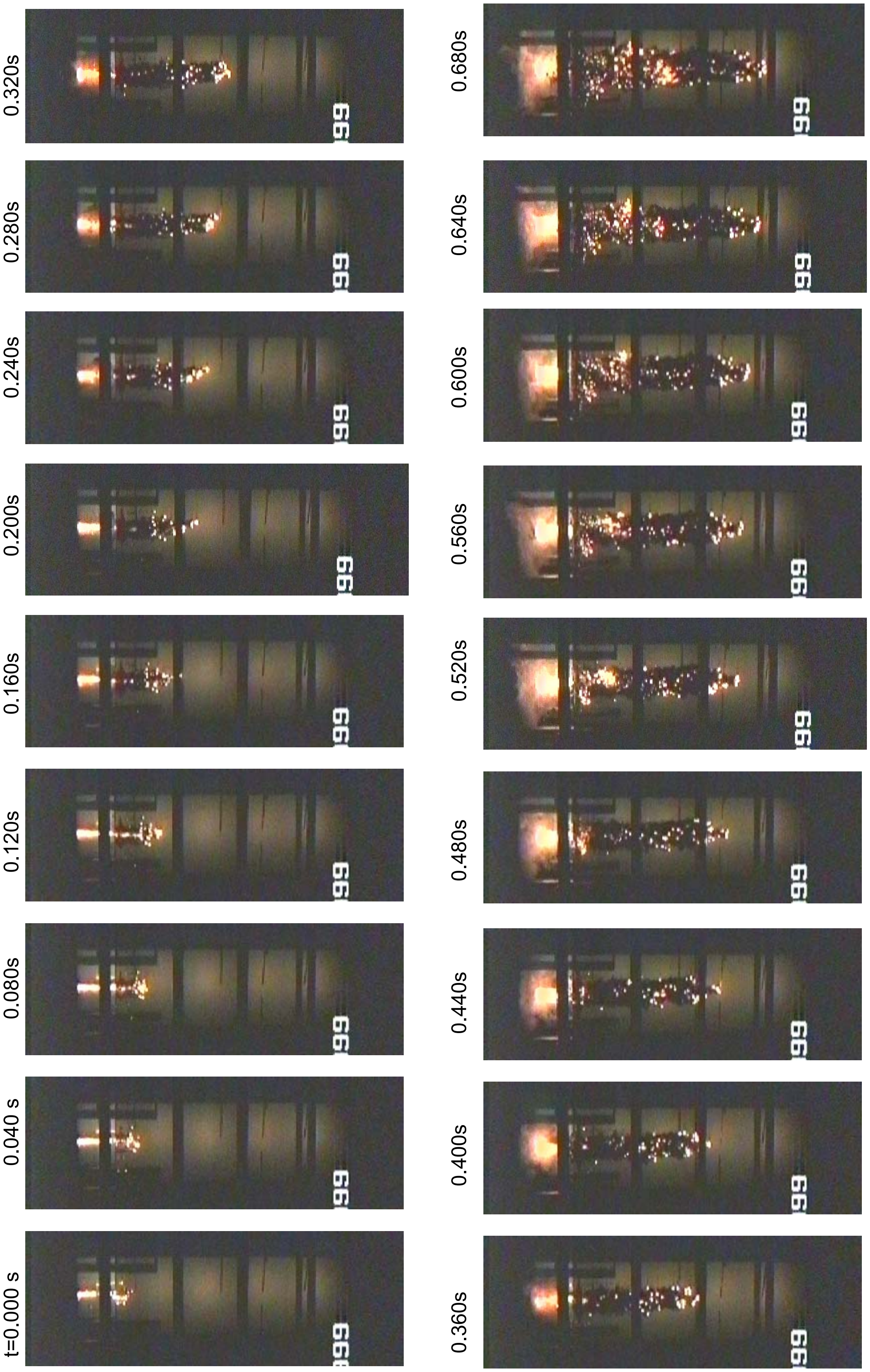

Fig. C1: PM17. Video pictures showing progression of interaction zone (small time steps).

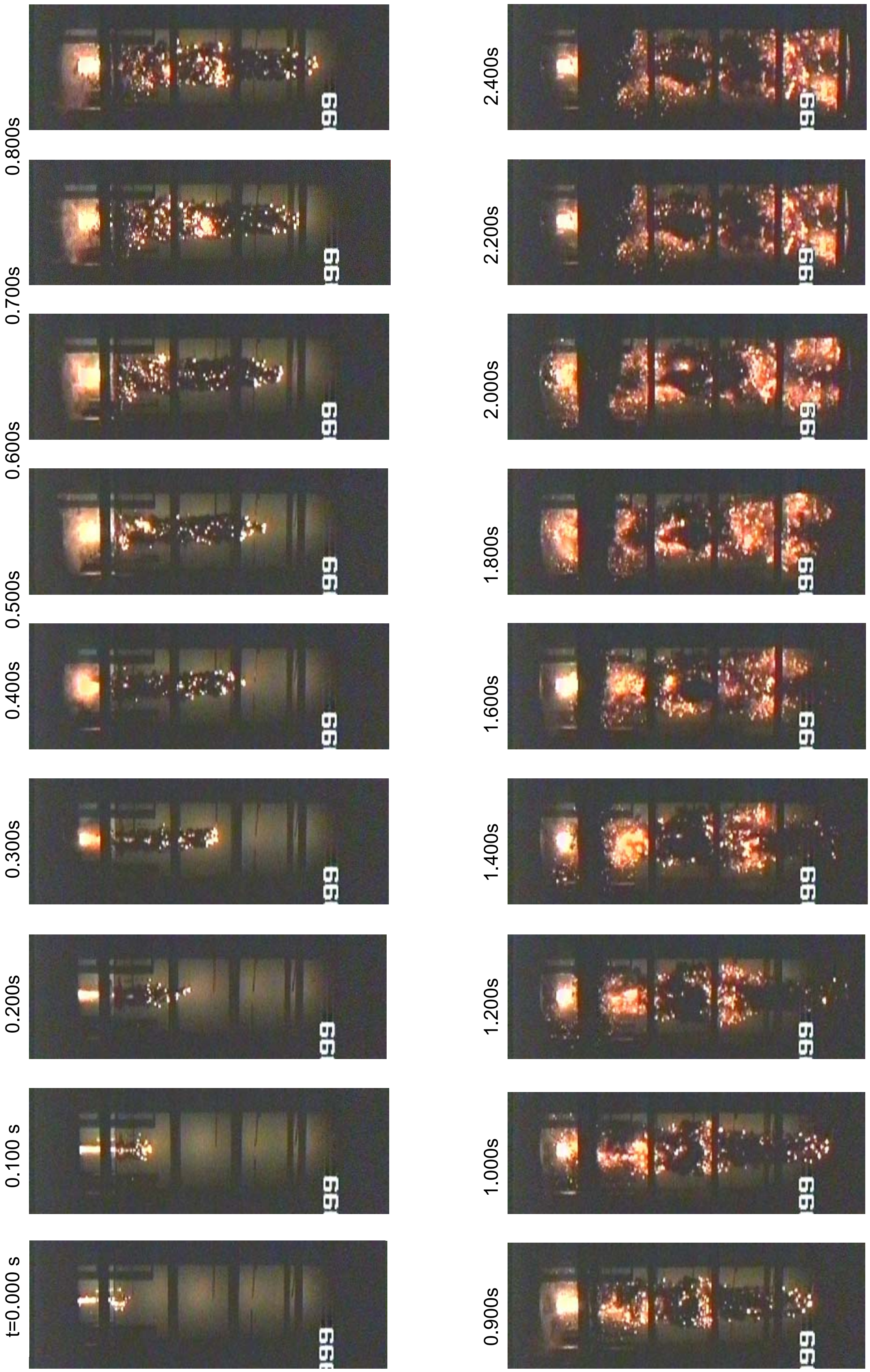

Fig. C2: PM17. Video pictures showing progression of interaction zone (larger time steps).

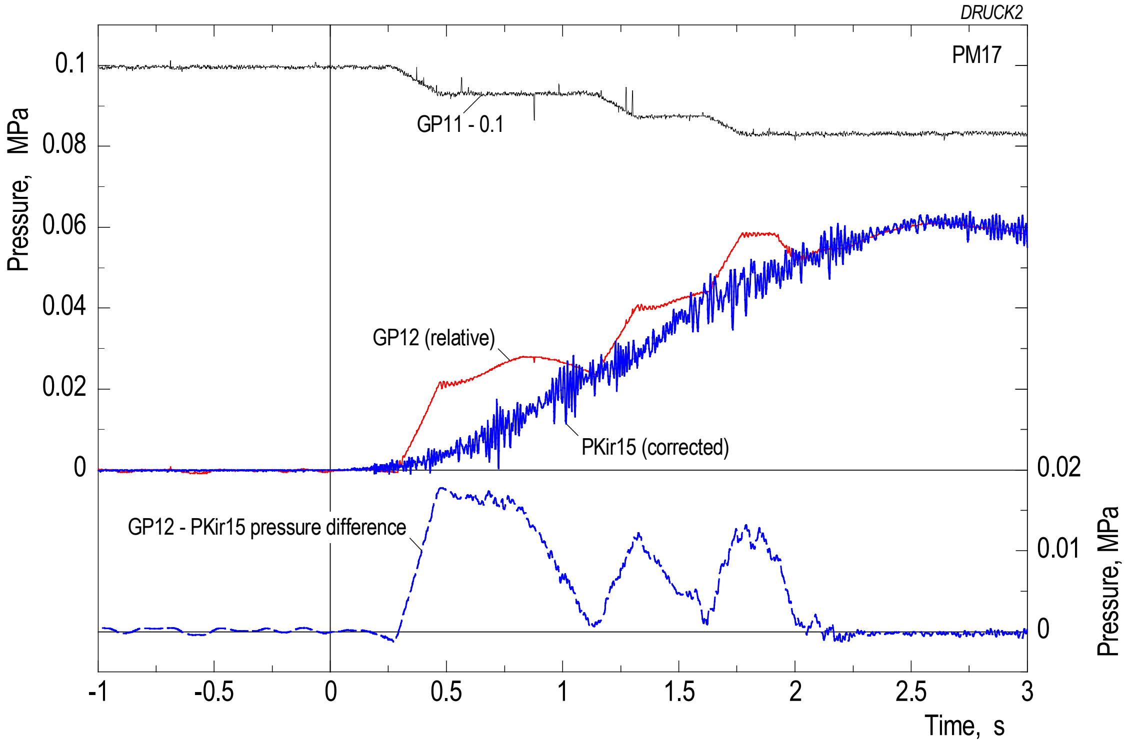

Fig. C3: PM17. Pressures controlling melt release.

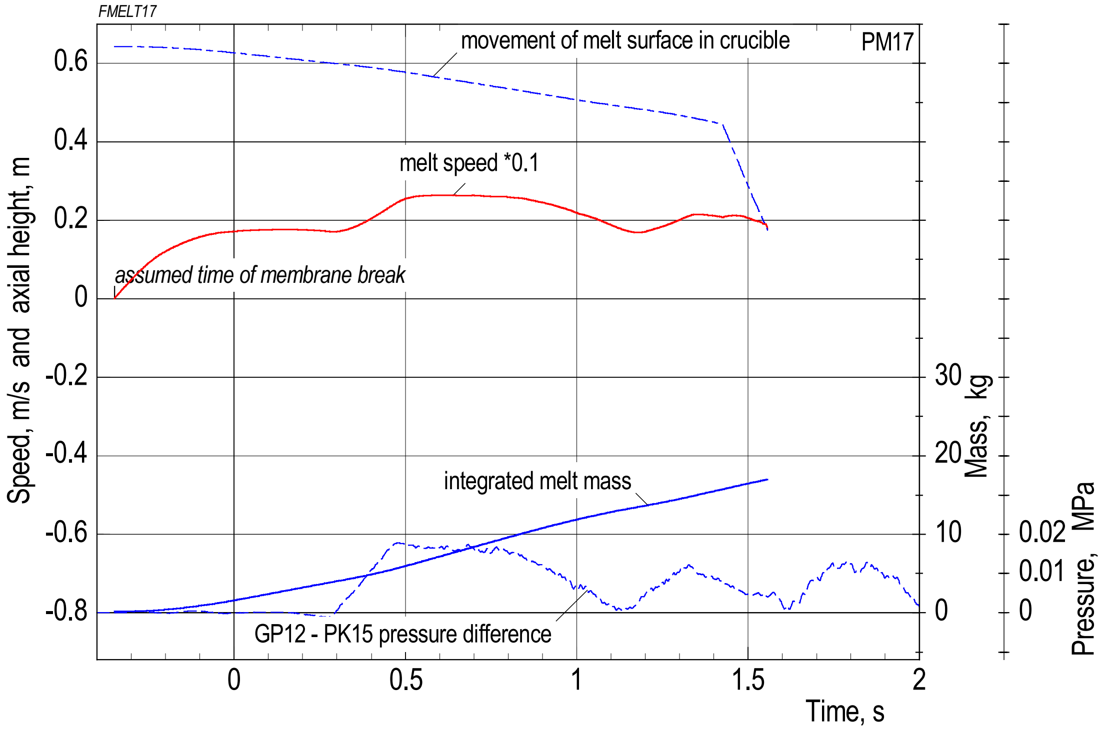

Fig. C4: PM17. Melt release calculated on basis of the driving pressure.

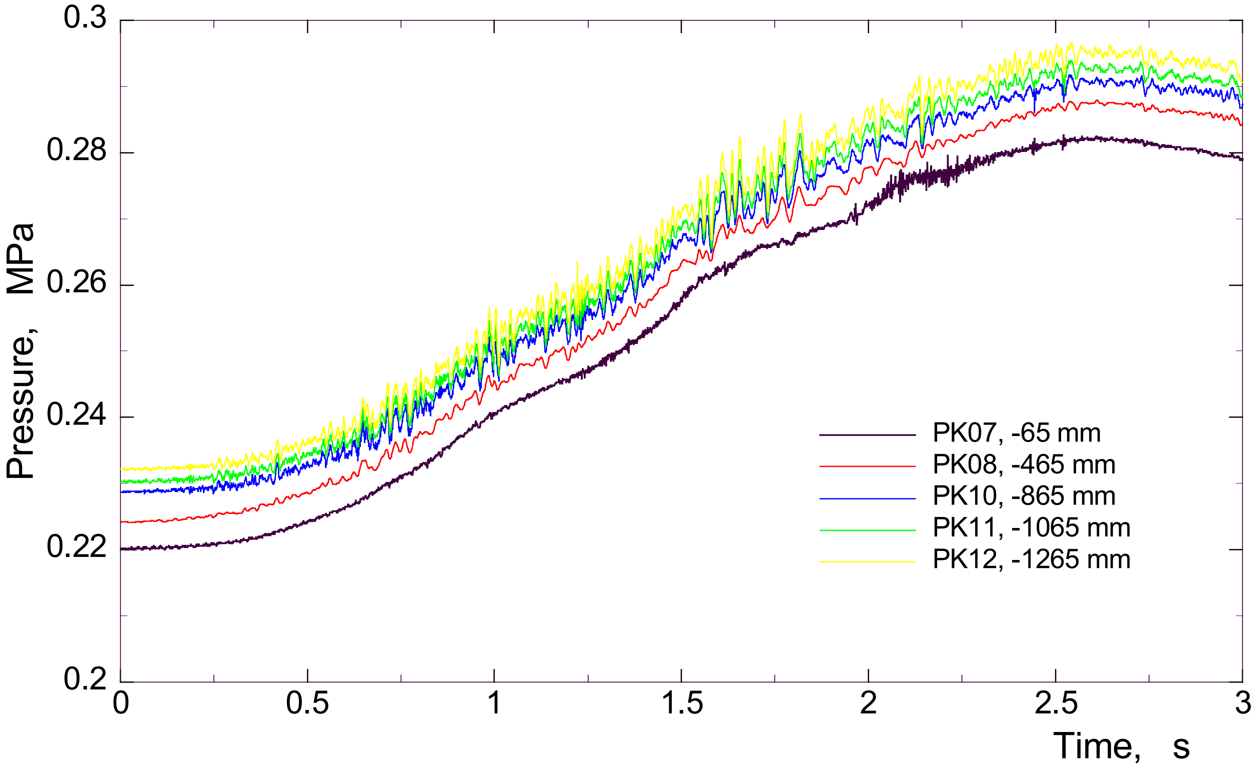

Fig. C5: PM17. Pressures measured in the water.

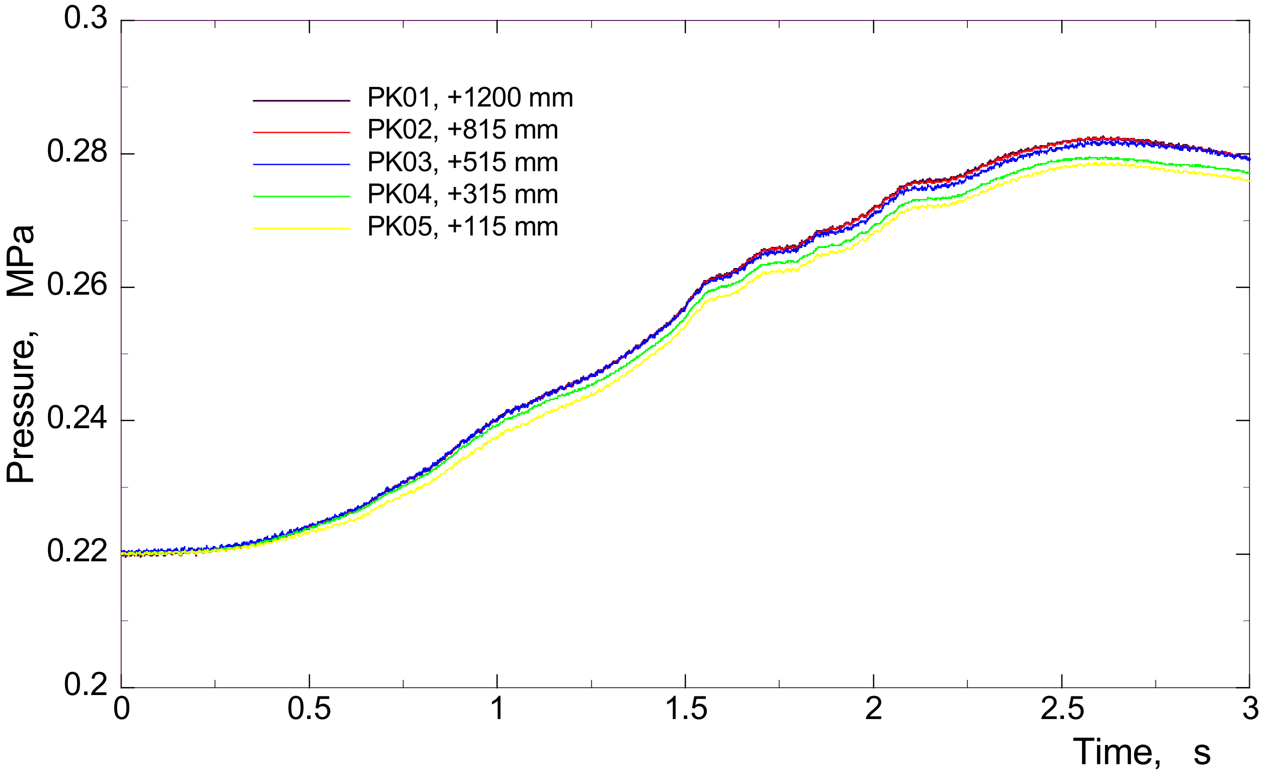

Fig. C6: PM17. Pressures measured in the gas compartment.

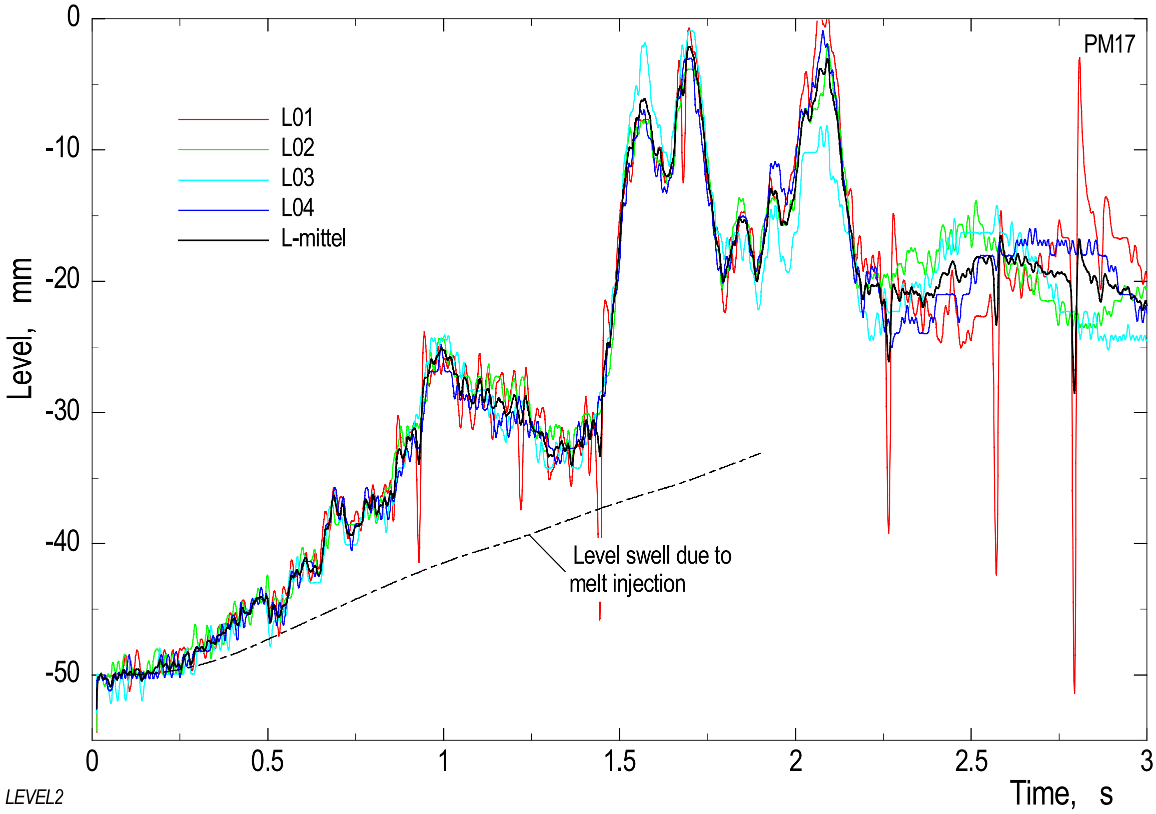

Fig. C7: PM17. Change in the water level.

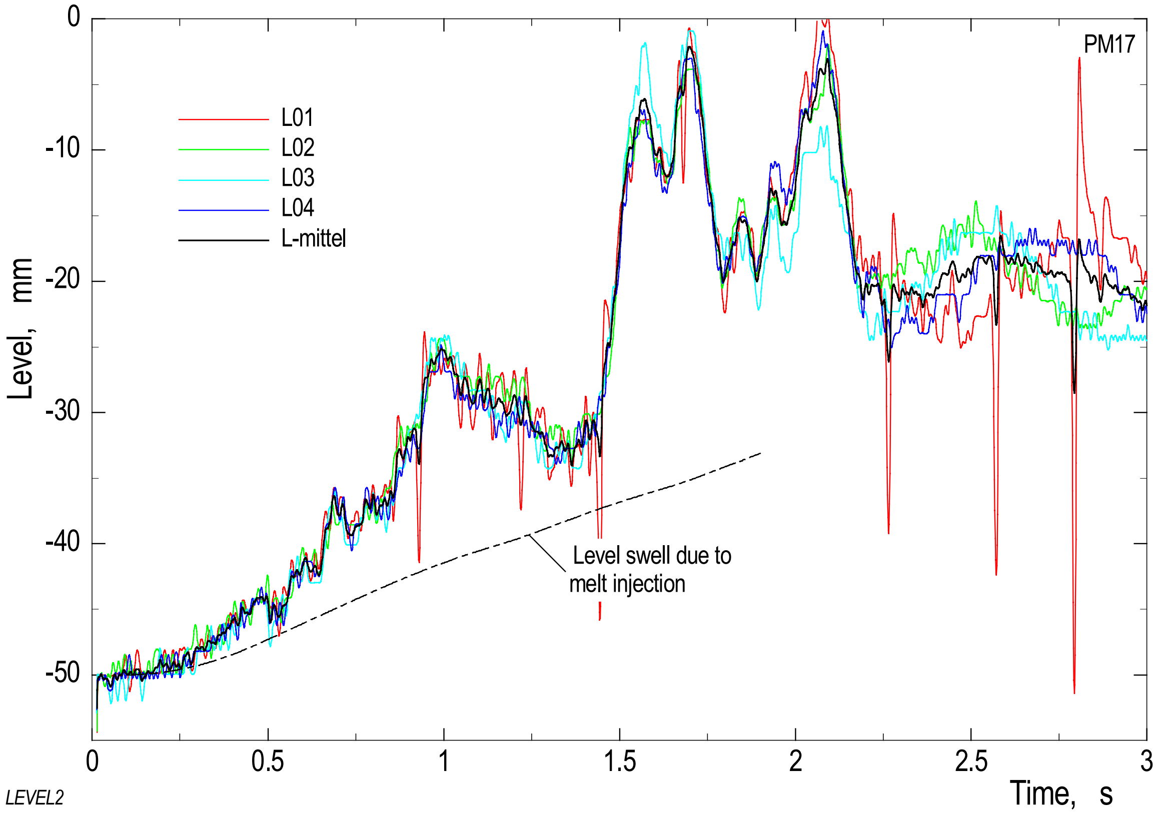

Fig. C8: PM17. Temperatures measured in the water.

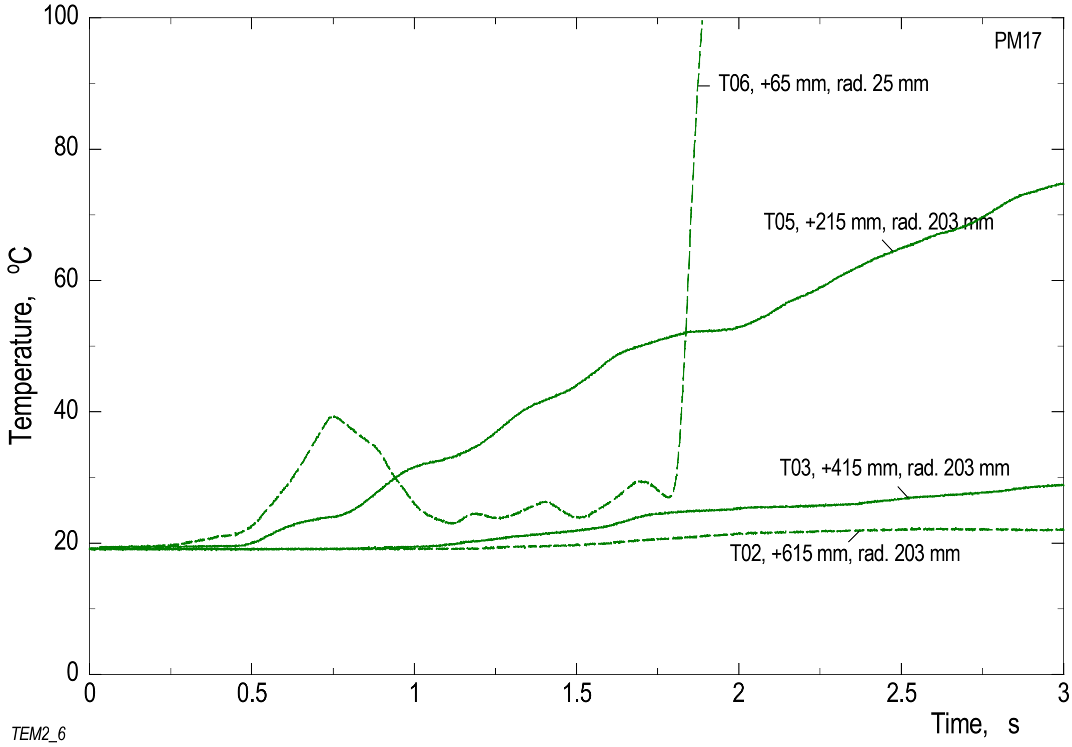

Fig. C9: PM17. Temperatures measured in the gas compartment.

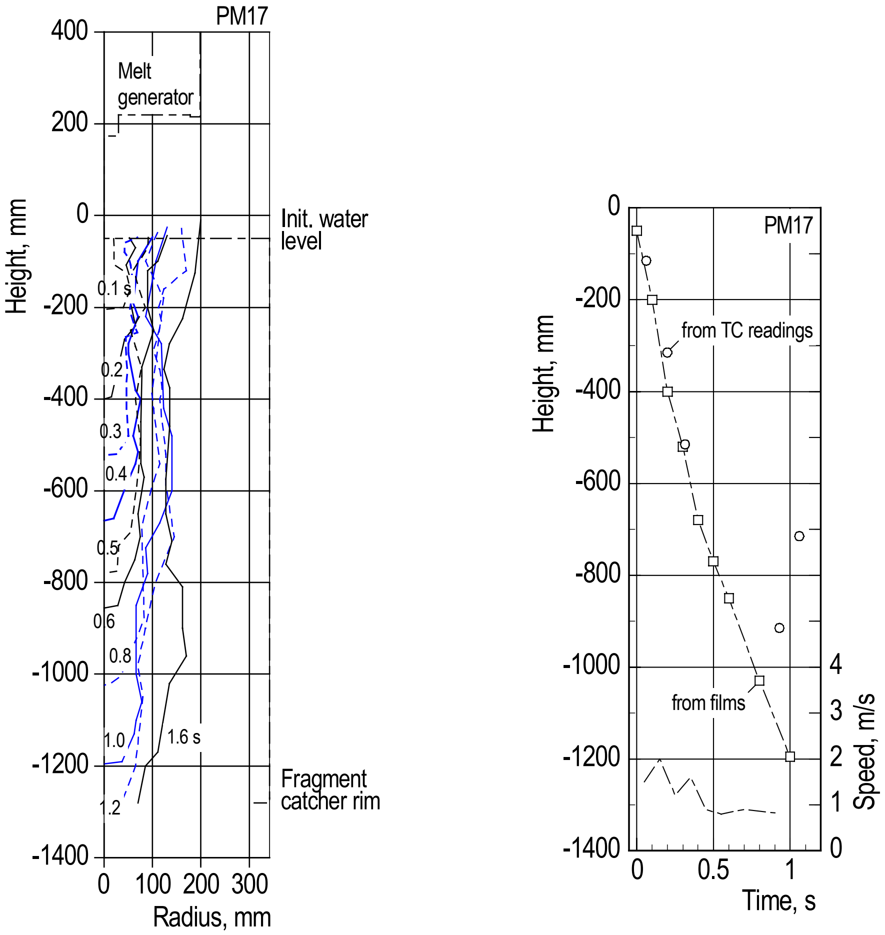

Fig. C10: Progression of the interaction zone in the axial and radial directions with the time as a parameter (left hand side). Axial progression and derived speed of the leading edge of the melt (right hand side).

Fig. C11: PM17. Local distribution of steam and water obtained from void probes at selected times. Dark points on base line=water; bright elevated points=steam.

Fig. C11: PM17. Local distribution of steam and water (continued).

Appendix D: Test PM18

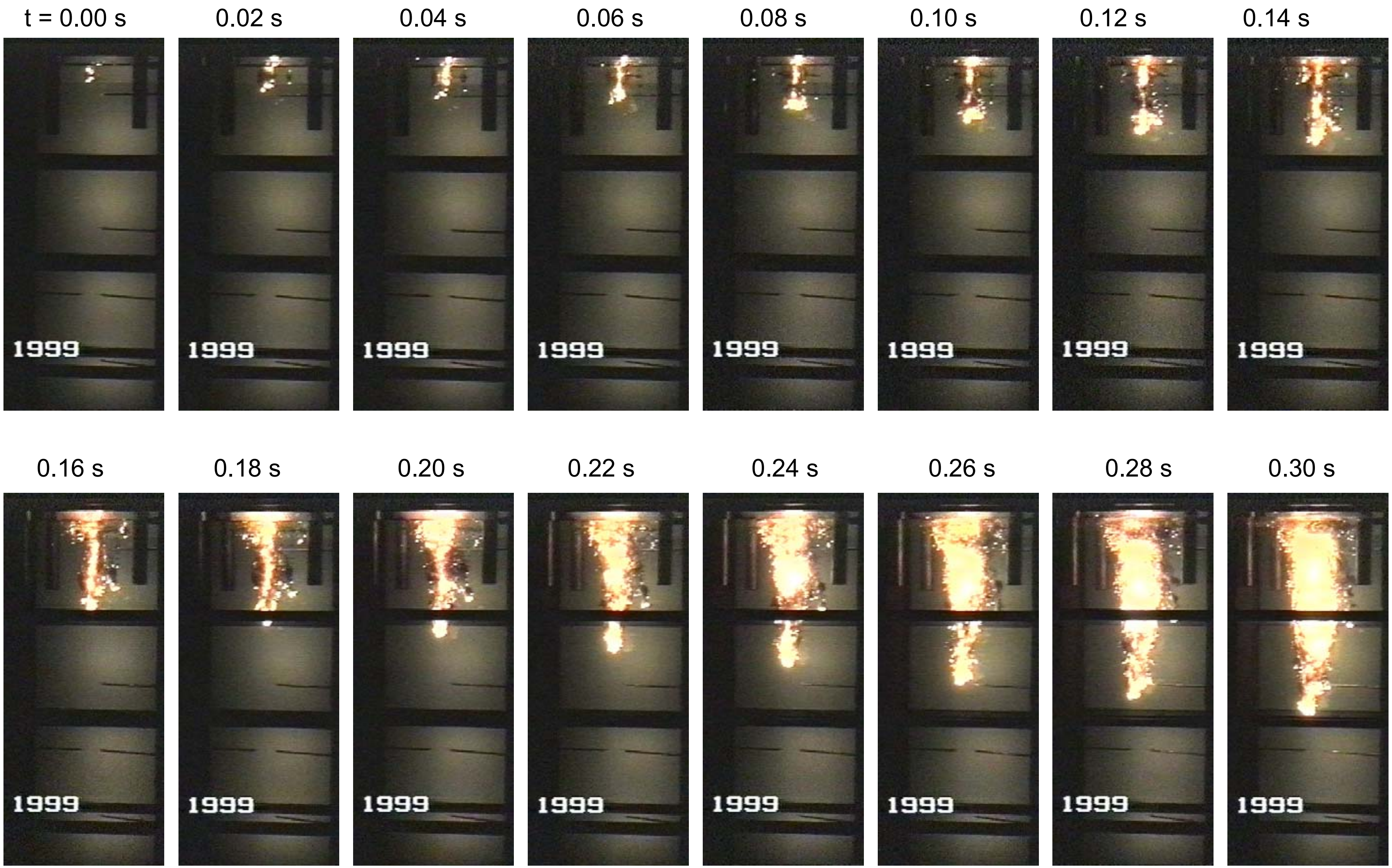

Fig. D1: PM18. Progression of the interaction zone under the condition of moderate initial water subcooling (26 K). Part 1: smaller time steps.

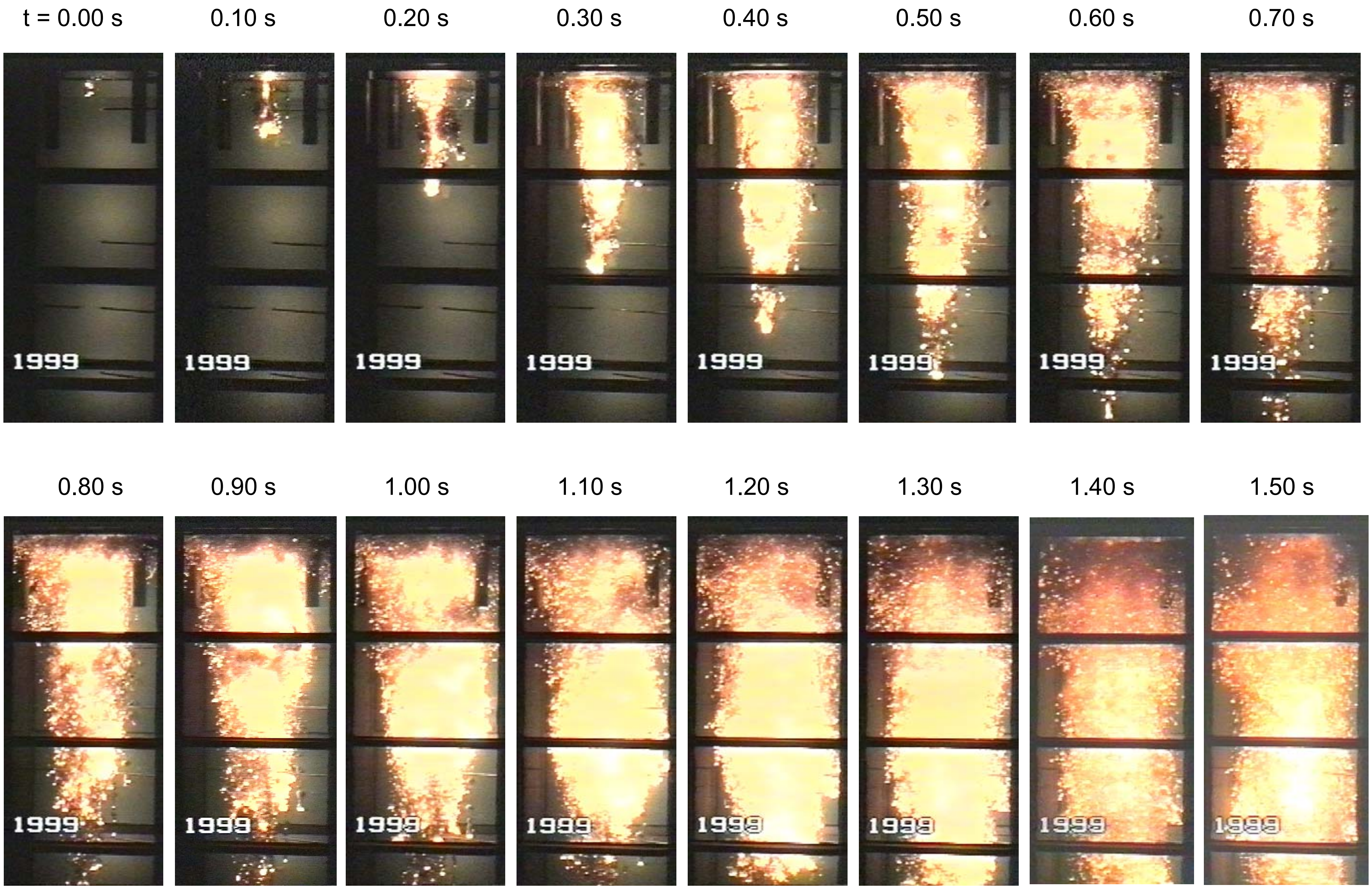

Fig. D2: PM18. Progression of the interaction zone. Part 2: larger time steps.

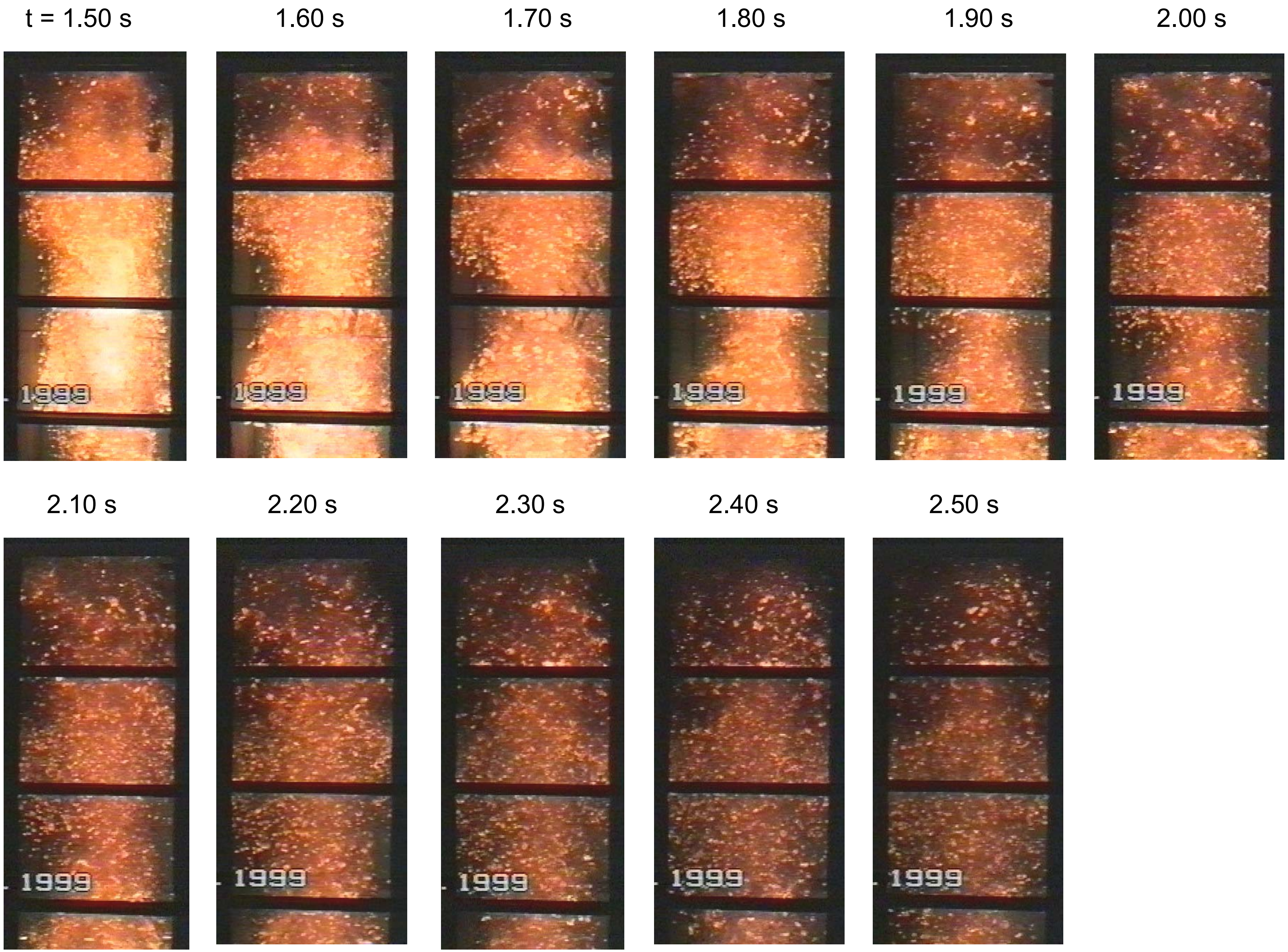

Fig. D3: PM18. Sequence of video frames taken after the end of melt release.

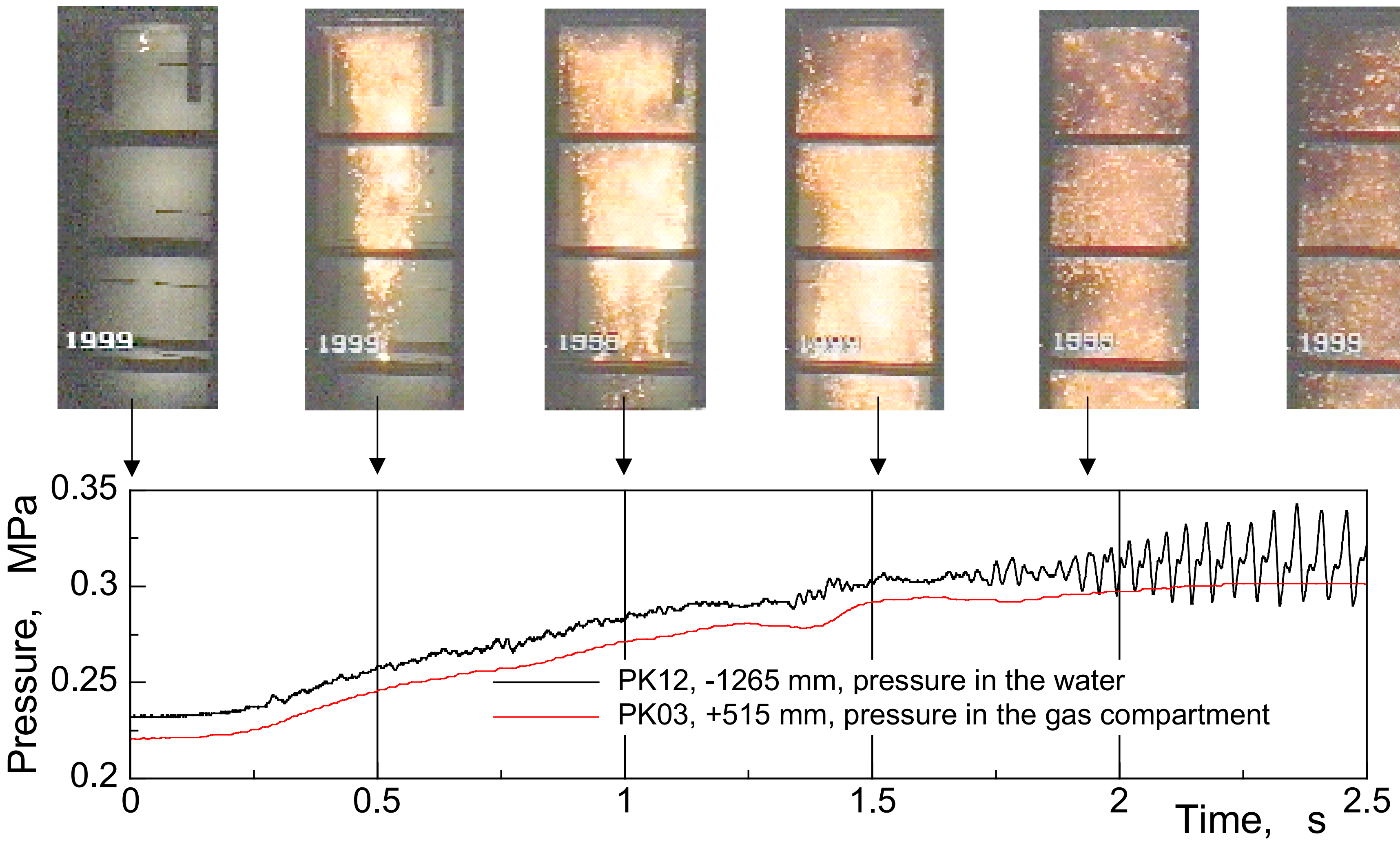

Fig. D4: PM18. Video frames correlated to the pressure time history.

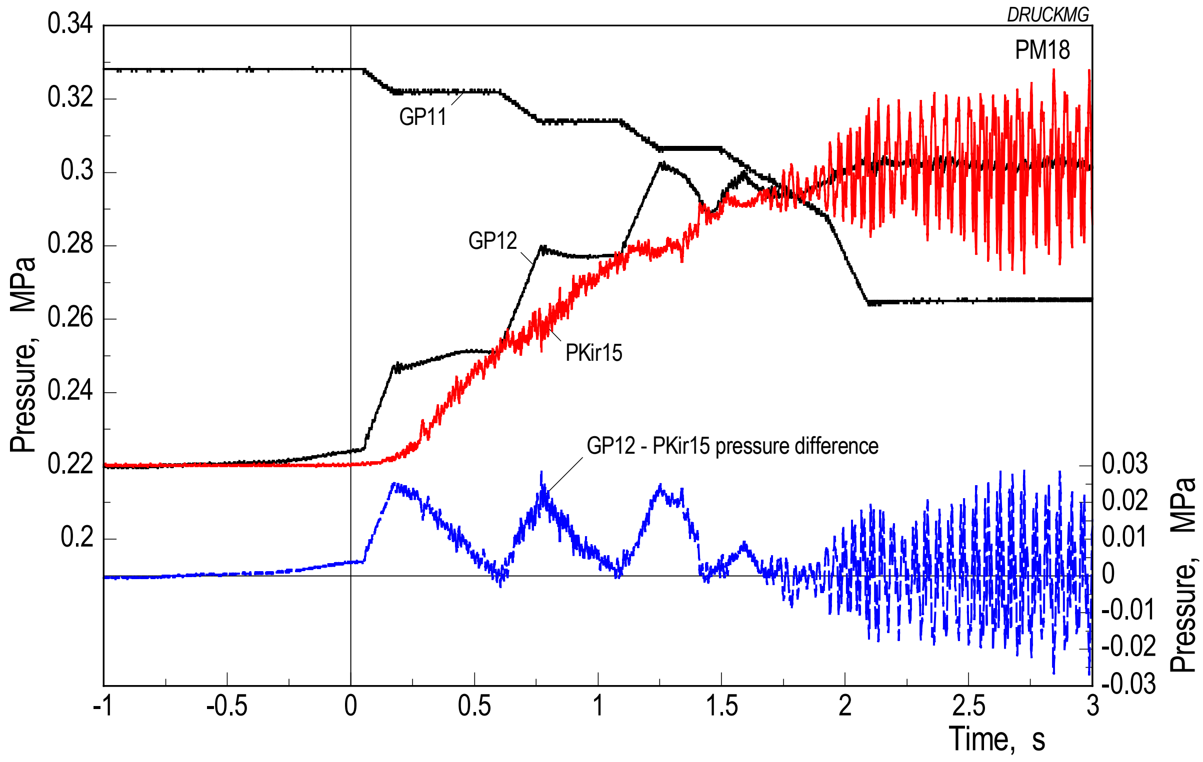

Fig. D5: PM18. Pressures controlling the melt release.

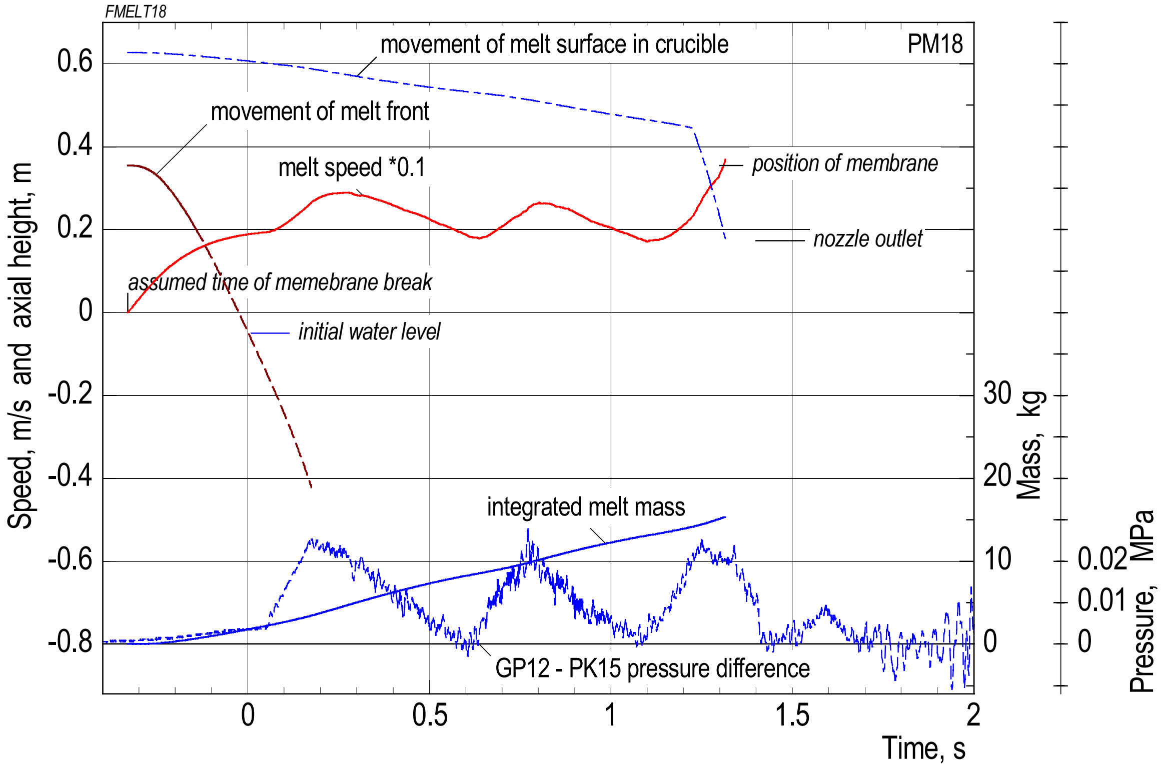

Fig. D6: PM18. Melt release calculated on basis of the pressure difference measured.

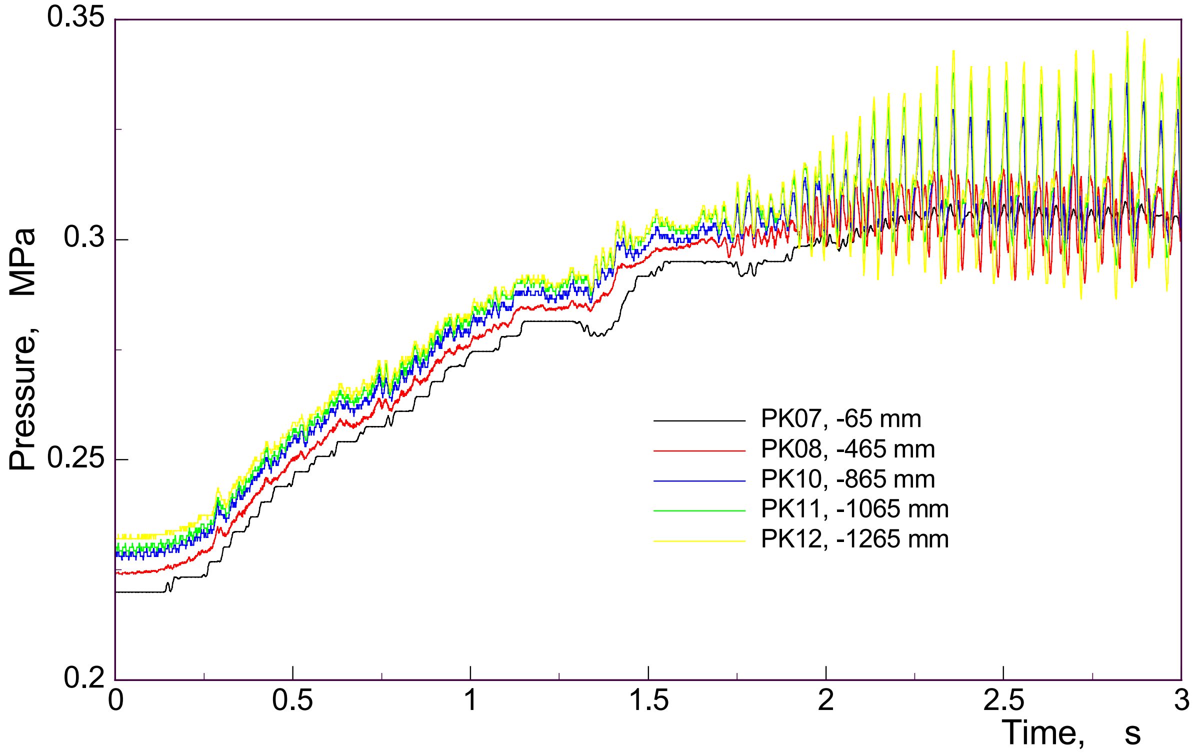

Fig. D7: PM18. Pressures measured in the water.

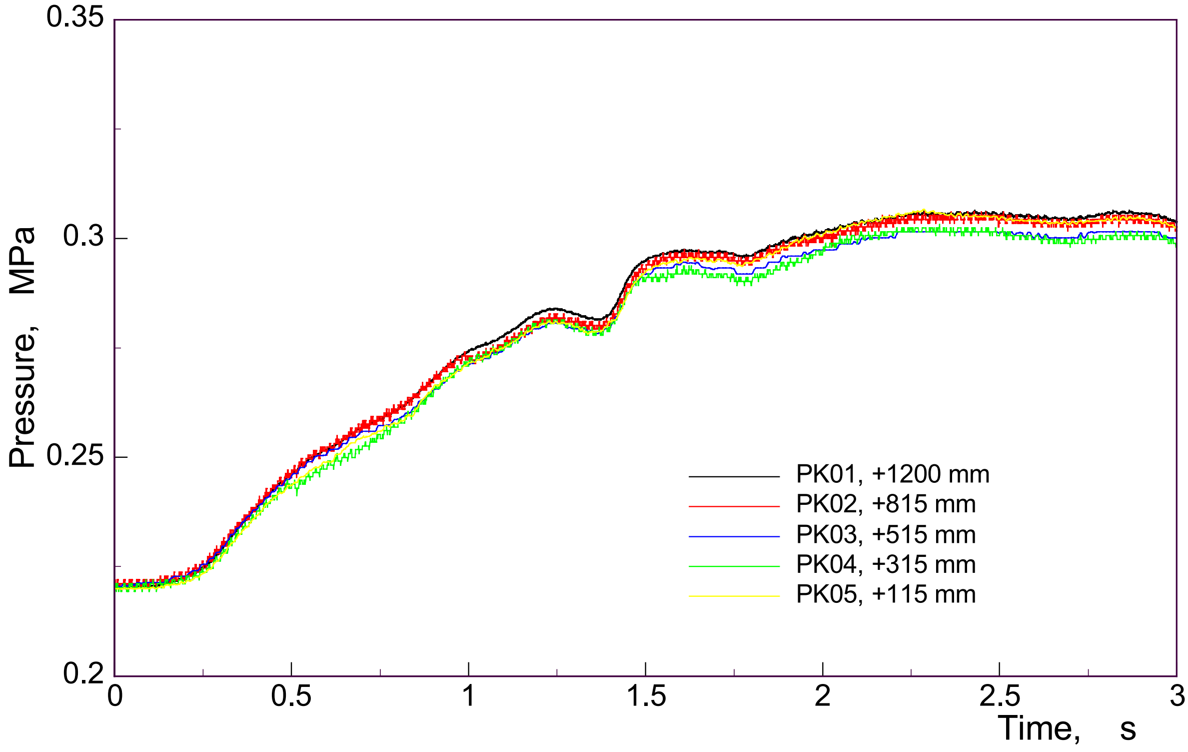

Fig. D8: PM18. Pressures measured in the gas space.

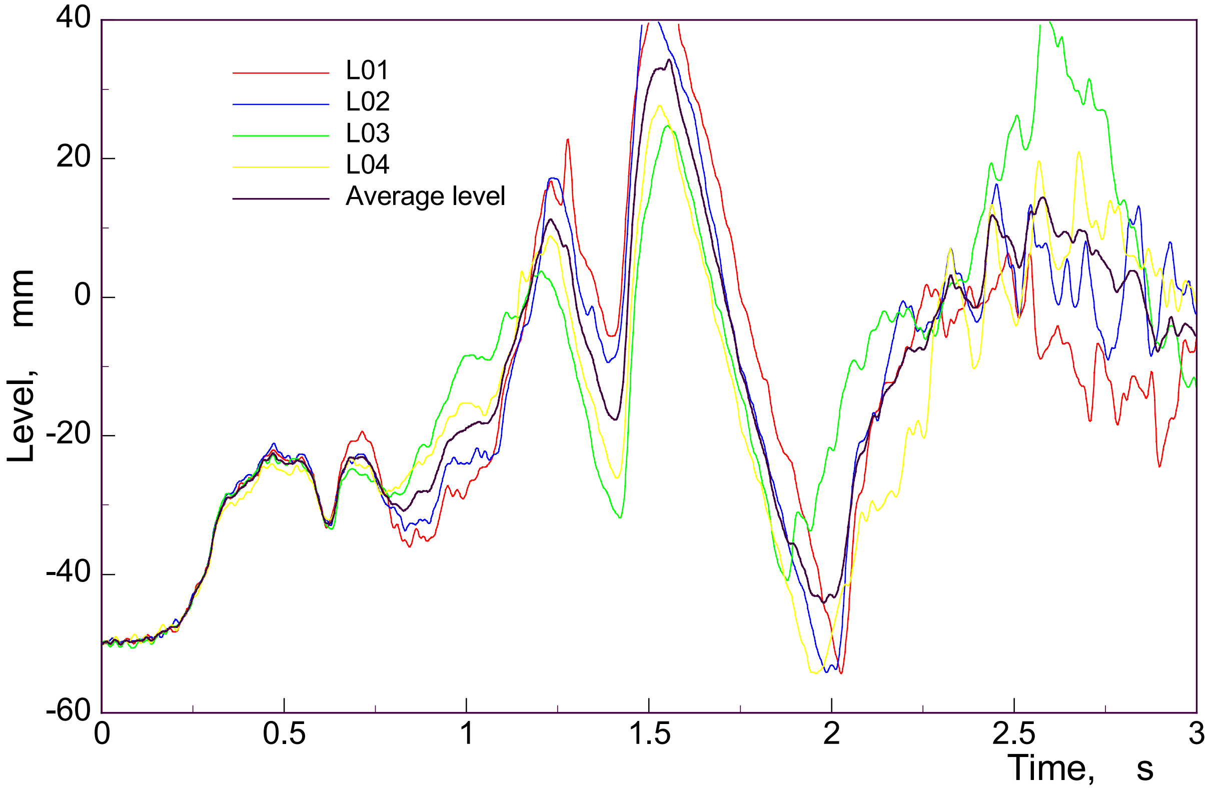

Fig. D9: PM18. Change in the water level.

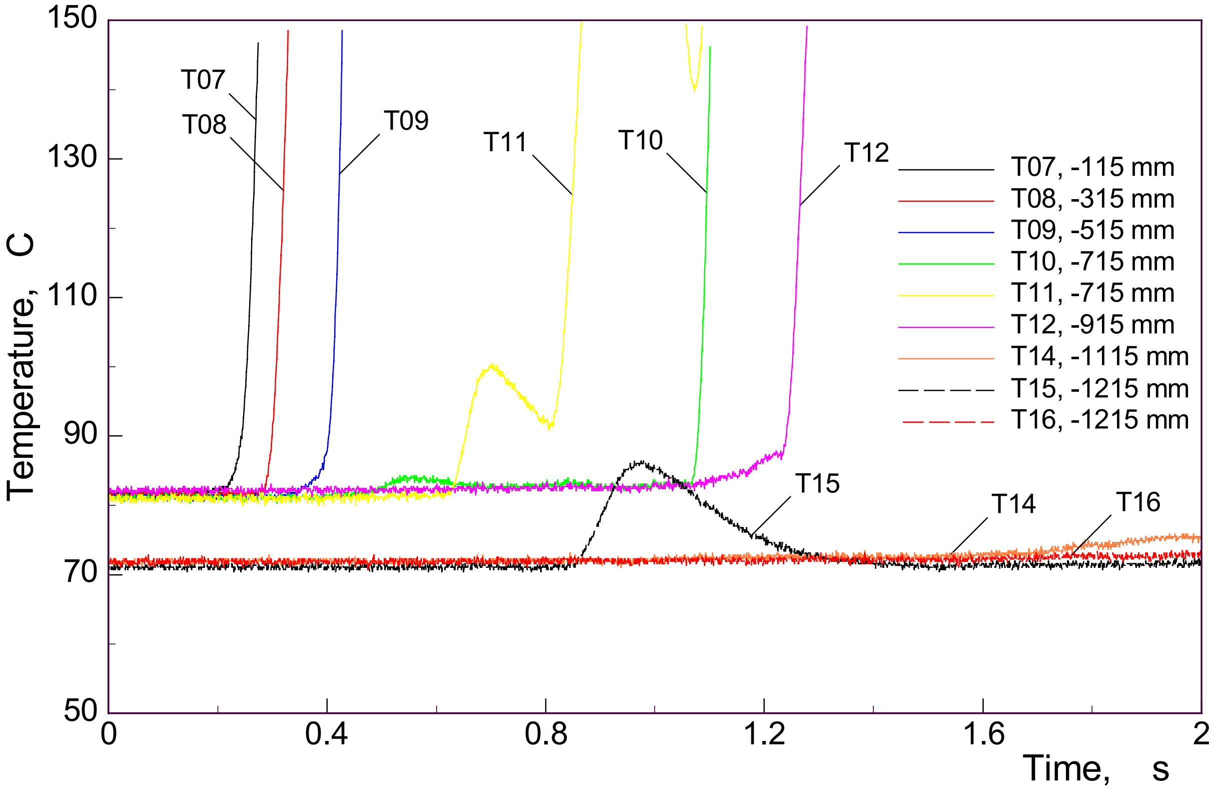

Fig. D10: PM18. Temperatures measured in the water.

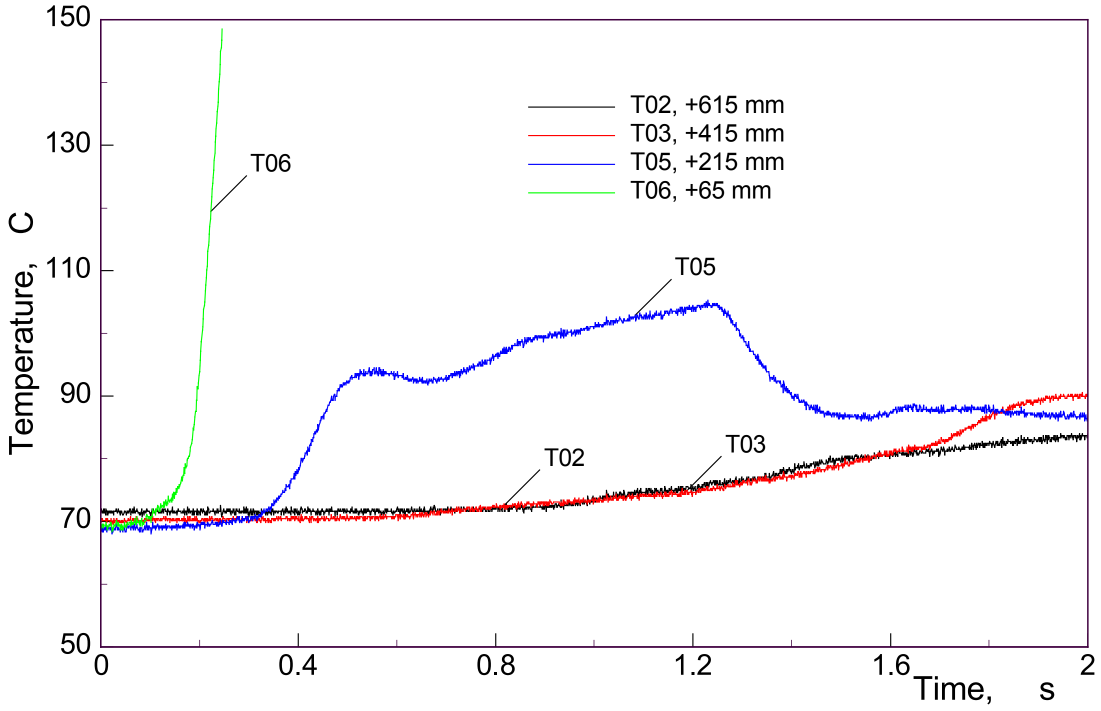

Fig. D11: PM18. Temperatures measured in the gas space.

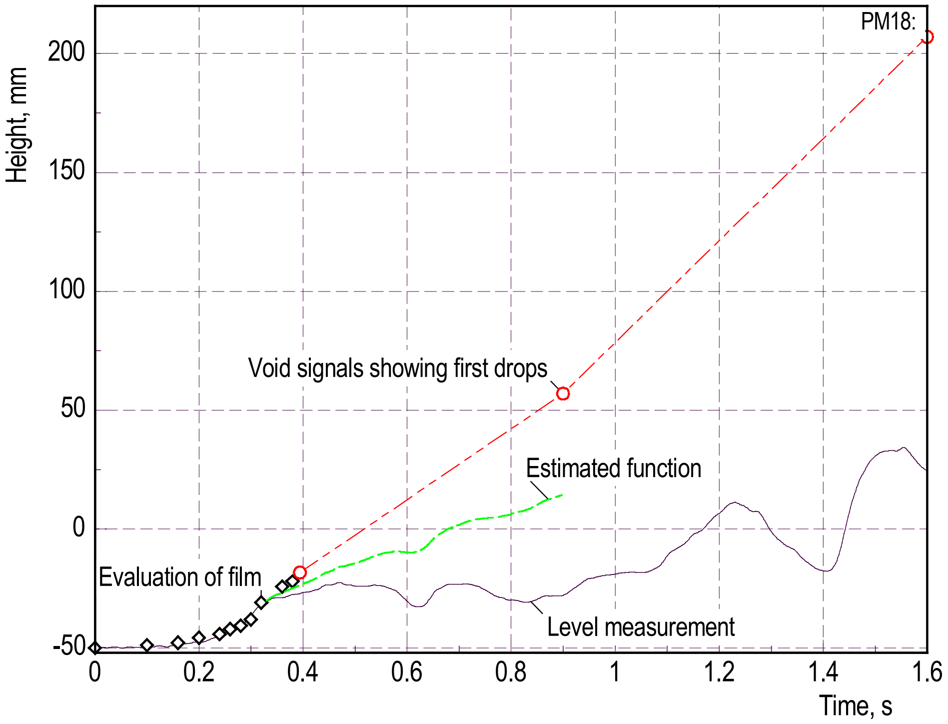

LM18 | 21.3.2000

Fig. D12: Estimated time function taken as an upper limit of the interaction zone in the calculation. It was formed as a mean function of (1) an upper boundary line given by the appearence of first liquid drops and (2) the level measurement. Taking the level measurement as an upper limit would exclude a substantial portion of the churned liquid from the mass balance. (See also the note made in the instrumentation chapter).

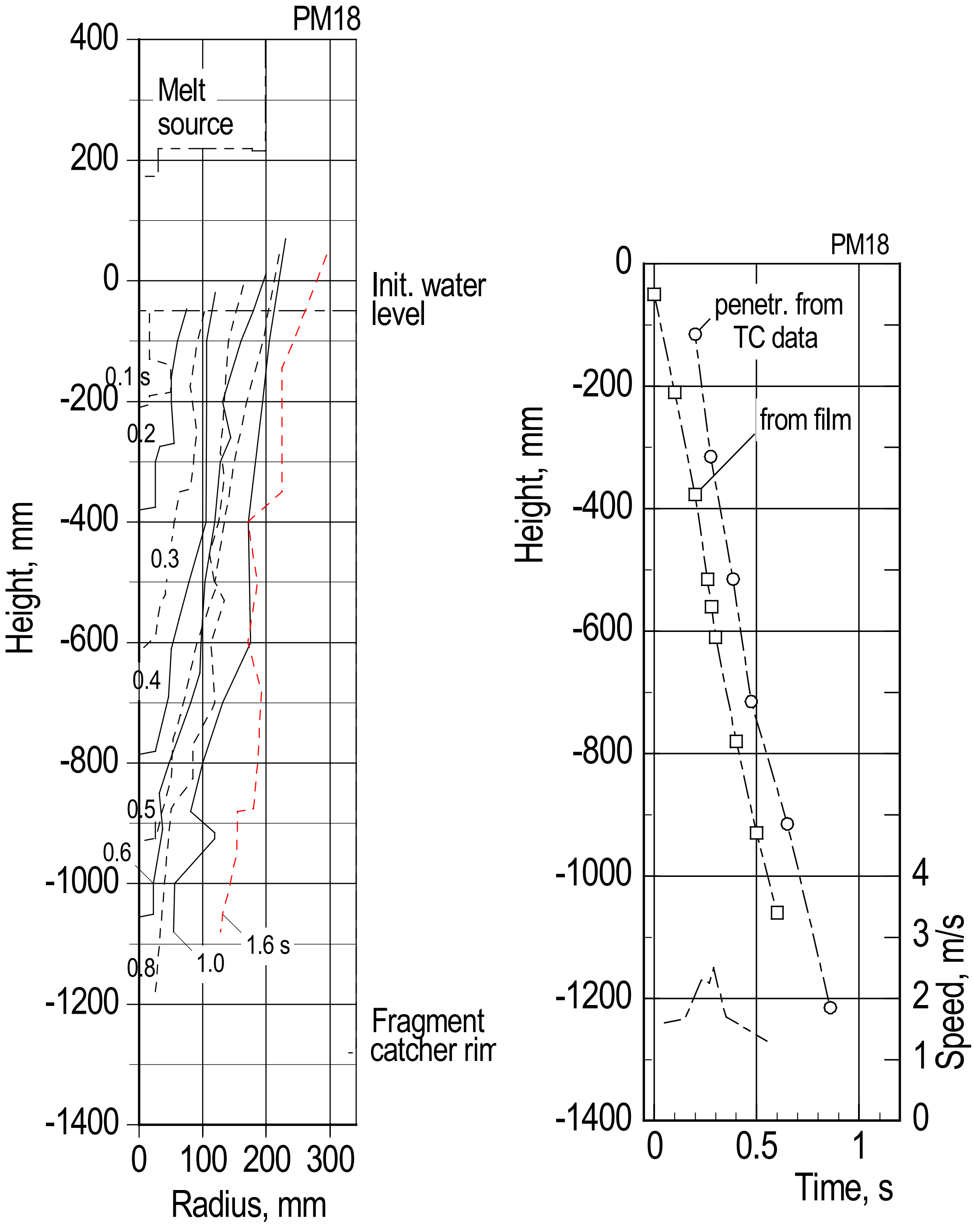

Fig. D13: Progression of the interaction zone in the axial and radial directions shown with the time as a parameter (left hand side). The evaluation was made mainly on basis of film pictures. The films covered the height down to –1080 mm. Axial penetration of the melt obtained from thermocouples (t/c) and from film pictures (right hand side). The speed of the leading edge was derived from the film data.

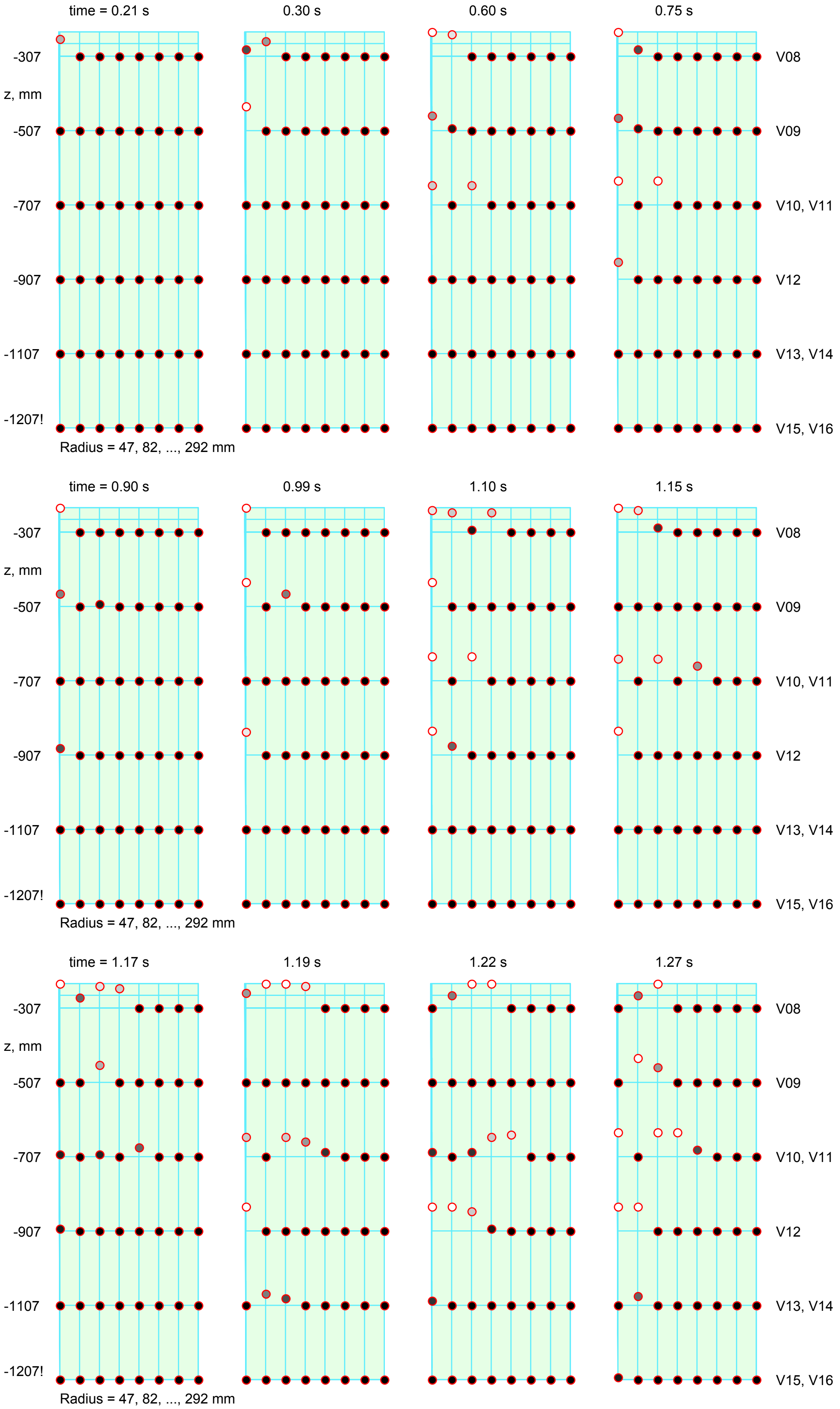

Fig. D14: PM18. Local distribution of steam and water obtained from void probes at selected times. Dark points on base line=water; bright elevated points=steam.

Fig. D14. PM18. Local distribution of steam and water (continued).

APPENDIX E: Melt Release. Performance and Numerical Simulation

1. Performance

To reproduce the melt release mode applied in FARO tests, which occurred under gravity conditions, a special procedure was performed in the PM16, PM17, and PM18 PREMIX tests. The main features of this procedure were as follows.

A operational control system (short: OCS) ought to maintain the pressure difference between melt generator and interaction zone at a level of around 0.005 MPa. To this end, the pressure in the melt generator was adjusted by back-feeding of gas from a reservoir. Depending on the rate of change of the pressure in the interaction zone, up to two valves mounted in parallel feeding lines were opened.

2. Calculation of the melt release rate using pressure measurements

The one-dimensional numerical model is based on the following momentum equation that describes the flow of melt in a pipe:

$$dv=dt/h*\ (g*h - 0.5*(v+0.5*dv)^2*zk + p_d(t)/rho), \qquad \text{(E1)}$$

or, in the difference form,

$$\Delta v=\Delta t/h*(g*h - 0.5*(v+0.5*\Delta v)^2*zk + p_d(t)/rho), \qquad \text{(E2)}$$

where

v and Δv	are the velocity and the change in velocity, respectively,
t and Δt	are the time variable and the time step (=0.001 s), respectively,
g and h	are the gravity constant and the actual geodetic height of the melt,
p_d	is the time history of the pressure difference acting on the melt,
rho	is the density, and
zk	is a composed number accounting for acceleration and for friction losses:

$$zk = 1+\varsigma+\lambda*l_{noz}/d_{noz}.$$

In the discretization (Fig. E1), the lower end of the nozzle tube is taken as the origin of the axial coordinate. The difference of the pressures measured inside and outside of the melt generator, GP12 and PKir15, are taken as input. The initial height of the melt in the crucible is calculated from the total mass of fragments found after the test, m0. The density (2800 kg/m^3) was set to 80% of the theoretical density attributed to the actual composition of the fragments (= alumina plus smaller fractions of iron) found after the test. The most significant output data are the melt mass flow rate and the duration of melt release.

In the calculation, constant loss coefficients, constant flow cross section, constant viscosity and temperature, and homogeneous flow of melt are assumed. The loss coefficients were chosen to be ς=0.6 at the entrance to nozzle tube and λ=0.22 within the tube. As for the flow cross section, a small average crust thickness of 1.5 millimeters is considered that reduces the nozzle internal diameter. The loss coefficients were chosen to be ς=0.6 at the entrance to nozzle tube and λ=0.22 within the tube.

The loss coefficients (which are in fact somewhat larger than those generally used for single-phase flow in a smooth pipe) together with the density and the reduced nozzle diameter resulted in melt release times that agree with those derived from the pressure readings. It should be noted that corresponding sets of parameters gave good results also for other PREMIX melt generator designs.

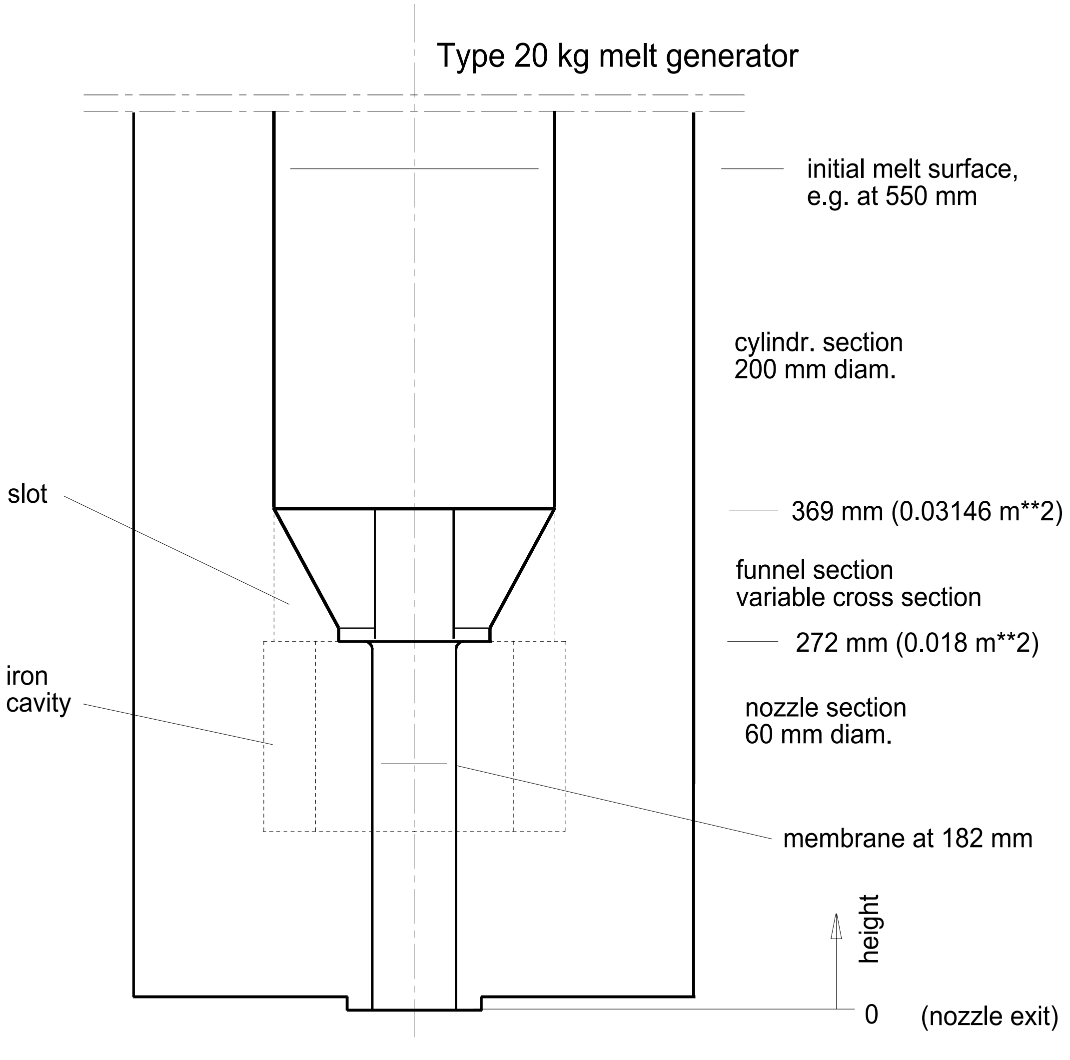

Fig. E1: Schematic of the melt generator used in the PM12 – PM15 and PM17 – PM18 PREMIX tests.

The calculation is started at the time when the steel membrane in the nozzle melts. The initial height of the melt in the crucible is calculated from the total mass of fragments found after the test. The flow of melt starts from the state of rest.

The fraction of melt mass that passes the initial location of the membrane during Δt is given by

$$\Delta me(t_i) = 0.5 * (v_{i-1} + v_i) * \Delta t * rho * A_{noz}, \qquad \text{(E3)}$$

where A_{noz} is the nozzle cross section. The mass fractions are integrated to give the total mass:

$$me(t_i) = me(t_{i-1}) + \Delta me(t_i). \qquad \text{(E4)}$$

The melt surface is considered to move evenly at any time. The funnel cross section is given as a function of the axial coordinate. The calculation is stopped when the mass ejected is equal to the initial melt mass, m0.

APPENDIX F: Estimation of the volumes and masses involved in the thermal interaction

The volume of the interaction zone can be regarded as composed of three partial volumes:

$$V_I = V_{\ell,I} + V_{v,I} + V_{m,I} \,. \qquad \text{(F1)}$$

The partial volumes refer, in the above sequence, to liquid, vapour (i.e. more common expression for steam), and melt. The volume of the interaction zone, V_I, can be obtained from the measurements. The $V_{v,I}$ and $V_{m,I}$ partial volumes can be estimated from the measurements and thereby the $V_{\ell,I}$ partial volume of the liquid. This is described in the following.

The *partial volume of the vapour,* $V_{v,I}$, is calculated from a mass balance considering the masses involved in the interaction. The control room of the balance comprises the pool water volume, the melt provided by the melt generator, and the steam within the gas space. This space covers the whole gaseous compartment above the initial water surface up to the location of the flow meters. The sum of the masses prior to the test is:

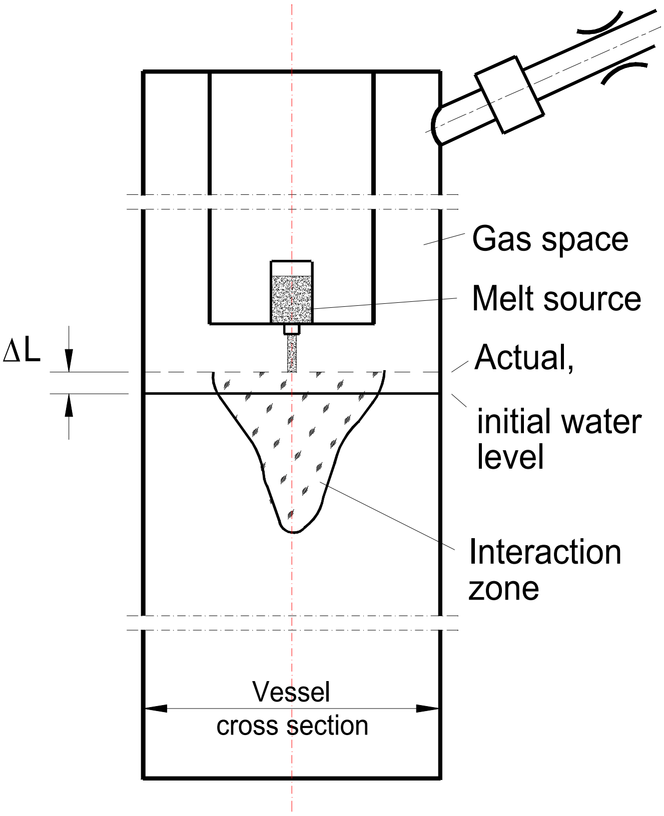

Fig. F1: Conditions around the interaction zone, schematically.

$$\sum m = m_{\ell}^{0} + m_{v,G}^{0} + m_m \,, \qquad \text{(F2)}$$

where the superscript 0 means the condition for t=0. Application of the relation $m = V \cdot \rho$ to eq. (B1) results in

$$\sum m = V_{\ell}^{0} \cdot \rho_{\ell} + V_{v,G}^{0} \cdot \rho_v + V_m \cdot \rho_m \,. \qquad \text{(F2a)}$$

For times t > 0, part of the water evaporates. Both the masses of the liquid and the steam become functions of time and the mass balance provides the relation:

$$\sum m = m_\ell + m_{\ell,I} + m_{v,I} + m_{v,G} + m_{v,exit} + m_m \tag{F3}$$

The meaning of the summands is:

- m_ℓ is the mass of the water outside of the interaction zone;
- $m_{\ell,I}$ and $m_{v,I}$ are the masses of the water and the steam, respectively, inside the interaction zone;
- $m_{v,G}$ is the mass of steam in the gas space. It diminishes with time due to the growth of the interaction zone;
- $m_{v,exit}$ is the integrated steam mass whose volume flow rate is measured at the venting tubes.

The volume of m_ℓ in eq. (F3) is calculated as initial water volume plus water level increase times vessel cross section minus interaction volume (compare Fig. F1):

$$V_{\ell,pool} = V_\ell^0 + \Delta L \cdot A_V - V_I . \tag{F4}$$

Introducing densities in eq. (F3) and considering eq. (F4) one obtains:

$$\sum m = (V_\ell^0 + \Delta L \cdot A_V - V_I) \cdot \rho_\ell + V_{\ell,I} \cdot \rho_\ell + V_{v,I} \cdot \rho_v + V_{v,G} \cdot \overline{\rho}_v + V_{v,exit} \cdot \rho_v + V_m \cdot \rho_m \tag{F3a}$$

Eqs. (F2a) and (F3a) are equated while also considering eq. (F1) and taking into account that $\rho_v / \rho_\ell << 1$. One obtains, after a few conversions, an equation for the partial volume of the vapour:

$$V_{v,I} = \Delta L \cdot A_V - V_{m,I} + V_{v,exit} \cdot \frac{\rho_v}{\rho_\ell} + \left[V_{v,G} \cdot \frac{\overline{\rho}_v}{\rho_\ell} - V_{v,G}^0 \cdot \frac{\rho_v}{\rho_\ell} \right] \tag{F5}$$

The two terms summarised in brackets constitute the change in steam volume in the gas room. The difference is very small and, therefore, eq. (F5) is reduced to the following equation:

$$V_{v,I} = \Delta L \cdot A_V - V_{m,I} + V_{v,exit} \cdot \rho_v / \rho_\ell , \tag{F5a}$$

The (total) melt volume, V_m, disappears during the above conversions. Instead, the *partial volume of the melt*, $V_{m,I}$, comes into consideration in eq. (F5a). Since the melt flow rate can not be measured in the experiments, the melt volume flow entering the interaction zone is estimated on basis of the flow rate predicted by a simple numerical model (see Appendix E). The calculated mass flow function has to be shifted in time to account for the travelling time of the melt front through the initial falling height. The function is drawn in Fig. F2 taking PM13 as an example.

Using the melt flow function, the $V_{v,I}$ partial volume of the vapour could now be calculated from eq. (F5a) and thereby also the $V_{\ell,I}$ partial volume of the liquid water from eq. (F1). The three essential functions that determine the calculation are shown in Fig. F3 on a larger time scale.

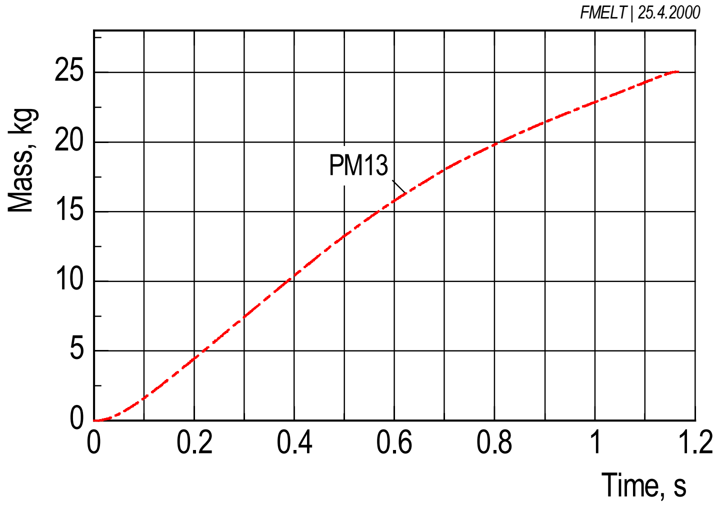

Fig. F2: Integrated mass entering the interaction zone.

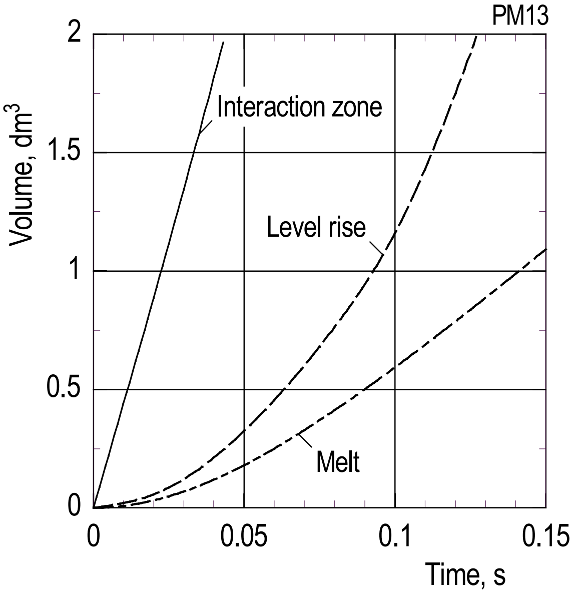

Fig. F3: The three functions that determine the calculation of the volume fractions shown in a larger time scale.